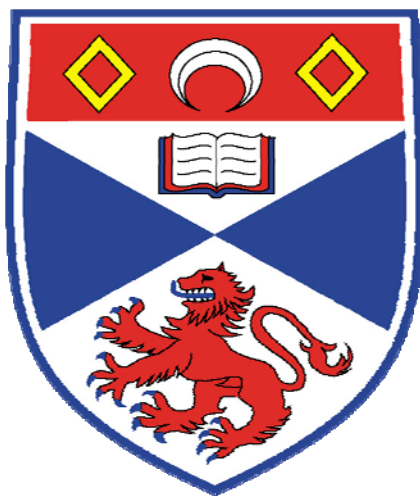


MICRORESONATORS FOR ORGANIC SEMICONDUCTOR AND FLUIDIC LASERS

Andreas E. Vasdekis



2007

A thesis submitted to the School of Physics and Astronomy, at the
University of St Andrews, for the degree of Doctor of Philosophy.

Abstract

This thesis describes a number of studies of microstructured optical resonators, designed with the aim of enhancing the performance of organic semiconductor lasers and exploring potential applications. The methodology involves the micro-engineering of the photonic environment in order to modify the pathways of the emitted light and control the feedback mechanism. The research focuses on designing new organic microstructures using established semi-analytical and numerical methods, developing fabrication techniques using electron-beam lithography, and optically characterising the resulting structures.

Control of the feedback mechanism in conjugated polymer lasers is first investigated by studying Distributed Feedback or photonic crystal resonators based on a square feedback lattice. This study identified the diffraction to free space radiation as a major source of loss in current microstructured resonator designs. By cancelling the coupling to free space through the use of different feedback symmetries and diffraction orders, a threshold reduction by almost an order of magnitude is demonstrated.

The introduction of mid-gap defect photonic states in an otherwise uniformly periodic structure was studied in Distributed Bragg Reflector (DBR) resonators. This enabled GaN diode pumped polymer lasers to be demonstrated, indicating that the transition from complex excitation sources to more compact systems is possible. Devices for potential applications in the field of optical communications are also explored by demonstrating a polymer DBR laser based on silicon. In this way, the potential for integrating conjugated polymers with silicon photonics is confirmed.

Photonic crystal fibres, which have a periodic microstructure in the transverse direction, are explored as an alternative means for controlling the optical properties of organic lasers. Fluidic fibre organic lasers were demonstrated as efficient sources with good spectral purity. In these devices, mechanisms to tune the emission wavelength were explored and the origin of the frequency selection mechanism was investigated.

Declarations

I, Andreas E. Vasdekis, hereby certify that this thesis, which is approximately 40,000 words in length, has been written by me, that it is the record of the work carried out by me and that it has not been submitted in any previous application for a higher degree.

Andreas E. Vasdekis

July 2007

I was admitted as a research student in October 2004 and as a candidate for the degree of Doctor in Philosophy in October 2004; the higher study for which this is a record was carried out in the University of St. Andrews between 2004 and 2007.

Andreas E. Vasdekis

July 2007

I hereby certify that the candidate has fulfilled the conditions of the Resolution and Regulations appropriate for the degree of Doctor in Philosophy in the University of St. Andrews and that the candidate is qualified to submit this thesis in application for that degree.

Graham A. Turnbull

July 2007

Copyright Declaration

In submitting this thesis to the University of St. Andrews I understand that I am giving permission for it to be made available for use in accordance with the regulations of the University Library for the time being in force, subject to any copyright vested in the work not being affected thereby. I also understand that the title and abstract will be published, and that a copy of the work may be made and supplied to any *bona fide* library or research worker, that my thesis will be electronically accessible for personal, or research use, and that the library has the right to migrate my thesis into new electronic forms as required to ensure continued access to the thesis. I have obtained any third-party copyright permissions that may be required in order to allow such access and migration.

Andreas E. Vasdekis

July 2007

Acknowledgments

I would like to thank Dr. Graham Turnbull and Prof. Ifor Samuel for their helpful comments and the fruitful discussions the past years and more importantly for providing a stimulating research environment. I am also grateful to Prof. T.F. Krauss for supportive and motivating discussions. Many thanks to the members of the Organic Semiconductor Centre and especially to Dr. A. Ruseckas, Dr. M. Goossens, Dr. O. Gaudin, Dr. C. Yates, Dr. P. André, Dr. A. McNeil, Dr. E. Nambdas, Mr. S. Stevenson, Mrs. D. Amarasinghe, Dr. J. Crayston and Dr. M. Buck. The contribution of Dr. J.-C. Ribierre and Mr. G. Tsiminis to the diode pumping experiments and the assistance by Dr. O' Faolain, Mr. S. Moore and Dr. M. Kotlyar on the microfabrication are gratefully acknowledged.

I am indebted to Prof. G. Town in Macquarie University for his assistance on the fluidic fibre laser experiments and to Prof. W. Barnes in the University of Exeter for providing the initial grating structures used in this thesis. I would also like to thank the technical and secretarial staff in St. Andrews and especially Mr. G. Robb and Mr. S. Balfour.

Financial support from the EPSRC through my PhD studentship and the fellowship award from the Wingate Foundation for the silicon based lasers work are also gratefully acknowledged.

I dedicate this work to my parents, Irini and Efthimio Vasdeki.

‘... we shall want finally to describe that research as a strenuous and devoted attempt to force nature into conceptual boxes...’

Thomas S. Kuhn
The Structure of Scientific Revolutions, 3rd edition (1996).

Table of contents

CHAPTER 1: Introduction	9
CHAPTER 2: The theory of organic semiconductor lasers	19
2.1 Introduction	19
2.2 Electronic structure of conjugated molecules	20
2.3 Optical properties of conjugated molecules	23
2.3.1 Absorption of light	23
2.3.2 Emission of light	24
2.3.3 Amplification of light	27
2.4 Resonators for organic lasers	30
2.4.1 Fabry Perot resonator	31
2.4.2 Distributed Feedback resonator	33
2.4.3 Distributed Bragg reflector resonator	37
2.5 References	39
CHAPTER 3: Methodology	44
3.1 Introduction	44
3.2 Micro-resonator fabrication	45
3.2.1 Electron beam lithography	46
3.2.2 Pattern transfer	48
3.2.3 Nanostructured silica fabrication for polymer lasers	49
(a) Charge dissipation	50
(b) Adhesion	52
(c) Proximity correction	55
3.3 Ellipsometry	57
3.3.1 Introduction	57
3.3.2 Ellipsometric investigations	60
3.4 Optical design and characterisation	62
3.4.1 Design	62

3.4.2 Optical characterisation	67
3.5 Summary	70
3.6 References	71
 CHAPTER 4: Distributed feedback polymer lasers and radiation losses	 74
4.1 Introduction	74
4.2 Radiation losses	76
4.2.1 Diffractive processes in periodic structures	76
4.2.2 Radiation losses and laser operation	78
4.3 Low threshold edge emitting polymer DFB laser based on a square lattice	80
4.3.1 The resonant symmetries of a square lattice	80
4.3.2 Low threshold operation	83
4.3.3 Dual mode operation	86
4.3.4 Beam quality	89
4.3.5 The Q-factor of the resonator	91
4.3.6 Summary	93
4.4 Low threshold surface emitting polymer DFB laser: integration	94
4.4.2 Integration of an output coupler: low threshold and surface emission	95
4.4.3 Alternative position of the coupler	99
4.5 Conclusions	102
4.6 References	104
 CHAPTER 5: Distributed Bragg Reflector polymer lasers and applications	 106
5.1 Introduction	106
5.2 Microcavity lasers	107
5.3 Microstructured DBR polymer lasers	110
5.3.1 Introduction	110
5.3.2 Characterisation below threshold	112
5.3.3 Characterisation above threshold	116
5.4 Diode pumped polymer lasers	119
5.4.1 Introduction	119

5.4.2 Gain medium	120
5.4.3 Lasing studies	121
5.4.4 Summary	124
5.5 A silicon based polymer laser	125
5.5.1 Introduction	125
5.5.2 Characterisation	127
5.5.3 Comparison with SiO ₂ mirrors	131
5.5.4 Summary	133
5.6 Summary	134
5.7 References	135
 CHAPTER 6: Fluidic dye lasers based on photonic crystal fibres	 137
6.1 Introduction	137
6.2 The methodology of photonic crystal fibre based fluidic lasers	138
6.3 Laser performance	143
6.3.1 Optical characterisation	143
6.3.2 Coupling efficiency and waveguide length	146
6.3.3 Tuneability	150
6.4 Wavelength selectivity	151
6.4.1 Antiresonant waveguiding	152
6.4.2 Length dependence and the Vernier effect	155
6.5 Summary	161
6.6 References	162
 CHAPTER 7: Conclusions	 166
 Appendix A: Procedure for electron beam fabrication	 171
 Appendix B: Publications arising from this work	 172

CHAPTER 1:

Introduction

Light-emitting organic semiconductors have been the subject of substantial theoretical and applied research over the past two decades. The discovery of efficient electroluminescence in small molecules [1] and conjugated polymers [2] triggered an explosion of interest in this field of condensed matter due to the plethora of potential applications, such as displays [3], solar cells [4], organic transistors [5] and lasers [6]. A reason why organic semiconductors have attracted significant attention is their relative ease of processing, in contrast to the epitaxial growth of inorganic semiconductors. Solution processible polymers and small molecules provide access to the coverage of large and even flexible surfaces, but also to novel preparation techniques such as ink-jet printing. Organic semiconductors are intrinsically low dimensional electronic systems and photonic structures are readily accessible with cost-effective techniques such as soft lithography [7, 8]. These properties enable the control of the interaction of photons with electrons [9, 10] with enormous potential in the field of solid-state lighting and visible laser sources.

Organic media are excellent candidates for lasing applications due to their high and broadband gain and great research interest remains active due to the prospects of low cost visible sources of coherent radiation, with applications ranging from telecommunications to femtosecond spectroscopy and coherent lighting. Currently, the pumping scheme of organic semiconductor lasers is based on optical excitation, hindering thus the possible applications to a certain extent. At the time this thesis commenced, the most compact excitation source was the frequency doubled microchip laser [11]. Further simplifying their excitation configuration could further enhance their practicality. To this end, the physics behind their operation is at the centre of

vigorous research in order to reduce the threshold, optimise their operation characteristics, increase their lifetime and ultimately demonstrate electrical injection lasing.

The versatility of organic semiconductors is yet again justified as they can be employed both in the liquid and undiluted solid state for laser applications. Solid-state organic semiconductor lasers were first demonstrated in 1996 [6, 12-15] and since then it has been a field of enthusiastic activity. Some of the most recent major findings involve the demonstration of diode pumped [16-18] and quasi-continuous wave polymer lasers [19], chemical sensing applications [20], short pulse generation [21] and the incorporation of metal contacts maintaining low threshold lasing [22]. Novel material combinations are introduced, aiming both at enhanced emission efficiencies and thus lower oscillation thresholds [23-26], but also improved charge mobility for more efficient electroluminescence and possibly electrical injection [27].

Different resonators for solid-state polymer laser applications have been also subject to extensive investigation. Several types of resonators have been demonstrated, such as microcavity [28], microdisc and microring lasers [29]. However, distributed feedback (DFB) cavities based on periodic microstructures show some of the lowest lasing thresholds [30] and due to their OLED type film architecture, are of most interest in the continuing quest for electrical excitation. When compared to one-dimensional DFB lasers, two-dimensional feedback structures exhibit lower oscillation thresholds [31] and better quality output beams [11, 32] due to the increased in-plane confinement and gain length. Different types of distributed feedback lattices have been also investigated, involving square [11, 33, 34], hexagonal [35-37] and circular DFB lasers [38-40]. Experiments to control the refractive index contrast within a unit cell have been performed, by employing Au and TiO₂ instead of silica and leading to even more microscopic resonators [41-43]. These experiments not only contributed to the optimisation of polymer lasers, but also lead to a deeper insight in the physics of periodic structures. The ease of processing has lead several research groups to focus on

these materials and explore new laser physics, such as the photonic crystal resonator based on the Penrose lattice [44].

In regards to liquid-state organic lasers, they have been the at the focus of attention for almost half a century and both small molecules [45], and more recently conjugated polymers [46], have been employed in numerous applications. In recent years, renewed interest has been focused on this field due to the emergence of optofluidics. Optofluidic devices have been developed as a tool for sensing, imaging and spectroscopy applications as they uniquely combine the non-intrusive interaction capabilities of photons and the fluidic delivery of biological samples [47]. Several types of devices have been demonstrated including adaptive lenses, optical manipulators of particles and sensors [48-50]. Fluidic lasers can act as efficient sources of narrow linewidth emission and their integration within fluidic networks can be easily implemented achieving significant progress towards lab-on-a-chip applications [51-55]. Organic gain media are currently one of the few available candidates in this field of visible laser sources.

This thesis aims to explore both solid- and liquid-state organic lasers and their applications. The organic chromophores that were used throughout were commercially available and so the focus of this work is only on the properties of the resonators. Firstly, the physics of periodic structures is employed to illuminate the properties and identify the major sources of loss of polymer DFB lasers, enabling an optimisation analysis and the demonstration of a threshold reduction by almost an order of magnitude. The effect of defects in uniform periodic structures is well established in the fields of solid-state physics and photonics and it is the second focus area. The transition from extended to localised photonic states and its consequences on the operation of polymer lasers is investigated and novel applications are demonstrated. Thirdly, long interaction lengths are investigated for fluidic laser applications employing microstructured fibre structures. An unanticipated frequency selection mechanism is demonstrated present in a very simple optical system where the need for reflectors and microstructures is not necessary.

The basic theory of organic semiconductor lasers is discussed in Chapter 2, both in the context of the relevant material properties and the operation of the most common laser structures. The relevant methodology for their experimental and theoretical study is outlined in Chapter 3. The time demanding electron beam lithography was chosen for its design versatility, and ellipsometric investigations took place to determine the optical constants and the exact thickness values of the films involved in the laser structures. These values were of utmost importance in terms of predicting the behaviour of polymer thin film lasers.

Distributed feedback organic semiconductor lasers are treated in Chapter 4. They exhibit the same operational characteristics as band-edge photonic crystal lasers [56, 57] and were likewise studied to identify their optimal operation conditions. The periodic refractive index perturbation is the origin of the feedback mechanism, but can also cause additional diffractive processes, such the advantageous surface emission. It was found that the performance of polymer lasers is greatly enhanced by directing the output beam from the surface to the edge. In this way, the radiation losses are reduced and a threshold reduction by almost an order of magnitude was demonstrated. Some of the first integration steps in the field of polymer optoelectronics were performed to re-direct the emission from the edge to the surface, hence addressing the divergence of edge-emitted beams from thin films and demonstrating a low threshold, surface-emitting polymer laser.

The absence of a few unit cells in a periodic lattice induces a significant change in the behaviour of polymer thin film lasers. The resulting laser modes are localised within the defect, replacing the Bloch modes of the distributed feedback lasers. These are the defect or DBR lasers and are treated in Chapter 5. Their operation is analysed in comparison to microcavity polymer lasers and their differences provide a deeper insight to the laser physics involved, but also indicates the relevant operational advantages. The optimised performance and repeatability of DBR lasers lead to a major finding of my thesis, namely the demonstration of diode pumped polymer lasers. This finding is of significant importance in the field of solid-state polymer lasers,

which along with similar attempts from other research groups denoted the transition from a paradigm of complex excitation sources (e.g. dye lasers, microchip lasers) to a new one where miniature inorganic diode lasers can be used.

Silicon based photonic integration has received significant attention in recent years due to its potential for cost-effective components for optical communications and interconnects [58]. A major hindrance towards this aim is the poor optical emission efficiency of silicon. To overcome this, several approaches have been proposed, including optically excited Raman lasers [59] and nanopatterned Si waveguides [60], while promising steps have been also achieved in the field of nanocrystals [61, 62], Er doped silicon [63] and III-V semiconductor lasers bonded to silicon chips [64]. An alternative approach is proposed in my thesis (Chapter 5), realised by combining microstructured silicon resonators with light-emitting polymers. This novel approach is based on the cost-effective CMOS fabrication processes and the integration of solution processible emitters adds only a simple supplementary fabrication step. To this end, a novel DBR resonator design based on silicon-on-insulator was examined and a polymer laser based on silicon was demonstrated. The laser was configured as surface emitting, hence compatible with the prospect of future lateral integration with silicon photodetectors.

Fluidic photonic crystal fibres have been explored as fluidic refractive index sensors and filters, both in the visible and the telecommunication wavelength range [65-67]. In Chapter 6, a photonic crystal fibre fluidic laser is demonstrated, hence expanding the functionality of this type of microstructures within the field of optofluidics. The experimental methods are outlined and the laser performance is analysed both in the context of its threshold and quantum efficiency, but also approaches to tune the emission wavelength are explored. An additional motivation of this work was to investigate the possibility of realising a laser based on a periodic structure, where the periodicity is transverse to the propagation direction. This is in contrast to DFB lasers, where the grating vector is parallel to the propagation of the laser field. However it was found that resonant effects do not play a role in the stimulated emission process.

Although the transverse periodicity was irrelevant, an interesting frequency selection mechanism was observed, leading to a free spectral range that does not correspond to the length of the liquid cores. This mechanism is attributed to a Vernier type effect between transverse modes. This type of laser features a hexagonal array of approximately 50 liquid waveguides and demonstrates the feasibility of lateral integration. In addition, the output power from this device is adequate for the formation of triangular optical lattices with applications in the field of optical-tweezing.

References

1. C.W. Tang, S.A. Vanslyke, 'Organic electroluminescent diodes', *Applied Physics Letters* **51**, 913 (1987).
2. J.H. Burroughes, D.D.C. Bradley, A.R. Brown, R.N. Marks, K. Mackay, R.H. Friend, P.L. Burn, A.B. Holmes, 'Light-emitting diodes based on conjugated polymers', *Nature* **347**, 539 (1990).
3. R.H. Friend, R.W. Gymer, A.B. Holmes, J.H. Burroughes, R.N. Marks, C. Taliani, D. D. C. Bradley, D.A.D. Santos, J. L. Bredas, M. Logdlund, W.R. Salaneck, 'Electroluminescence in conjugated polymers', *Nature* **397**, 121 (1999).
4. G. Yu, J. Gab, J.C. Hummelen, F. Wudl, A.J. Heeger, 'Polymer photovoltaic cells - enhanced efficiencies via a network of internal donor-acceptor heterojunction', *Science* **270**, 1789 (1995).
5. A. Tsumura, H. Koezuka, T. Ando, 'Macromolecular electronic device: Field-effect transistor with a polythiophene thin film', *Applied Physics Letters* **49**, 1210 (1986).
6. N. Tessler, G.J. Denton, R.H. Friend, 'Lasing from conjugated polymer microcavities', *Nature* **382**, 695 (1996).
7. Y. Xia, G.M. Whitesides, 'Soft lithography', *Angew. Chem. Int. Ed.* **37**, 550 (1998).
8. S.R. Quake, A. Scherer, 'From micro- to nanofabrication with soft materials', *Science* **290**, 1536 (2000).
9. E. Yablonovitch, 'Inhibited spontaneous emission in solid-state physics and electronics', *Physical Review Letters* **58**, 2059 (1987).

10. C. Weisbuch, H. Benisty, R. Houdre, 'Overview of fundamentals and applications of electrons, excitons and photons in confined structures', *Journal of Luminescence* **85**, 271 (2000).
11. G.A. Turnbull, P. Andrew, W.L. Barnes, I.D.W. Samuel, 'Operating characteristics of a semiconducting polymer laser pumped by a microchip laser', *Applied Physics Letters* **82**, 313 (2003).
12. W. Holzer, A. Penzkofer, S.-H. Gong, A. Bleyer, D.D.C. Bradley, 'Laser Action in Poly(m-phenylenevinylene-co-2,5-dioctoxy-p-phenylenevinylene)', *Advanced Materials* **8**, 974 (1996).
13. N. Tessler, 'Lasers based on semiconducting organic materials', *Advanced Materials* **11**, 363 (1999).
14. V.G. Kozlov, S.R. Forrest, 'Lasing action in organic semiconductor thin films', *Current Opinion in Solid State & Materials Science* **4**, 203 (1999).
15. M.D. McGehee, A.J. Heeger, 'Semiconducting (conjugated) polymers as materials for solid-state lasers', *Advanced Materials* **12**, 1655 (2000).
16. T. Riedl, T. Rabe, H.-H. Johannes, W. Kowalsky, J. Wang, T. Weimann, P. Hinze, B. Nehls, T. Farrell, U. Scherf, 'Tunable organic thin-film laser pumped by an inorganic violet diode laser', *Applied Physics Letters* **88**, 241116 (2006).
17. C. Karnutsch, C. Grtner, V. Haug, U. Lemmer, T. Farrell, B. Nehls, U. Scherf, J. Wang, T. Weimann, G. Heliotis, C. Pflumm, J. Demello, D.D.C. Bradley, 'Low threshold blue conjugated polymer DFB lasers', *Conference on Lasers and Electro-optics, CLEO*, paper CFJ3 (2006).
18. A.E. Vasdekis, G. Tsiminis, J.-C. Ribierre, L.O. Faolain, T.F. Krauss, G.A. Turnbull, I.D.W. Samuel, 'Diode pumped distributed Bragg reflector lasers based on a dye-to-polymer energy transfer blend', *Optics Express* **14**, 9211 (2006).
19. T. Rabe, K. Gerlach, T. Riedl, H.-H. Johannes, W. Kowalsky, J. Niederhofer, W. Gries, J. Wang, T. Weimann, P. Hinze, F. Galbrecht, U. Scherf, 'Quasi-continuous-wave operation of an organic thin-film distributed feedback laser', *Applied Physics Letters* **89**, 081115 (2006).
20. A. Rose, Z. Zhu, C.F. Madigan, T.M. Swager, V. Bulovic, 'Sensitivity gain in chemosensing by lasing action in organic polymers', *Nature* **434**, 876 (2005).
21. M. Goossens, A. Ruseckas, G.A. Turnbull, I.D.W. Samuels, 'Subpicosecond pulses from a gain-switched polymer distributed feedback laser', *Applied Physics Letters* **85**, 31 (2004).
22. M. Reufer, S. Riechel, J.M. Lupton, J. Feldmann, U. Lemmer, D. Schneider, T. Benstem, T. Dobbartin, W. Kowalsky, A. Gombert, K. Forberich, V. Wittwer, U. Scherf, 'Low-threshold polymeric distributed feedback lasers with metallic contacts', *Applied Physics Letters* **84**, 3262 (2004).
23. R. Xia, G. Heliotis, D.D.C. Bradley, 'Fluorene-based polymer gain media for solid-state laser emission across the full visible spectrum', *Applied Physics Letters* **82**, 3599 (2003).
24. T. Aimonio, Y. Kawamura, K. Goushi, H. Yamamoto, H. Sasabe, C. Adachi, '100% fluorescence efficiency of 4,4'-bis(N-carbazole)styryl-biphenyl in a solid film and the very low amplified spontaneous emission threshold', *Applied Physics Letters* **86**, 071110 (2005).
25. T. Rabe, M. Hoping, D. Schneider, E. Becker, H.-H. Johannes, W. Kowalsky, T. Weimann, J. Wang, P. Hinze, B.S. Nehls, U. Scherf, T. Farrell, T. Riedl, 'Threshold reduction in polymer

- lasers based on poly(9,9-dioctylfluorene) with statistical binaphthyl units', *Advanced Functional Materials* **15**, 1188 (2005).
26. F. Marchioni, R. Chiechi, S. Patil, F. Wudl, 'Absolute photoluminescence quantum yield enhancement of poly(2-methoxy 5-[2'-ethylhexyloxy]-p-phenylenevinylene)', *Applied Physics Letters* **89**, 061101 (2006).
 27. G. Heliotis, S.A. Choulis, G. Itskos, R. Xia, R. Murray, P.N. Stavrinou, D.D.C. Bradley, 'Low-threshold lasers based on a high-mobility semiconducting polymer', *Applied Physics Letters* **88**, 081104 (2006).
 28. L. Persano, P.D. Carro, E. Mele, R. Cingolani, D. Pisignano, M. Zavelani-Rossi, S. Longhi, G. Lanzani, 'Monolithic polymer microcavity lasers with on-top evaporated dielectric mirrors', *Applied Physics Letters* **88**, 121110 (2006).
 29. M. Kuwata-Gonokami, R.H. Jordan, A. Dodabalapur, H.E. Katz, M.L. Schilling, R.E. Shusher, 'Polymer microdisk and microring lasers', *Optics Letters* **20**, 2093 (1995).
 30. C. Karnutsch, C. Gyrtner, V. Haug, U. Lemmer, T. Farrell, B.S. Nehls, U. Scherf, J. Wang, T. Weimann, G. Heliotis, C. Pflumm, J.C. Demello, D.D.C. Bradley, 'Low threshold blue conjugated polymer lasers with first- and second-order distributed feedback', *Applied Physics Letters* **89**, 201108 (2006).
 31. G. Heliotis, R. Xia, G.A. Turnbull, P. Andrew, W.L. Barnes, I.D.W. Samuel, D.D.C. Bradley, 'Emission characteristics and performance comparison of polyfluorene Lasers with One- and Two Dimensional Distributed Feedback', *Advanced Functional Materials* **14**, 9 (2004).
 32. A. Mekis, A. Dodabalapur, R.E. Slusher, J.D. Joannopoulos, 'Two-dimensional photonic crystal couplers for unidirectional light output', *Optics Letters* **25**, 942 (2000).
 33. S. Riechel, C. Kallinger, U. Lemmer, J. Feldmann, A. Gombert, V. Wittwer, U. Scherf, 'A nearly diffraction limited surface emitting conjugated polymer laser utilizing a two-dimensional photonic band structure', *Applied Physics Letters* **77**, 2310 (2000).
 34. A.E. Vasdekis, G.A. Turnbull, I.D.W. Samuel, P. Andrew, W.L. Barnes, 'Low threshold edge emitting polymer distributed feedback laser based on a square lattice', *Applied Physics Letters* **86**, 161102 (2005).
 35. M. Notomi, H. Suzuki, T. Tamamura, 'Directional lasing oscillation of two-dimensional organic photonic crystal lasers at several photonic band gaps', *Applied Physics Letters* **78**, 1325 (2001).
 36. M. Kitamura, S. Iwamoto, Y. Arakawa, 'Enhanced light emission from an organic photonic crystal with a nanocavity', *Applied Physics Letters* **87**, 151119 (2005).
 37. M. Meier, A. Mekis, A. Dodabalapur, A. Timko, R.E. Slusher, J.D. Joannopoulos, 'Laser action from two-dimensional distributed feedback in photonic crystals', *Applied Physics Letters* **74**, 7 (1999).
 38. C. Bauer, H. Giessen, B. Schnabel, E.-B. Kley, C. Schmitt, U. Scherf, R.F. Mahrt, 'A Surface-Emitting Circular Grating Polymer Laser', *Advanced Materials* **13**, 1161 (2001).
 39. G.F. Barlow, K.A. Shore, G.A. Turnbull, I.D.W. Samuel, 'Design and analysis of a low-threshold polymer circular-grating distributed-feedback laser', *Journal of Optical Society of America B* **21**, 2142 (2004).

40. G.A. Turnbull, A. Carleton, A. Tahraoui, T.F. Krauss, I.D.W. Samuel, G.F. Barlow, K.A. Shore, 'Effect of gain localization in circular-grating distributed feedback lasers', *Applied Physics Letters* **87**, 201101 (2005).
41. J. Stehr, J. Crewett, F. Schindler, R. Sperling, G.V. Plessen, U. Lemmer, J.M. Lupton, T.A. Klar, J. Feldmann, A.W. Holleitner, M. Forster, U. Scherf, 'A Low Threshold Polymer Laser Based on Metallic Nanoparticle Gratings', *Advanced Materials* **15**, 1726 (2003).
42. R. Harbers, N. Moll, R.F. Mahrt, D. Erni, W. Bachtold, 'Enhancement of the mode coupling in photonic-crystal-based organic lasers', *Journal of optics A: Pure and Applied Optics* **7**, S230 (2005).
43. R. Harbers, P. Strasser, D. Caimi, R.F. Mahrt, N. Moll, B.J. Offrein, D. Erni, W. Bachtold, U. Scherf, 'Enhanced feedback in organic photonic-crystal lasers', *Applied Physics Letters* **87**, 151121 (2005).
44. M. Notomi, H. Suzuki, T. Tamamura, K. Edagawa, 'Lasing Action due to the Two-Dimensional Quasiperiodicity of Photonic Quasicrystals with a Penrose Lattice', *Physical Review Letters* **92**, 123906 (2004).
45. F.P. Schafer, 'Principles of Dye Laser Operation', *Dye Lasers, Topics in Applied Physics*, Springer-Verlag **1** (1990).
46. D. Moses, 'High quantum efficiency luminescence from a conducting polymer in solution: A novel polymer laser dye', *Applied Physics Letters* **60**, 3215 (1992).
47. D. Psaltis, S.R. Quake, C. Yang, 'Developing optofluidic technology through the fusion of microfluidics and optics', *Nature* **442**, 381 (2006).
48. D.-Y. Zhang, N. Justis, Y.-H. Lo, 'Fluidic adaptive lens of transformable lens type', *Applied Physics Letters* **84**, 4194 (2004).
49. S.C. McGreehin, T.F. Krauss, K. Dholakia, 'Integrated monolithic optical manipulation', *Lab on a Chip* **6**, 1122 (2006).
50. D. Erickson, T. Rockwood, T. Emery, A. Scherer, D. Psaltis, 'Nanofluidic tuning of photonic crystal circuits', *Optics Letters* **31**, 59 (2006).
51. D.V. Vezhenov, B.T. Mayers, R.S. Conroy, G.M. Whitesides, P.T. Snee, Y. Chan, D.G. Nocera, M.G. Bawendi, 'A low-threshold, high-efficiency microfluidic waveguide laser', *J. Am. Chem. Soc.* **127**, 8952 (2005).
52. H. Azzouz, L. Alkhafadiji, S. Balslev, J. Johansson, N.A. Mortensen, S. Nilsson, A. Kristensen, 'Levitated droplet dye laser', *Optics Express* **14**, 4374 (2006).
53. Z. Li, Z. Zhang, A. Scherer, D. Psaltis, 'Mechanically tunable optofluidic distributed feedback dye laser', *Optics Express* **14**, 10494 (2006).
54. S. Balslev, A. Mironov, D. Nilsson, A. Kristensen, 'Micro-fabricated single mode polymer dye laser', *Optics Express* **14**, 2170 (2006).
55. M. Gersborg-Hansen, A. Kristensen, 'Tunability of optofluidic distributed feedback dye lasers', *Optics Express* **15**, 137 (2007).
56. C. Monat, C. Seassal, X. Letartre, R. Regreny, P. Rojo-Romeo, P. Viktorovitch, M.L. D'Yerville, D. Cassagne, J.P. Albert, E. Jalaguier, S. Pocas, B. Aspar, 'InP-based two-

- dimensional photonic crystal on silicon: In-plane Bloch mode laser', *Applied Physics Letters* **81**, 5102 (2002).
57. J.M. Pottage, E. Silvestre, P. Russell, 'Vertical-cavity surface-emitting resonances in photonic crystal films', *Journal of the Optical Society of America* **18**, 442 (2001).
 58. G.T. Reed, A.P. Knights, 'Silicon Photonics: An Introduction', John Wiley, Chichester, West Sussex (2004).
 59. H. Rong, R. Jones, A. Liu, O. Cohen, D. Hak, A. Fang, M. Paniccia, 'A continuous-wave Raman silicon laser', *Nature* **433**, 725 (2005).
 60. S.G. Cloutier, P.A. Kossyrev, J. Xu, 'Optical gain and stimulated emission in periodic nanopatterned crystalline silicon', *Nature Materials* **4**, 887 (2005).
 61. L. Pavesi, L.D. Negro, C. Mazzoleni, G. Franzo, F. Priolo, 'Optical gain in silicon nanocrystals', *Nature* **408**, 441 (2000).
 62. M. Makarova, J. Vuckovic, H. Sanda, Y. Nishi, 'Silicon-based photonic crystal nanocavity light emitters', *Applied Physics Letters* **89**, 221101 1 (2006).
 63. H. Enner, G. Pomrenke, A. Axmann, K. Eisele, W. Haydl, J. Schneider, '1.54 μm electroluminescence from Er-doped silicon grown by molecular beam epitaxy', *Applied Physics Letters* **46**, 381 (1985).
 64. A.W. Fang, H. Park, O. Cohen, R. Jones, M.J. Paniccia, J.E. Bowers, 'Electrically pumped hybrid AlGaInAs-silicon evanescent laser', *Optics Express* **14**, 9203 (2006).
 65. P. Mach, M. Dolinski, K.W. Baldwin, J.A. Rogers, C. Kerbage, R.S. Windeler, B.J. Eggleton, 'Tunable microfluidic optical fiber', *Applied Physics Letters* **80**, 4294 (2002).
 66. N.M. Litchinitser, S.C. Dunn, P.E. Steinvurzel, B.J. Eggleton, T.P. White, R.C. Mcphedran, C.M.D. Sterke, 'Application of an ARROW model for designing tunable photonic devices', *Optics Express* **12**, 1540 (2004).
 67. T.T. Larsen, A. Bjarklev, D.S. Hermann, J. Broeng, 'Optical devices based on liquid crystal photonic bandgap fibres', *Optics Express* **11**, 2589 (2003).

CHAPTER 2:

The theory of organic semiconductor lasers

2.1 Introduction

Since 1960, when the first laser based on ruby as an active medium was realized, significant progress has been made on the design and engineering of lasers, primarily driven by the vast number of related applications. The acronym laser stands for ‘light amplification by stimulated emission of radiation’ and its realization was permitted by the interaction of photons with matter, as described by Einstein, in 1917. Such a device is comprised of two components, an optical amplifier and a resonator. The optical amplifier is responsible for the generation of photons via either an optical or an electrical excitation, while the resonator acts a feedback loop that forces the photons to travel several times through the amplifier and thus cause laser oscillation.

In this chapter, the focus will be on both of these essential components of a laser and how they are implemented in organic semiconductor lasers. The initial section focuses on the important aspects of the structure of conjugated molecules followed by how these relate to their electronic and optical properties. The types of resonators that have been used for this thesis will be analysed, laying the basis of the discussion that will follow. This analysis will be both qualitative and quantitative based on numerical tools that were developed for this thesis and will be described in more detail in chapter 3.

2.2 Electronic structure of conjugated molecules

The term conjugation describes a certain type of covalent bonding that can occur in both low molecular weight organic materials and polymers. In conjugated molecules, carbon atoms are connected through alternating single and double bonds and this structure gives rise to a series of attractive electronic and optical properties.

A double bond between two carbon atoms consists of one σ and one π -bond. A typical example of a molecule that contains such a bond is ethene (ethylene $\text{CH}_2 = \text{CH}_2$) and its bonding configuration is shown in figure 2.2.1. The three outer shell electrons of the two carbon atoms are sp^2 -hybridised giving three equivalent atomic trigonal orbitals in one plane that are axially symmetric and form 120° degrees with each other. The sp^2 orbitals are responsible for the formation of the backbone of the molecule: each carbon atom links to two hydrogen atoms through the overlap of the (Csp^2 , $\text{H}1\text{s}$) orbitals and the two CH_2 groups link through a (Csp^2 , Csp^2) overlap. In both cases the bond is a σ -bond. The remaining two p-orbitals of the carbon atoms are oriented in the plane perpendicular to the σ -bond and their overlapping is the origin of the formation of a π -bond [2]. The π -bond is responsible for a variety of properties, such as the *torsional rigidity* of a double bond but more importantly for the *electron delocalization* along the backbone of the molecule. In conjugated polymers, a series of conjugated units link with σ -bonds to form the chains that the polymer consists.

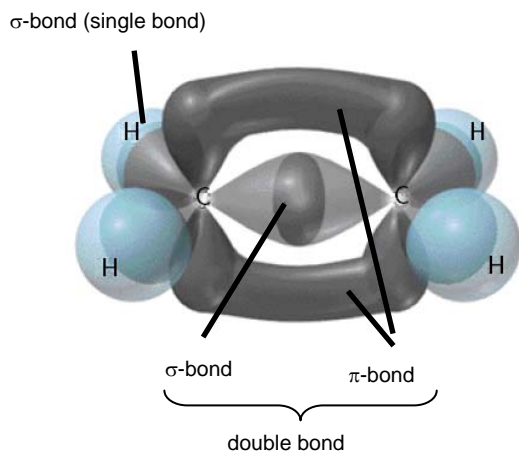


Figure 2.2.1: σ and π bonds from the overlap of the sp^2 and p orbitals of the two neighbouring carbon atoms in ethene. (Figure taken from <http://kekule.chem.csus.edu>).

The energy level diagrams of π -electron molecules can be estimated under the Hückel approximation and are shown in figure 2.2.2 for both ethene and a larger conjugated molecule of butadiene ($\text{CH}_2 = \text{CH} - \text{CH} = \text{CH}_2$).^{*} The number of the Hückel molecular energy levels is equal to the number of the p-orbital electrons. It is possible that the p-electrons of the neighboring carbon atoms interfere constructively or destructively depending on the signs of their wavefunctions. This in turn leads to the formation of bonding or antibonding π -orbitals respectively. When the bonding, or π orbitals are occupied, the energy of the molecule is lowered and in contrast destabilization occurs when the antibonding, or π^* orbital is occupied. The π - π^* orbitals form two pseudo-continua of energy levels separated by an energy gap. The highest energy π orbital is occupied by two electrons at thermal equilibrium and is referred to as *HOMO* (highest occupied molecular orbital). The antibonding orbital of the lowest energy is referred to as *LUMO* (lowest occupied molecular orbital).

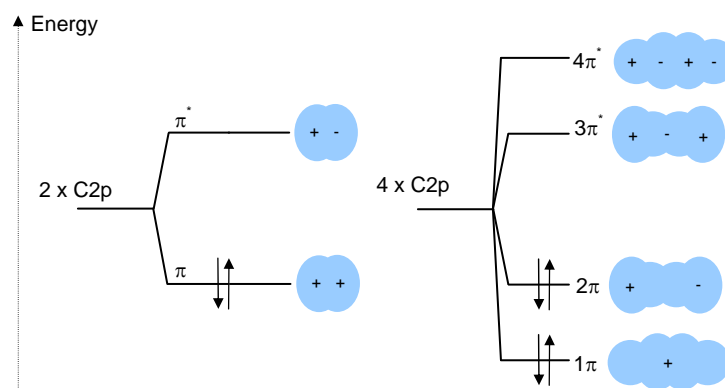


Figure 2.2.2: The Hückel molecular orbital energy levels for two or four carbon 2p orbitals link to either form ethene (*left*), or butadiene (*right*). In both cases, two electrons occupy the lowest available orbital (adapted from ref. 1).

The electronic structure in conjugated polymers is analogous to butadiene. A major difference is the higher number of orbitals, due to the increased number of double bonds (or p-electrons) within the repeat unit. Under the assumption of the weak electronic localization, when an electron is optically promoted from a bonding π to an

^{*} Under the Hückel approximation, the π - orbitals and σ -orbitals are separable and the latter are treated as a rigid framework responsible for the molecular geometry. In addition, all carbon atoms are treated as identical.

antibonding π^* orbital, the created electron – hole pair forms an exciton [3]. The exciton binding energy is relatively high (0.5 eV – 1.0 eV) in conjugated polymers both due to the short distance between the charges and the low dielectric constant of the medium [4]. These electrons and holes can be located on a single polymer chain (intrachain excitons) or shared between neighbouring segments (interchain excitons) [5]. Both can contribute to the polymer luminescence. The interchain excitons become important in the solid state where the distance between neighbouring polymer chains is small and their packing can play a significant role [3, 6, 7].

A second consequence of the electronic delocalisation is the existence of well-defined spin states: the singlet and the triplet [8]. The singlet and triplet states are defined as having an anti-symmetric or symmetric spin wavefunctions:

$$\text{Singlet: } \frac{1}{\sqrt{2}} \cdot [|\uparrow\downarrow\rangle - |\downarrow\uparrow\rangle] \quad \text{Triplet: } \frac{1}{\sqrt{2}} \cdot [|\uparrow\downarrow\rangle + |\downarrow\uparrow\rangle]$$

$$\begin{array}{c} |\uparrow\uparrow\rangle \\ |\downarrow\downarrow\rangle \end{array}$$

Spin conservation determines that transitions are allowed between states with the same spin condition (singlet-singlet, or triplet-triplet), whereas singlet-triplet transitions are forbidden.

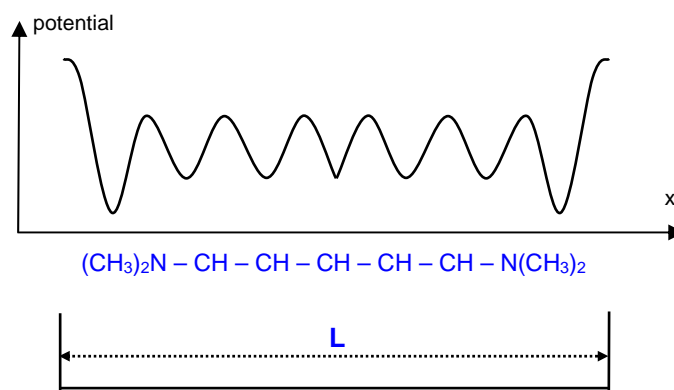


Figure 2.3.1: Free electron model for the electronic energy states of the cyanine dye (adapted from [1]). L is the conjugation length.

2.3 Optical properties of conjugated molecules

2.3.1 Absorption of light

The electronic structure of conjugated molecules determines their optical properties. The electronic π - π^* transitions are responsible for the absorption of photons of a resonant frequency that matches the energy gap between the π and π^* states. An example is the cyanine dye, in figure 2.3.1, where the free movement of the electrons along the molecule is approximated by electrons in a square quantum well [9]. The conjugation length of the molecule corresponds to the width of the well, the potential barriers of which are the methyl groups at either end of the molecule.

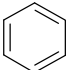
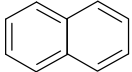
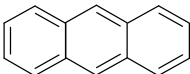
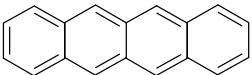
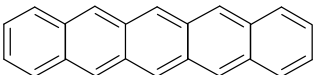
Molecule	Structure	Absorption Maximum
Benzene		255 nm
Napthalene		315 nm
Anthracene		380 nm
Tetracene		480 nm
Pentacene		580 nm

Figure 2.3.2: The wavelength of the absorption maximum for five different members of the family of polyacenes and their corresponding molecular structure showing the relevant conjugation length (adapted from ref. 8).

This is the free electron approximation, which in conjugated molecules exemplifies that it is the conjugation length (or the length of the chain of alternating single and double bonds) that determines the energy gap and consequently the wavelength of the absorption maximum. Chemical engineering of the molecular structure allows to

conveniently tune the optoelectronic properties of organic semiconductors. Figure 2.3.2 shows how the energy gap changes with the conjugation length in the family of polyacenes [8].

The interaction strength of the incident light with the organic medium is described by the Beer Lambert law, according to which the intensity of the incident light reduces exponentially with the thickness of the sample l and concentration of the absorbing species J [10]. The law is expressed as: $I_f = I_i \cdot e^{-\alpha \cdot [J] \cdot l}$, where α is the extinction coefficient that depends on the molecule and the frequency of the incident light.

2.3.2 Emission of light

The emission of light in conjugated molecules stems from the electronic excited states and is described best with the aid of the Jablonski diagram (figure 2.3.3) [11]. S_0 , S_1 , S_2 depict the ground, first and second singlet states, which in turn split to a series of vibronic states named as 0, 1, 2 etc. Absorption occurs typically from the lowest vibronic ground state energy to higher singlet states, which are unpopulated at thermal equilibrium. In accordance to the Frank Condon principle, the positions of the nuclei do not change during electronic transitions and consequently all transitions are vertical in the Jablonski diagram.

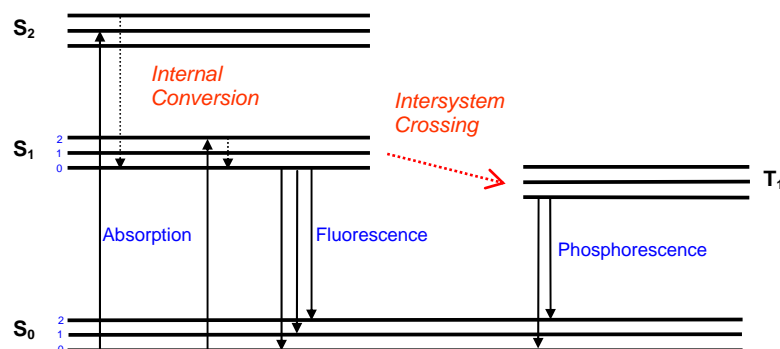


Figure 2.3.3: A Jablonski diagram for the depiction of the optical transitions in conjugated molecules.

Following absorption, the fluorophores are excited to either the S_1 or S_2 and then rapidly relax to the lowest vibrational level of S_1 by internal conversion and vibrational relaxation. Fluorescence occurs due to the transition from this electronic state to all the vibrational levels of the ground state. Molecules in S_1 can also undergo spin conversion to the first triplet state T_1 , a process referred to as intersystem crossing. Phosphorescence follows the transition from T_1 to S_0 . Whereas fluorescence lifetimes are typically in the range of a few nsec, phosphorescence, being a spin-forbidden process, is characterized by radiative lifetimes in the range of msec to seconds. The incorporation of heavy atoms (e.g. Ir) within the architecture of conjugated molecules facilitates the intersystem crossing and the phosphorescence rate increases. Representative molecules in this class are the organometallic complexes [12].

The 0-0 transition of the fluorescence is usually red-shifted with respect to the 0-0 transition of the absorption spectrum. This energy difference corresponds to the Stokes' shift and occurs mainly due to the change of the nuclei positions that follow the excitation. In comparison to the ground state, such changes in the molecular conformation result in a different excited state potential and occurs in significantly shorter timescales than the excited state lifetime. Other causes for the Stokes shift include the relaxation of the surrounding environment of the molecule (e.g. solvent) [13].

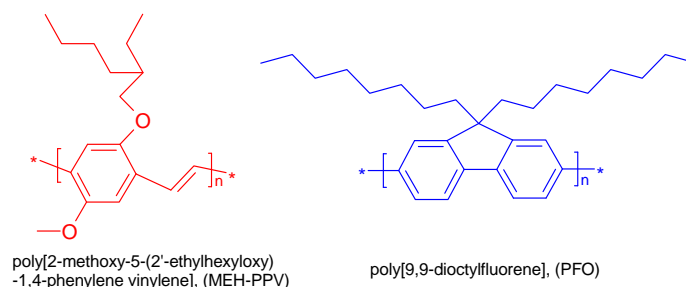


Figure 2.3.4: The chemical structure of some prototype conjugated polymers: the red emitting MEH-PPV and the violet emitting PFO.

In conjugated polymers (two prototypical materials are shown in figure 2.3.4) and in contrast to small molecules, there are additional energy relaxation mechanisms involved in light emission. One of these mechanisms is exciton migration and

contributes to the evident Stokes' shift observed in polymers. Exciton migration predominately occurs from short to longer conjugated segments. This effect has been studied by ultrafast time resolved photoluminescence showing that the time decay is significantly shorter at higher energies [14, 15]. In addition, exciton migration is responsible for the narrower emission spectrum in comparison to absorption and also for breaking the symmetry between them [16].

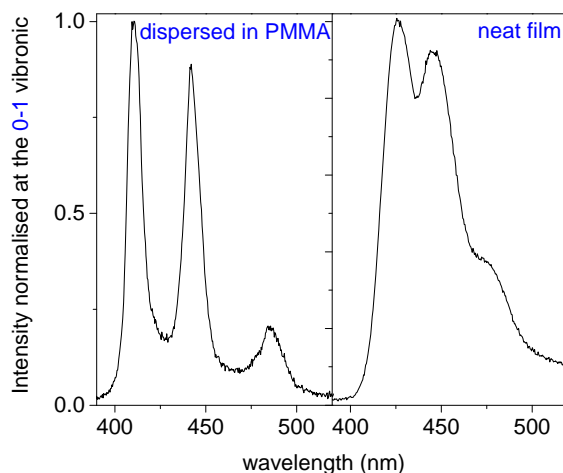


Figure 2.3.5: The photoluminescence of the conjugated polymer PFO when dispersed in PMMA and in neat film.

Intermolecular interactions are also considered responsible for the featureless emission and absorption spectra of conjugated polymers in the solid state. Electronic coupling between neighboring chains, as well as disorder can reduce the resolution of the vibronic peaks in the emission or absorption spectra. This effect is shown in figure 2.3.5 where the photoluminescence spectra for a neat PFO film (20 mg/ml chloroform) and PFO dispersed in PMMA (10^{-3} % wt.) are plotted. The low level of disorder in the dispersed PFO and the increased separation between neighbouring chains result in clear vibronic emission in contrast to the neat film. The level of disorder in polymer films depends on the conformational degrees of freedom of the repeat unit, which in turn depends on its molecular structure. A single molecule luminescence study involving two different conjugated polymers of different level of disorder revealed that the molecule exhibiting higher rigidity provided a much narrower distribution of peak energies by almost a factor of 4 [17]. Increased rigidity and reduced intermolecular

interactions can also increase the quantum efficiency of the conjugated system. This effect is shown in figure 2.3.6, where the PLQY values of a neat MEH-PPV film and films of MEH-PPV blended in polystyrene are plotted. The efficiency increases for decreasing concentration of the MEH-PPV in the solid matrix and reaches a maximum for a chromophore density of 1 wt. % [18]. This study illustrates the effect of the high chromophore density and the resulting increased intermolecular interactions on the photoluminescence quantum yield of the conjugated polymer MEH-PPV.

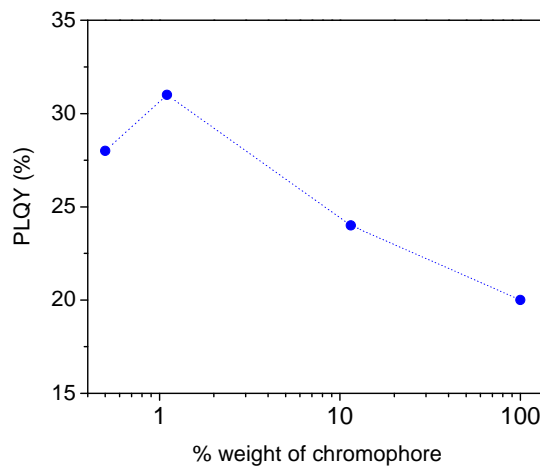


Figure 2.3.6: The photoluminescence quantum yield for a neat MEH-PPV films and blends of MEH-PPV with polystyrene.

2.3.3 Amplification of light

Population inversion is the necessary condition for light amplification through a medium. If a plane wave with a photon flux F travels through a two-energy level material and σ_{21} is the stimulated emission cross section of the medium, then the change of the photon flux dF of the wave when it propagates distance dz in the medium is [19]:

$$dF = \sigma_{21} \cdot F \cdot \left[N_2 - \left(\frac{g_2 \cdot N_1}{g_1} \right) \right] \cdot dz$$

Where the $N_{1,2}$ and $g_{1,2}$ are the populations and degeneracies of the levels 1 and 2 respectively. This relation implies that light amplification through a medium occurs when $N_2 > g_2 N_1/g_1$. This non-equilibrium condition is referred to as *population inversion*. Effectively, two-level atomic systems are inadequate for achieving laser emission due to the *two-level saturation*, where stimulated emission compensates for the absorption and transparency is reached [20]. On the contrary, 3- or 4- level systems can achieve population inversion

The electronic structure of organic semiconductors resembles that of a 4-level system and thus possesses the necessary optical properties for laser operation. The excited state events (figure 2.3.3) following pulsed optical excitation follow the route: molecules are excited from the electronic ground state S_0 into a Franck-Condon state S_{1-vib} . An ultra-fast vibrational ‘cooling’ to the lowest vibronic excited state S_{1-0} follows. Population inversion occurs between the S_{1-0} state and the highest vibronic levels of the ground state followed by a second thermalization process to the lowest vibronic level S_{0-0} [21]. Since the thermal relaxations are substantially faster (~ 10 fsec) than the radiative decay, a 4-level system is formed.

However, several mechanisms that can non-radiatively deplete the excited state population are present in organic semiconductors. These mechanisms reduce the population inversion and can vary depending on the material structure with significant implications in polymer lasers. These excited state decay mechanisms include:

1. The presence of ***chemical defects*** and ***impurities*** in a polymer, which can act as efficient photoluminescence quenchers. They were in fact the reason for the absence of gain in the early measurements of some polymers. A common quencher in conjugated polymers is the carbonyl group that is introduced during photooxidation. It is believed that these groups quench singlet exciton luminescence by fast charge transfer from the exciton to the carbonyl [22].

2. The ***exciton-exciton annihilation*** that occurs at high optical excitations due to collisions of mobile excitons, leading to multiple phonon emission and to the annihilation of at least one excitation [23]. It has been shown that the luminescence decay of thin films depends on the pump intensity and faster decay times are obtained for higher excitation densities [24]. Exciton-exciton annihilation can be reduced by spacing the polymer chains further apart [25].

Apart from the aforementioned intrinsic material losses, the optical gain also depends on the propagation losses within the organic film. These reduce the photon flux and consequently the net-gain. These types of losses include:

1. The ***ground state absorption*** due to the finite overlap between the absorption and emission spectrum. The emitted photons suffer from re-absorption as they propagate within an organic film hindering thus the amplification. This type of loss can be overcome by shifting the luminescence with respect to the absorption spectrum using guest-host techniques, where the emission spectrum of the host must overlap with the absorption of the guest molecule. The transfer mechanism is a non-radiative dipole-dipole interaction, namely Forster energy transfer, and has been experimentally demonstrated to lead to lower self-absorption and hence lower lasing thresholds [26, 27].

2. The ***photoinduced absorption***, which originates from the excited singlet and triplet state absorption, as well as absorption from the photogenerated carriers (polaron absorption). The excited state absorption occurs due to the promotion of singlet excitons to higher electronic states and can have a rather insignificant effect in conjugated polymers since its absorption peak is at a lower energy than the luminescence [28]. It is worth noting that this is not usually the case in organic dyes. The excited state absorption in organic semiconductors depends on the film morphology as shown in a comparative analysis performed in neat films of MEH-PPV and MEH-PPV dispersed in polystyrene or in solution [29].

In spite of these non-radiative decay processes and optical losses, organic molecules and especially conjugated polymers exhibit excellent amplification properties that usefully functionalise them as laser gain media. Chemical engineering of their molecular conformation can be employed to tune their emission spectrum, bandwidth and solubility. High stimulated absorption and emission cross-sections allow for very short cavity lengths (~ few hundreds of nanometers) to achieve lasing in optimized material combinations [30].

To this end, significant research has been focused on conjugated polymers and their applications as media for widely tuneable visible lasers. This type of organic media can exhibit high luminescence efficiency up to 50% if the polymer chain is designed so that interchain aggregates and chain defects are minimized [31]. The majority of the work has concentrated on derivatives of poly(paraphenylene-vinylene), poly(fluorene) and polythiophene [32-35]. Additionally, and in contrast to conventional dyes, polymers exhibit reduced concentration quenching of the luminescence, enabling the use of high chromophore densities [36].

One further advantage of organic molecules and in contrast to bulk inorganic semiconductors is their high exciton binding energy. This can be very attractive in terms of quantum electrodynamics, such as polariton effects both for laser and solid state lighting applications [37-39].

2.4 Resonators for organic lasers

Stimulated emission requires the excited atom to shift to a lower energy state when interacting with an incoming photon, resulting in the emission of a second photon of the same frequency, phase and polarization. Such a process is realized under population inversion conditions, assisted by the incorporation of the emitter within a resonator that forces the emitted photons to oscillate.

A significant number of resonators have been proposed and demonstrated for organic lasers. These cavities vary from Fabry-Perot resonators to more sophisticated nano-structured gain media. The purpose of this subsection is to describe the operating principles of the most common resonators that were studied for this thesis, laying thus the basis for the discussion that will follow.

2.4.1 Fabry Perot resonator

Historically, Fabry Perot (FP) cavities were the first demonstrated, while still remaining an important class of general purpose lasers [40]. The gain medium is placed between two reflecting interfaces, realized either by highly reflecting mirrors, or by the refractive index discontinuity at the boundary of the gain medium and the surrounding dielectric (figure 2.4.1). To a first approximation, the laser field is built from the superposition of two electromagnetic waves propagating in opposite directions along the cavity axis. The resonant frequencies are determined by the condition that the cavity length L must be equal to an integer multiple of half wavelengths. An alternative statement of the resonant condition is that the round-trip phase change must be an integer multiple of 2π : $e^{2\beta L} = 1$. A typical transmission spectrum for Fabry Perot resonator consisting of a 40 μm long MEH-PPV amplifier and 70% reflecting mirrors is shown in figure 2.4.1.

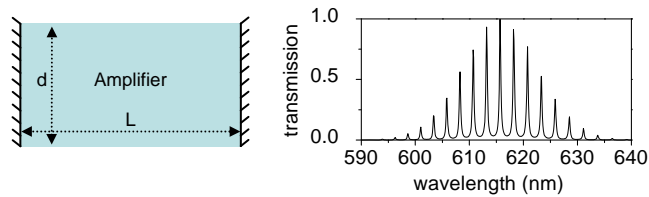


Figure 2.4.1 *Left:* Plane parallel Fabry Perot resonator. *Right:* The transmission of a Fabry Perot cavity: the amplifier is a MEH-PPV film and the end mirror reflectivity is 70%.

When determining the resonant frequencies of thin film based FP resonators, one needs to consider the propagation coefficients of the relevant transverse modes supported by the amplifier. To this end, the transverse dimension d and the refractive indices of the amplifier medium and the surrounding dielectric become important. The effective propagation constant and the number of the supported transverse modes will vary for different film thicknesses, altering thus the resonant condition. In figure 2.4.2 (a), this effect is illustrated for a freestanding MEH-PPV film at a wavelength of 630 nm. The propagation constant of fundamental transverse electric mode grows fast for increasing thicknesses saturating above a certain value, while above a certain thickness additional modes appear. Furthermore, the environment that surrounds the waveguide can also have a significant impact on the resonant condition. This is illustrated in figure 2.4.2 (b), where the propagation constant varies depending on whether the surrounding dielectric is air or silica. It is worth noting that for thicker films the two values converge indicating that the respective modes are more confined within the polymer film.

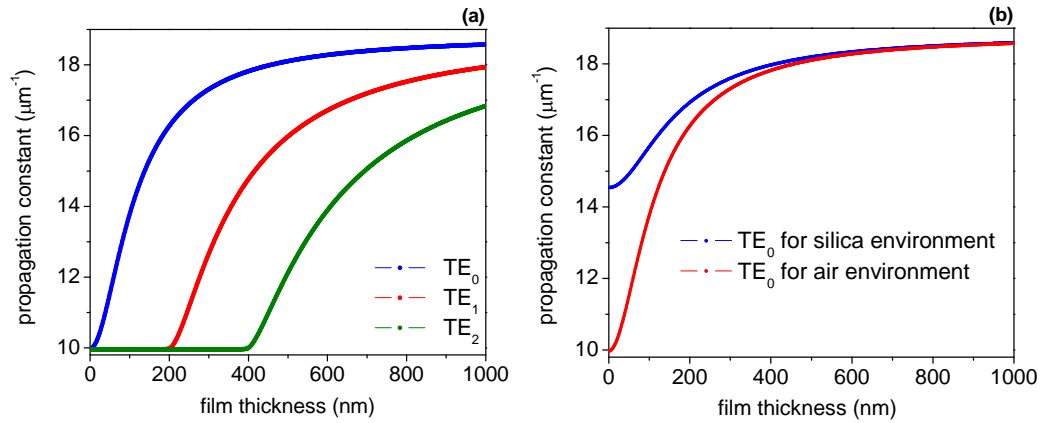


Figure 2.4.2 (a): The change of the propagation constant as a function of the waveguide thickness of a free standing MEH-PPV film for different order transverse electric modes. **(b):** The same effect for environments of different refractive indices.

In general Fabry Perot cavities represent several advantages, namely the simplicity of their design and fabrication, high output powers and small emitting areas that can easily match the numerical aperture of optical fibres [41]. However, there is a reciprocal relationship between long gain lengths and spectral purity. The cavity

lengths used so far are usually in the order of mm, imposing thus severe multimodality and hindering the laser performance and applications such as spectroscopy [42]. Different types of resonators have been employed in order to overcome this and achieve single frequency organic lasers.

2.4.2 Distributed Feedback resonator

Several polymer lasers have been demonstrated in the Distributed Feedback (DFB) configuration. The motivation behind this research is their low threshold operation, collimated emission, increased design versatility in terms of feedback and output coupling directions and the prospect of simple fabrication via nano-imprint lithography [43-45]. The operation of such microstructures is based on the periodic modulation of the refractive index of a thin polymer film, spun on top of a diffraction grating (figure 2.4.3). In the contemporary literature, diffractive nanostructures are alternatively referred to as photonic crystals, or more generally as Metamaterials [46].



Figure 2.4.3: The elevation (left) and plan view (right) of a one-dimensional polymer periodic structure; the cover and surrounding areas are air.

Periodic structures are characterised by translational symmetry, which for one-dimensional periodicity states that the medium ‘looks’ the same at x and at $x+\Lambda$, where Λ is the lattice constant. In comparison to isotropic structures, the radiation field in periodically stratified media exhibits certain special features. One way to visualise these is the imaging capacity of light, which in periodic structures can only occur via interference, or formation of standing waves [47]. This process requires several plane waves to interact and the cause of this interaction is the periodic perturbation of the dielectric constant, or grating momentum. The condition for this to occur is the

wavelength of the incident light to be equal (or close) to an integer multiple of the periodicity of the stratified medium.

The interference condition is dictated by the Bragg condition: $n \cdot \lambda/2 = n_{\text{eff}} \cdot \Lambda$, where λ is the wavelength, n_{eff} is the effective index and n an integer. For a certain optical period but different values of the integer n , this condition is satisfied for different wavelengths. The effect of the wavelength and the diffraction order on the distribution of the standing waves can be calculated by the Plane Wave Expansion method (PWEM) [48] and is illustrated in figure 2.4.4: for a certain wavelength the light *localises* $n/2$ times within a single period.

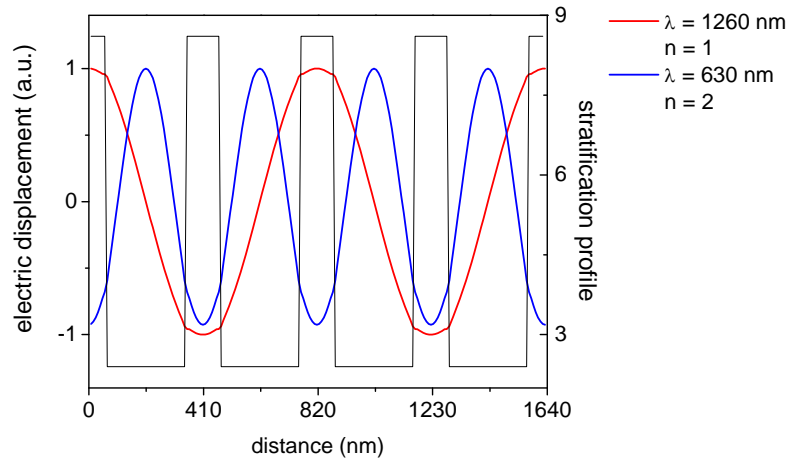


Figure 2.4.4: The electric field distribution of FB waves for different orders of diffraction and wavelengths in a stratified medium with period of 410 nm and an effective index contrast of 0.09.

In analogy to plane waves in a slab waveguide, the interfered harmonics comprise the respective Floquet-Bloch (FB) waves in periodic media [47]. FB waves behave in a similar fashion to plane waves, with some exciting exceptions such as negative refraction [49]. In the transverse direction to the propagation plane, total internal reflection confines the light and can be analysed as in the case of thin films (see Fabry Perot section) [50]. The formation of FB waves is the basis of operation of DFB lasers, or Bloch lasers [51, 52].

So far, it was assumed that a mode of a wavelength that satisfies the Bragg condition propagates within the periodic structure. Even if this is not explicitly valid, it has been previously employed to determine the operating wavelength of a polymer DFB laser [53]. In effect, the mode corresponding to the Bragg wavelength is evanescent forming a photonic stop-band [54]. The dispersion relationship $\omega = c \cdot \kappa$ illustrates the stop band, where for a certain optical frequency ω , the wavevector κ of the Bloch waves becomes imaginary. In figure 2.4.5 such a dispersion relationship is shown for a thin MEH-PPV film (120 nm thick) on a silica grating of a period 410 nm and fill factor 70% (PWEM). On the same y-axis, the respective reflectivity spectrum is plotted to illustrate the coincidence of the stop band with the wavelengths that experience high reflectivity. The calculation of the reflectivity spectrum was performed using the Transfer Matrix Method (TMM) [54].

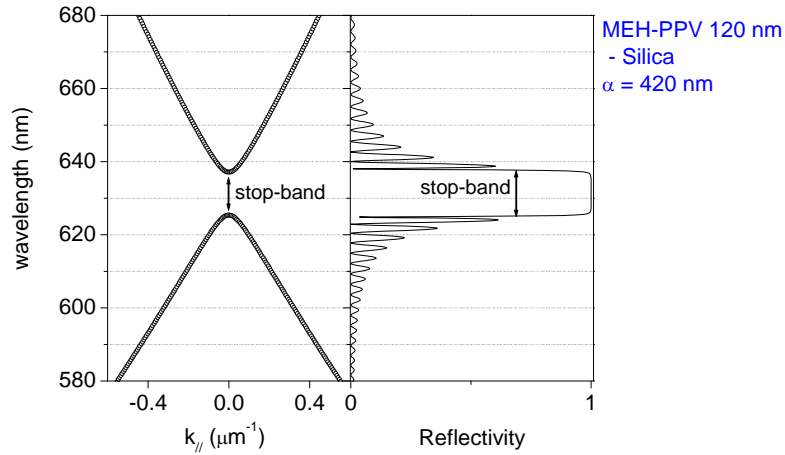


Figure 2.4.5: The dispersion relationship of a periodic medium (see text), along with the reflectivity spectra on the same y-axis.

In regards to DFB lasers, the modes at the edge of the stop-band are the ones that experience significant feedback and thus are more likely to reach threshold. These optical waves travelling in one direction are continuously scattered into an optical wave in the reverse direction, growing in intensity due to both the gain and the distributed reflectivity. As the gain increases in the structure (by increasing the optical excitation density for example) one of the modes will start growing faster than the background emission denoting the threshold. This effect is illustrated in figure 2.4.6, which shows the sum of the transmitted and reflected intensities of light incident on

the DFB structure. The gain in the structure is accounted for by the imaginary part of the refractive index ε'' [55]. For $\varepsilon'' = 0$, the sum is 1 and for higher values of ε'' the band-edge mode at 630 nm grows > 1 , which is the effect of stimulated emission.

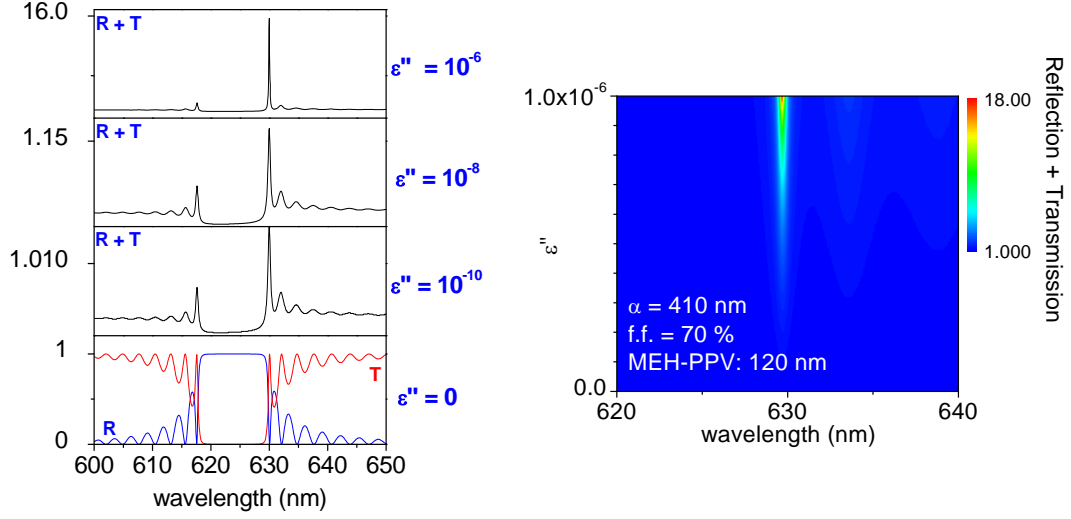


Figure 2.4.6: *Left:* The sum of the transmittance and the reflectance for a DFB polymer laser, for increasing gain in the material and light parallel to the grating vector. *Right:* The same calculation, plotted in 3D graph.

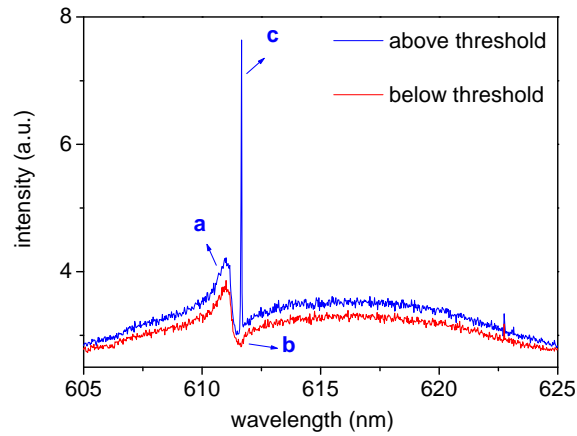


Figure 2.4.7: The emission spectrum of an organic DFB laser below and above threshold. The stop-band is the intensity dip (b).

Experimentally, the effect of the stop-band can be observed in the emission spectrum. Figure 2.4.7 shows such a spectrum for an organic DFB laser based on a dye-doped polystyrene gain medium [18]. The spectrum exhibits three features, namely a band-edge mode (a), the stop-band (b) and the lasing band-edge mode (c). The short wavelength band-edge mode (a) experiences an increased photon density as denoted

by its increased intensity and in contrast the stop-band is represented by a characteristic intensity dip in the spectrum. The long wavelength band-edge mode experiences reduced coupling to free space radiation and thus higher net gain. This is why the long wavelength mode reaches threshold first [56].

It is clear from the preceding analysis that by employing the frequency selectivity inherent in diffractive nanostructures, the issue of single frequency operation in polymer lasers can be addressed. It is also possible to use gratings where the diffracted wave is radiated away from the polymer guide. Second order gratings are of particular note because they can be used to couple light from the laser in a direction perpendicular to the surface forming thus a surface-emitting laser [57]. Recent work has also shown several interesting phenomena occurring when the gain is correlated with the periodicity of a metamaterial, namely the gain enhancement due to a ‘group velocity anomaly’ at the edges of the stop band and the ‘gain anisotropy’ [58-60].

2.4.3 Distributed Bragg reflector resonator

In distributed Bragg reflector lasers (DBR) the amplifying medium is placed between two Bragg mirrors that provide the necessary feedback for lasing (figure 2.4.8). In contrast to DFB lasers that consist of a uniform grating area, DBR lasers operate within the stop-band due to the break of the grating symmetry induced by the presence of a structural defect. They operate in a similar fashion to Fabry-Perot cavities, but with the advantage that the distributed reflection mirrors give significant feedback only around the Bragg frequency. Due to the narrow reflectivity bandwidth the presence of several longitudinal modes can be avoided.

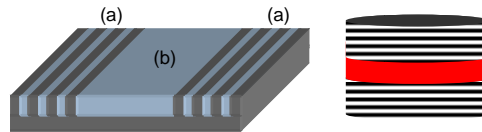


Figure 2.4.8: *Left:* Diagram of a distributed Bragg reflector laser. *Right:* A schematic of an organic VCSEL. Sections (a) correspond to Bragg grating reflectors and (b) to the optical gain medium.

Such organic lasers have been demonstrated in the past, with the mirror separation being relatively large and in the order of mm [61, 62]. They were realised in a thin polymer film configuration imposing thus the consideration of the effective propagation constant as mentioned in the section of Fabry-Perot resonators. A lot of attention has also been focused on similar structures, namely the organic VCSEL type of lasers (or microcavities) that nonetheless entail certain drawbacks, such as the additional step of the top mirror deposition but also the short gain length limited by the thickness of the organic film [63, 64].

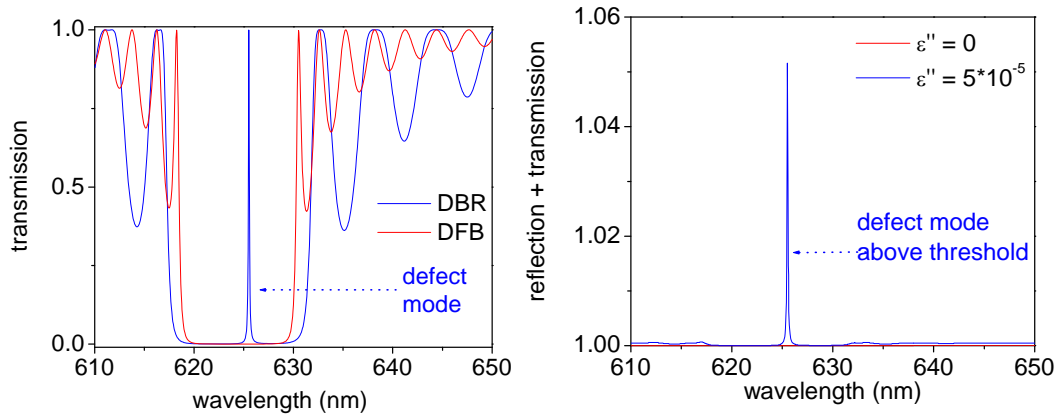


Figure 2.4.9: *Left:* The transmission spectra for a DFB and a DBR including a 260 nm long defect section. *Right:* The sum of the reflection and transmission of the DBR for increasing gain in the structure. For both the DFB and DBR, the period was 420 nm, the fill factor 30 % and the polymer was a 120 nm MEH-PPV thick film.

The operation of DBR cavities can also be described with the aid of the transmission, or reflection spectra. The introduction of a defect in between the mirrors manifests itself via an additional high transmission peak within the stop-band. This is shown in figure 2.4.9 (TMM), where the transmission is plotted for a uniform Bragg stack and for a DBR with a defect of 260 nm long; the additional transmission peak corresponds to a mode that is mostly localized within the defect and thus referred to as ‘defect mode’. The number of defect modes and their position within the stop-band spectrum can be controlled by the width of the defect. Regarding laser action in DBR cavities, it is the defect mode that will reach threshold when population inversion occurs within the defect area. The depiction of stimulated emission is in the right of figure 2.4.9: for

increasing gain within the cavity the sum of transmittance and reflection grows to values higher than one for the wavelength that corresponds to the defect mode.

The motivation behind DBR polymer laser research has mainly been the capability of separating the amplification region (defect) with the Bragg gratings. The latter can act as a source of loss due to the surface roughness associated with the spinning of a polymer film on top of a corrugated substrate [65]. In addition, the volume of the polymer material within the defect can absorb more efficiently the pump excitation. The argument supporting this is the fact that due to the absence of the silica corrugation the chromophore density is much higher in the defect area than in DFB lasers, where the volume of the polymer is limited by the fill factor. In addition, increased Purcell factors (p. 91) can be realized in such devices due to the coexistence of increased Q-factor modes, but also limited modal volumes [66].

2.5 References

1. A. Kavokin, I. Shelykh, G. Malpuech, 'Optical Tamm states for the fabrication of polariton lasers', *Applied Physics Letters* **87**, 261105 (2005).
2. P.W. Atkins, 'Physical Chemistry', 3rd Edition, 393 (1986).
3. I. D. W. Samuel, G. Rambles, C.J. Collison, 'Efficient interchain photoluminescence in high-electron-affinity conjugated polymers', *Physical Review B* **52**, R11 573 (1995).
4. R.H. Friend, 'Charges and Excitons at Interfaces in Polymeric Semiconductor Structure', in *International Conference on the Science and Technology of Synthetic Metals*, Dublin (2006).
5. J.M. Lupton, PhD thesis: Nanoengineering of organic light emitting diodes, University of Durham, (2002).
6. M. Yan, L.J. Rothberg, E.W. Kwock, T.M. Miller, 'Interchain Excitations in Conjugated Polymers', *Physical Review Letters* **75**, 1992 (1995).
7. N.T. Harrison, D.R. Baigent, I.D.W. Samuel, R.H. Friend, A.C. Grimsdale, S.C. Moratti, A.B. Holmes, 'Site Selective Studies of poly(p-phenylene vinylene) and its derivatives', *Physical Review B* **53**, 15815 (1996).
8. W. Butting, *Physics of organic semiconductors*, Wiley-VCH Verlag GmbH, Weinheim, 6 (2005).

9. F.P. Schafer, Principles of Dye Laser Operation, in Topics in Applied Physics, Dye Lasers, Springer-Verlag (1990).
10. P.W. Atkins, 'Physical Chemistry', 3rd Edition, 464 (1986).
11. J.R. Lakowicz, 'Principles of Fluorescence Spectroscopy', Kluwer Academic, New York, (1999).
12. E.B. Namdas, A. Ruseckas, I.D.W. Samuel, S. Lo, P.L. Burn, 'Photophysics of Fac-Tris(2-Phenylpyridine) Iridium(III) Cored Electroluminescent', Journal of Physical Chemistry B **108**, 1570 (2004).
13. G.G. Stokes, 'On the Change of Refrangibility of Light', Philosophical Transactions of the Royal Society of London **142**, 463 (1852).
14. R. Kersting, U. Lemmer, R.F. Mahrt, H. Kurz, H. Bassler, O.E. Gobel, 'Femtosecond Energy Relaxation in p-Conjugated Polymers', Physical Review Letters **70**, 3820 (1993).
15. B. Mollay, U. Lemmer, R. Kersting, R.F. Mahrt, H. Kurz, H.F. Kauffmann, H. Bassler, 'Dynamics of Singlet Excitations in Conjugated Polymers: Poly(phenylenevinylene) and Poly(phenylphenylenevinylene)', Physical Review B **50**, 10769 (1994).
16. G.R. Hayes, I.D.W. Samuel, R.T. Phillips, 'Exciton Dynamics in Electroluminescent Polymers Studied by Femtosecond Time-Resolved Photoluminescence Spectroscopy', Physical Review B **52**, 11569 (1995).
17. F. Schindler, J. Lupton, J. Feldmann, U. Scherf, 'A Universal Picture of Chromophores in p-Conjugated Polymers Derived from Single-Molecule Spectroscopy', Proceedings of the National Academy of Sciences (PNAS) **101**, 14695 (2004).
18. M. Alvarez, A. E. Vasdekis, G. A. Turnbull, 'Comparison of the operating characteristics of conjugated polymer and solid-state dye distributed feedback lasers', Journal of Applied Physics, in preparation (2007).
19. O. Svelto, Principles of Lasers, Plenum Press (1998).
20. G. I. Papadopoulos, F.P. Palikari, Quantum optics and Lasers, University of Athens (2002).
21. B. Schweitzer, G. Wegmann, H. Giessen, D. Hertel, H. Bassler, R. F. Mahrt, 'The optical gain mechanism in solid conjugated polymers', Applied Physics Letters **72**, 2933 (1998).
22. G. J. Denton, N. Tessler, N. T. Harrison, R. H. Friend, 'Factors influencing stimulated emission from Poly(p-phenylenevinylene)', Physical Review Letters **78**, 733 (1997).
23. R.H. Friend, D.D.C. Bradley, P.D. Townsend, 'Photo-excitation in conjugated polymers', Journal of Physics D: Applied Physics **20**, 1367 (1987).
24. I.D.W. Samuel, G. Rumbles, C.J. Collison, R.H. Friend, S.C. Moratti, A.B. Holmes, 'Picosecond Time-Resolved Photoluminescence of PPV Derivatives', Synthetic Metals **84**, 497 (1997).
25. A. Ruseckas, M. Theander, L. Valkunasb, M.R. Andersson, O. Inganäs, 'Energy transfer in a conjugated polymer with reduced inter-chain coupling', Journal of Luminescence **76 & 77**, 474 (1998).

26. R. Gupta, M. Stevenson, A. J. Heeger, 'Low threshold distributed feedback lasers fabricated from blends of conjugated polymers: Reduced losses through Forster transfer', *Journal of Applied Physics* **92**, 4874 (2002).
27. A.K. Sheridan, A.R. Buckley, A. M. Fox, A. Bacher, D. D. C. Bradley, I. D. W. Samuel, 'Efficient Energy Transfer in Organic Thin Films-Implications for Organic Lasers', *Journal of Applied Physics* **92**, 6367 (2002).
28. R. Osterbacka, W. Wohlgenannt, D. Chin, Z. V. Vardeny, 'Optical studies of triplet excitations in poly(p-phenylene vinylene)', *Physical Review B* **60**, 11253 (1999).
29. M.D. McGehee, A.J. Heeger, 'Semiconducting (Conjugated) polymers as materials for solid state lasers', *Advanced Materials* **12**, 1655 (2000).
30. V. Bulovic, V.G. Kozlov, V. B. Khalfin, S. R. Forrest, 'Transform-limited, narrow-linewidth lasing action in organic semiconductor microcavities', *Science* **279**, 553 (1998).
31. U. Scherf, S. Riechel, U. Lemmer, R. F. Mahrt, 'Conjugated polymers: lasing and stimulated emission', *Current Opinion in Solid State & Material Science* **5**, 143 (2001).
32. G. Heliotis, D.D.C. Bradley, G.A. Turnbull, I.D.W. Samuel, 'Light amplification and gain in polyfluorene waveguides', *Applied Physics Letters* **81**, 415 (2002).
33. F. Hide, M.A. Diaz-Garcia, B.J. Schwartz, M.R. Andersson, Q. Pei, A.J. Heeger, 'Semiconducting polymers: a new class of solid-state laser materials', *Science* **273**, 1883 (1996).
34. T. Granlund, M. Theander, M. Berggren, M. Andersson, A. Ruzeckas, V. Sundstrom, G. Bjork, M. Granstrom, O. Inganas, 'A polythiophene microcavity laser', *Chemical Physics Letters* **288**, 879 (1998).
35. T. Granlund, M. Theander, M. Berggren, M. Andersson, A. Ruzeckas, V. Sundstrom, G. Bjork, M. Granstrom, O. Inganas, 'Corrigendum to: "A polythiophene microcavity laser"', *Chemical Physics Letters* **310**, 577 (1999).
36. G.A. Turnbull, 'Lasers: Organic Semiconductors, Polymers', *Encyclopedia of Modern Optics* Elsevier (2004).
37. J.R. Tischler, M.S. Bradley, V. Bulovic, 'Strong coupling in a microcavity LED', *Physical Review Letters* **95**, 036401 (2005).
38. R.F. Oulton, N. Takada, J. Koe, P.N. Stavrinou, D.D.C. Bradley, 'Strong coupling in organic semiconductor microcavities', *Semiconductor Science and Technology* **18**, S419 (2003).
39. A. Kavokin, I. Shelykh, G. Malpuech, 'Optical Tamm states for the fabrication of polariton lasers', *Applied Physics Letters* **87**, 261105 (2005).
40. A.L. Schawlow, C.H. Townes, 'Infrared and optical masers', *Physical Review B* **112**, 1940 (1958).
41. N. Tessler, G.J. Denton, R.H. Friend, 'Lasing from conjugated-polymer microcavities', *Nature* **382**, 695 (1996).
42. V.G. Kozlov, V. Bulovic, P.E. Burrows, M. Baldo, V.B. Khalfin, G. Parthasarathy, S.R. Forrest, Y. You, M.E. Thompson, 'Study of lasing action based on Forster energy transfer in

- optically pumped organic semiconductor thin films', *Journal of Applied Physics* **84**, 4096 (1998).
43. G.A. Turnbull, P. Andrew, W.L. Barnes, I.D.W. Samuel, 'Operating characteristics of a semiconducting polymer laser pumped by a microchip laser', *Applied Physics Letters* **82**, 313 (2003).
 44. J.R. Lawrence, P. Andrew, W.L. Barnes, M. Buck, G.A. Turnbull, I.D.W. Samuel, 'Optical properties of a light-emitting polymer directly patterned by soft lithography', *Applied Physics Letters* **81**, 1955 (2002).
 45. A.E. Vasdekis, G.A. Turnbull, I.D.W. Samuel, G.E. Town, 'Novel diffractive feedback structures for semiconducting polymer lasers', *Proc. SPIE Int. Soc. Opt. Eng.* **5937**, 311 (2005).
 46. J. Pendry, 'Metamaterials, negative refraction and a new design paradigm in optics,' in *Photon 06*, Manchester (2006).
 47. P.S. Russell, 'Photonic Band-Gaps', *Physics World* **5**, 37 (1992).
 48. S.P. Guo, S. Albin, 'Simple plane wave implementation for photonic crystal calculations', *Optics Express* **11**, 167 (2003).
 49. A. Berrier, M. Mulot, M. Swillo, M. Qiu, L. Thylen, A. Talneau, S. Anand, 'Negative refraction at infrared wavelengths in a two-dimensional photonic crystal', *Physical Review Letters* **93**, 073902 (2004).
 50. E. Chow, S.Y. Lin, S.G. Johnson, P.R. Villeneuve, J.D. Joannopoulos, J.R. Wendt, G.A. Vawter, W. Zubrzycki, H. Hou, A. Alleman, 'Three-dimensional control of light in a two-dimensional photonic crystal slab', *Nature* **407**, 983 (2000).
 51. C. Monat, C. Seassal, X. Letartre, R. Regreny, P. Rojo-Romeo, P. Viktorovitch, M.L. D'Yerville, D. Cassagne, J.P. Albert, E. Jalaguier, S. Pocas, B. Aspar, 'InP-based two-dimensional photonic crystal on silicon: In-plane Bloch mode laser', *Applied Physics Letters* **81**, 5102 (2002).
 52. M. Imada, S. Noda, A. Chutinan, T. Tokuda, M. Murata, G. Sasaki, 'Coherent two-dimensional lasing action in surface-emitting laser with triangular-lattice photonic crystal structure', *Applied Physics Letters* **75**, 316 (1999).
 53. W. Holzer, A. Penzkofer, T. Pertsch, N. Danz, A. Brauer, E.B. Kley, H. Tillmann, C. Bader, H.H. Horhold, 'Corrugated neat thin-film conjugated polymer distributed-feedback lasers', *Applied Physics B-Lasers and Optics* **74**, 333 (2002).
 54. A. Yariv, P. Yeh, 'Optical waves in crystals', Wiley, New Jersey (2003).
 55. K. Sakoda, *Optical properties of photonic crystals*, Springer-Verlag, Berlin (2001).
 56. G.A. Turnbull, P. Andrew, M.J. Jory, W.L. Barnes, I.D.W. Samuel, 'Relationship between photonic band structure and emission characteristics of a polymer distributed feedback laser', *Physical Review B* **12**, 6412 (2001).
 57. M. Imada, S. Noda, A. Chutinan, T. Tokuda, M. Murata, G. Sasaki, 'Coherent two-dimensional lasing action in surface-emitting laser with triangular-lattice photonic crystal structure', *Applied Physics Letters* **75**, 316 (1999).

58. P. St. J. Russell, T.A. Birks, 'Bloch wave optics in photonic crystals: physics and applications', in Photonic Band Gap materials, K.A. Publishers (1996).
59. J.P. Dowling, M. Scalora, M.J. Bloemer, C.M. Bowden, 'The Photonic Band-Edge Laser - a New Approach to Gain Enhancement', Journal of Applied Physics **75**, 1896 (1994).
60. S. Nojima, 'Enhancement of optical gain in two-dimensional photonic crystal with active lattice points.' Japanese Journal of Applied Physics **37**, L565 (1998).
61. I.P. Kaminow, H.P. Weber, E.A. Chandros, 'Poly(Methyl Methacrylate) Dye Laser with Internal Diffraction Grating Resonator', Applied Physics Letters **18**, 497 (1971).
62. M. Berggren, A. Dodabalapur, R.E. Slusher, 'Stimulated emission and lasing in dye-doped organic thin films with Forster transfer', Applied Physics Letters **71**, 2230 (1997).
63. V. Bulovic, V.G. Kozlov, V.B. Khalfin, S.R. Forrest, 'Transform-limited, narrow-linewidth lasing action in organic semiconductor microcavities', Science **279**, 553 (1998).
64. L. Persano, P. Del Carro, E. Mele, R. Cingolani, D. Pisignano, M. Zavelani-Rossi, S. Longhi, G. Lanzani, 'Monolithic polymer microcavity lasers with on-top evaporated dielectric mirrors', Applied Physics Letters **88**, 12 (2006).
65. A.E. Vasdekis, G. Tsiminis, J.-C. Ribierre, Liam O' Faolain, T. F. Krauss, G.A. Turnbull, I.D.W. Samuel, 'Diode pumped distributed Bragg reflector lasers based on a dye-to-polymer energy transfer blend', Optics Express **14**, 9211 (2006).
66. A.M. Adawi, A. Cadby, L.G. Connolly, W.C. Hung, R. Dean, A. Tahraoui, A.M. Fox, A.G. Cullis, D. Sanvitto, M.S. Skolnick, D.G. Lidzey, 'Spontaneous emission control in micropillar cavities containing a fluorescent molecular dye', Advanced Materials **18**, 742 (2006).

CHAPTER 3:

Methodology

3.1 Introduction

The necessary components of microstructured polymer lasers are a transparent and periodically corrugated substrate, a thin conjugated polymer film and a pulsed laser source for their optical excitation. In this chapter, the methodologies for the design, fabrication and characterisation of lasers based on microstructured polymer thin films will be described. The fabrication technique of this type of structures was based on the electron beam lithography and to this end, I developed a certain fabrication process for fused silica, which is outlined in section 3.2. In this way, it has been possible to investigate several types of periodic feedback lattices, contributing significantly to the optimisation steps of polymer microstructured lasers. Section 3.3 describes the ellipsometric investigations that I made in order to determine the optical constants of the organic gain media used, but also the exact thicknesses of the films involved in the laser structures. These values have been of significant importance, especially in the context of designing and characterising polymer lasers the basic rules of which will be outlined in section 3.4. In the context of the fluidic fibre lasers, the relevant preparation and characterisation methodology is relevantly simple and hence will be outlined separately in chapter 6.

3.2 Micro-resonator fabrication

Electron beam lithography was used to define most of the micro-resonators studied in this thesis. The first fabrication step of the microstructured substrates for polymer lasers, involves the pattern design using a CAD (Computer Aided Design) software. This pattern is subsequently transferred to a thin resist layer that covers the substrate (typically polymethyl(methacrylate), PMMA) using the electron beam radiation. After development and removal of the exposed resist sections, the pattern is transferred from the resist into the silica substrate using reactive ion etching (RIE), typically based on fluorine. The final step of the grating preparation involves an ultrasonic bath in a polar solvent (acetone for example) to remove the resist residue. An overview of the fabrication process is shown in figure 3.2.1.

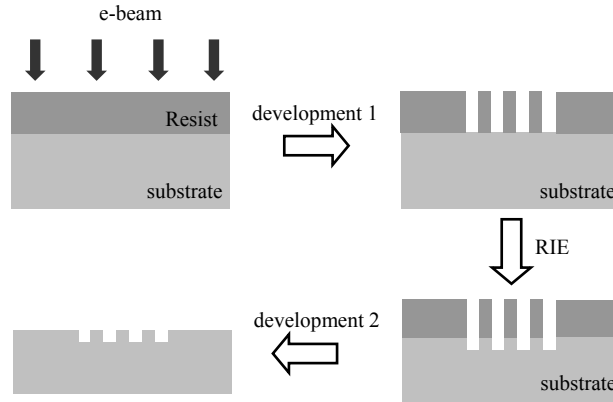


Figure 3.2.1: An overview of the fabrication of the diffractive feedback gratings in fused silica.

In the majority of the experiments, the substrate was a fused silica sample with dimensions $25 \times 25 \times 1 \text{ mm}^3$.^{*} The motivation for this choice of material is its low refractive index compared to most conjugated polymers, allowing the formation of polymer waveguides. The size of the substrate was relatively large, in comparison to similar experiments in photonic crystal research, as the requirement of a uniform polymer film had to be met, which becomes more difficult to achieve using spin-coating when the size of the substrate decreases. In addition, the large size of the substrate allowed for the definition of several devices on a single sample, hence

^{*} The fused silica substrates were purchased from Heraeus Silica and Metals Limited (U.K.).

enabling comparative studies of different cavities under similar experimental conditions. Several challenges had to be addressed in order to fabricate structures of substantially small feature sizes. These involved managing the insulating properties of fused silica that limit the lithographic resolution, the mechanical stability of the exposed features (adhesion) and the backscattering of the electron beam that imposed an additional variation of the features' size. Specific techniques were thus developed to overcome these problems.

3.2.1 Electron beam lithography

Electron beam lithography is a unique technique for the definition of extremely fine patterns on almost every kind of surface, ranging from semiconductors to dielectrics and metals. The requirements for these fine structures were initially posed by the electronics industry with the demand for decreasing size integrated circuits in accordance to Moore's law. In contrast to optical lithography, the level of resolution is greatly enhanced by employing electrons instead of photons. The reason for this enhancement is the wavelength of the radiation involved in each case: in optical lithography, the typical wavelength used is ~ 248 nm, but the de Broglie wavelength of electrons is much shorter (typically in the pm range), thus significantly increasing the possible resolution. A schematic e-beam system is shown in figure 3.2.2.

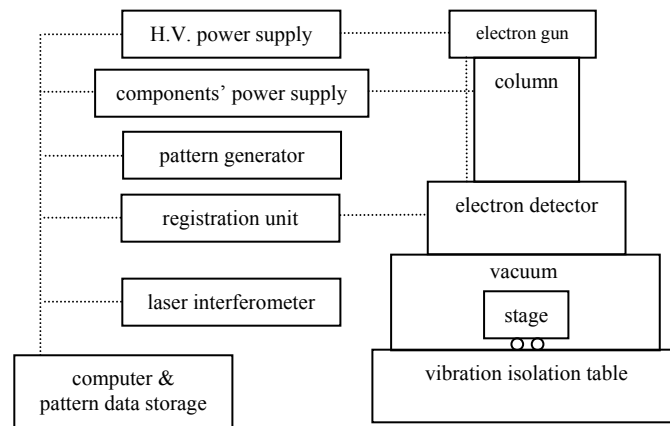


Figure 3.2.2: A block diagram illustrating the major components of an electron beam lithography system (reproduced after [1]).

The most common electron beam lithography systems are based on standard scanning electron microscopes. However, the quest for high throughput has lead to the development of expensive and complex dedicated lithography systems, the price of which can exceed the range of 3M GBP. In brief, the technique consists of scanning a beam of electrons across the surface of a sample covered with a resist film sensitive to the electrons' radiation. In this way, the beam deposits energy on certain areas of the resist and thus a pattern is defined on its surface. The core of the system is the column that consists of an electron source and the control elements for the electron beam (lenses, stigmators, blankers, detectors etc.). Underneath the column, the sample is mounted on a translation stage, the position of which is controlled by a laser interferometer. Both the sample and the column operate under ultra-high vacuum. A complex set of electronics, which supplies the signal and power to the various components, completes the system. The complexity of the electron beam lithography stems from the electron-solid interactions involved during the exposure. Upon penetrating the resist, electrons experience several small-angle scattering events that tend to decrease the resolution of the exposure. These manifest themselves via the broadening of the incident electron beam diameter and is referred to as forward scattering [1]. Subsequent to the resist, the electrons penetrate the substrate and undergo large-angle scattering events (backscattering). This affects the size of an exposed feature, since the dose it receives is increased due to backscattered electrons from a nearby feature. The latter is the proximity effect and the simplest way to control against it is to modulate the dose during the exposure and in accordance to the shape-shape interactions that are involved.

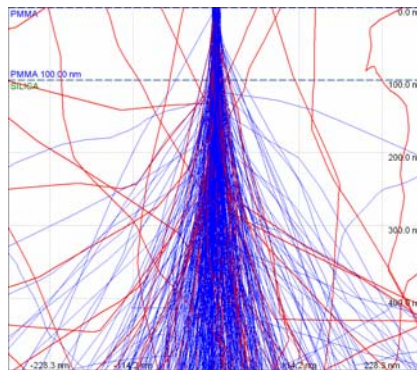


Figure 3.2.3: A Monte-Carlo simulation of electron scattering in a PMMA resist on fused silica.

These two types of interactions are illustrated in figure 3.2.3. This graph was produced by a Monte Carlo simulation of electron scattering in a typical sample of the ones used throughout the thesis: a thin layer of e-beam resist, i.e. polymethyl(methacrylate) (PMMA) on fused silica [2]. The trajectories of the forward propagating electrons are displayed in blue, while the backscattered electrons are shown in red. It can be observed that backscattering events occur only when the electron beam enters the substrate. Additionally, in comparison to the top surface of the resist, the electron beam has broadened significantly when arriving at the substrate surface, which is the limiting factor of the resolution. The increase in the effective beam diameter due to forward scattering is given by the following empirical formula, which shows how the resist thickness limits the attainable resolution [1]:

$$d_f = 0.9 \cdot \left(\frac{\text{resist thickness (nm)}}{\text{beam voltage (kV)}} \right)^{1.5} \quad (3.1)$$

3.2.2 Pattern transfer

Electron beam resists are divided mainly into two categories, the positive tone resists, such as the PMMA and the negative tone ones, such as the SU₈ and the flowable oxide Hydrogen Silsesquioxane (FOX-12). The difference between positive and negative tone resists originates from their molecular structure, in that the electron radiation results in chain scission and chain connection between two neighbouring polymer segments, respectively [3].

Understanding the exposure mechanism is important, because following the pattern definition by electron beam lithography, the sample is developed to remove the soluble exposed areas in positive tone resists, while in negative tone ones it is the unexposed areas that are soluble and thus removed. For the purpose of this thesis, the positive resist PMMA was most frequently used. The patterned resist forms an etch mask, which is used to transfer the pattern into the substrate using reactive ion etching (RIE).

During the RIE, the sample is placed in a vacuum chamber that is subsequently filled with an appropriate, relatively inert process gas. The application of a high RF Voltage leads to ionisation of the gas and thus the formation of a glow discharge. For the etching of fused silica that was primarily used in this work, CF₄ gas was chosen. It dissociates in the plasma as follows [4]:



The plasma formation also creates a boundary surface region on the sample's surface, referred to as the *sheath*. The sheath is characterised by high electric fields of such polarity that accelerates the positive ions, or molecular radicals towards the surface, while negative ions and electrons are kept away [4]. Successful etching takes place when the chemically reactive species formed by the gas dissociation interact with the solid and form very volatile products. During the fused silica etching, the fluorine gas reacts readily with the Si atoms of the wafer to form SiF₄. The latter is a gas at room temperature and thus can be conveniently pumped away.

During the etching process of fused silica, both the substrate and the PMMA are eroded by the plasma with similar rates (aspect ratio 1:1). Consequently, care must be taken to use a sufficiently thick mask, and not to over-etch the resist, which risks decreasing the quality of the surface of the sample. The poor etch selectivity of PMMA sets an upper limit to the depth of the nanostructure that is limited by the resist thickness, which is typically 140 nm.

3.2.3 Nanostructured silica fabrication for polymer lasers

The aforementioned processes of pattern definition and transfer were employed to create the gratings necessary for the operation of nanostructured polymer lasers. The substrate material primarily employed was fused silica and the electron beam resist

was PMMA. It is remarkable that since the first report on the excellent qualities of PMMA as an electron beam resist and despite the development of a plethora of positive and negative tone resists, most of the relevant work continues to be done with PMMA [5]. The electron beam lithography tool used was a Hybrid LEO Gemini 1530 SEM/RAITH ELPHY lithography system, with a maximum acceleration voltage of 30 kV.

The specifics of this particular fabrication process will be outlined in this section. Several challenges were met during the development of the fabrication procedure. First of all, the silica substrate is an electrical insulator, so the exposure with a beam of charged electrons leads to local charge density increase. These charging problems had to be overcome in order to both decrease the set-up time of the lithography but also to be able to view the fabricated nanostructures. The resist thickness was also found to play an important role in the adhesion problem that causes the poor quality of some gratings. Finally, the proximity correction was found to be of utmost importance in the fabrication of distributed Bragg reflector resonators, where the interface between the defect area and the mirror grating is very prone to defect creation.

(a) Charge dissipation

One way to address the charging problem is to form a multilayer structure, where apart from the resist other layers are added that act as effective discharge layers [6]. This approach was followed throughout the thesis. The charge dissipation layer used initially was a thin Al layer that was evaporated on top of the PMMA resist. Prior to development, the Al layer was removed in a bath of Orthophosphoric acid. In many cases, the Al layer remained on the surface after the development step, increasing the probability of failed fabrication.

A different method involved the formation of a multilayer structure consisting of a thin (~ 20 nm) conductive polymer referred to as PEDOT*, a thin sputtered Au film (~ 15 nm) and the PMMA resist (figure 3.2.1) [7]. The advantage of this method is that in the vast majority of the experiments both of the charge dissipation layers were readily removed. PEDOT is water-soluble and thus was removed after the second development step (figure 3.2.1). During this step, the sputtered Au was also removed due to its poor bonding to the surface of the PMMA. The usage of these two layers allowed a significantly higher resolution lithography since the setting up of the process was both easier and at much higher magnifications.

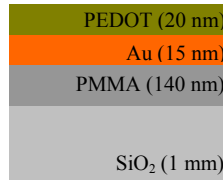


Figure 3.2.4: A cross sectional view of the multilayer structure used to overcome the charging problem.

Figure 3.2.5 shows a scanning electron microscopy image of two different samples. The left one is covered only with PMMA, while the right has additionally the aforementioned layers. It is obvious that the imaging contrast is substantially improved.

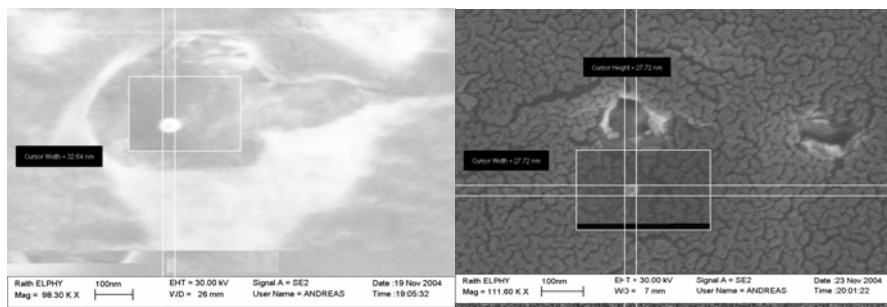


Figure 3.2.5: *Left:* An SEM image taken during the exposure set-up for a sample of PMMA on fused silica. *Right:* The same conditions for the sample of figure 3.2.4

In addition, imaging an insulating sample becomes impossible at high magnifications. To this end, adding a thin PEDOT layer is also very useful, as it is water-soluble and

* The type of PEDOT used was the BAYTRON P VP.AI 4083 (H.C. Starck, Germany).

thus does not leave any permanent traces on the sample. It is worth mentioning that only water soluble conducting polymers can be used in this manner, as any other method, such as sputtering or evaporating thin metal layers, would result in a permanent extra layer on top of the structure [7, 8]. Image 3.2.6 illustrates such an advantage; the left image was taken from a sample that was not covered with any extra charge dissipating layers and the right one is covered with a thin PEDOT layer. The difference in quality is obvious since the right image does not suffer from any distortions stemming from irregular brightness or contrast.

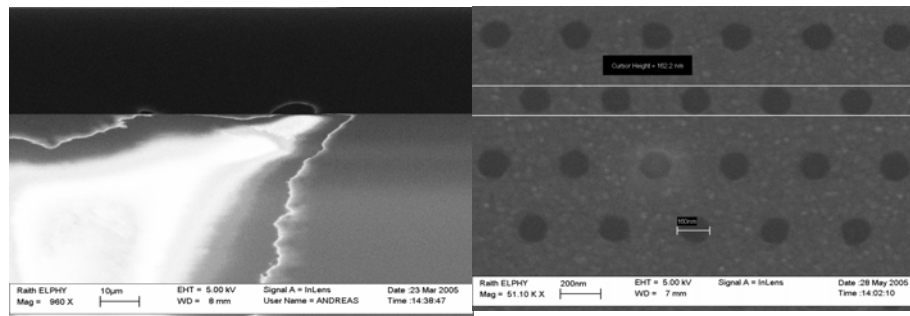


Figure 3.2.6: *Left:* An SEM image of a grating without PEDOT. *Right:* A triangular photonic crystal lattice in fused silica imaged at high magnifications using PEDOT.

(b) Adhesion

The forward small-angle scattering events that occur during the propagation of the electron beam within the resist lead to broadening of the beam as mentioned in section 3.2.1. This can result in non-vertical resist sidewalls and thus mechanically unstable features that eventually could collapse. This effect is referred to as adhesion. Adhesion becomes more profound in linear grating structures, where the volume of a single feature can be relative large with typical values of $\sim 1 \mu\text{m}^3$. Figure 3.2.7 illustrates a linear grating structure suffering from adhesion: upon developing and etching, the grating lines collapse resulting in poor quality of the nanostructure.

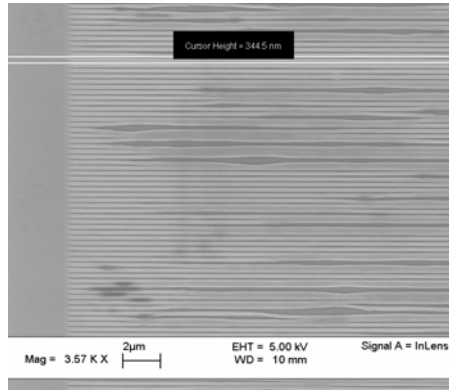


Figure 3.2.7: An electron beam defined grating suffering from adhesion: some grating lines come in contact with the neighbouring features severely decreasing the quality of the structure.

As depicted by the empirical relationship 3.1, the beam broadening effect depends on the resist thickness and the acceleration voltage of the column. The acceleration voltage is system limited and the maximum possible value was employed throughout these experiments (30 kV). I conducted a study to identify the effect of the resist thickness on the resolution by exposing single pixel lines on samples of different PMMA film thickness. For a certain resist thickness, the width of the exposed areas increases for increasing exposure doses (figure 3.2.8), while for a certain exposure dose, the width of the exposed areas will be different for different resist thicknesses, indicative of the beam broadening effect involved. In such an experiment, the adhesion can be identified by comparing the rate of change of the width of the exposed areas versus the exposure dose for different film thicknesses. A range of gratings of different periods was exposed to study the effect of the distance between neighbouring features.

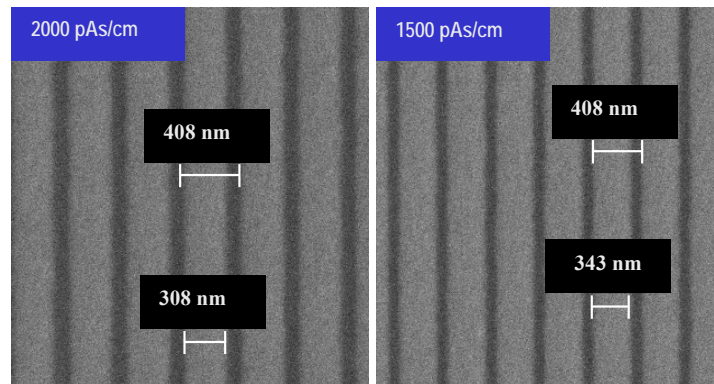


Figure 3.2.8: SEM images for a linear silica grating of 408 nm period, illustrating the dose effect on the width of the exposed area for a PMMA thickness of 140 nm.

Figure 3.2.9 depicts the results, where it can be seen that the rate is lower for thinner PMMA films indicating that adhesion is less significant. For example, for a grating with a period of 200 nm (*right*) that received a dose of 700 pAs/cm, the exposed line-width is 96 nm for resist thicknesses of 300 nm, while for a resist thickness of 140 nm the respective width was 51 nm. The reduced width of an exposed area for the same dose, but thinner resist, indicates the decreased level of adhesion present during fabrication. It can be also observed that the difference between the slopes of the two thicknesses is higher for a lattice constant of 200 nm (*right*) than for period of 408 nm (*left*), indicating that adhesion becomes more significant for smaller features.

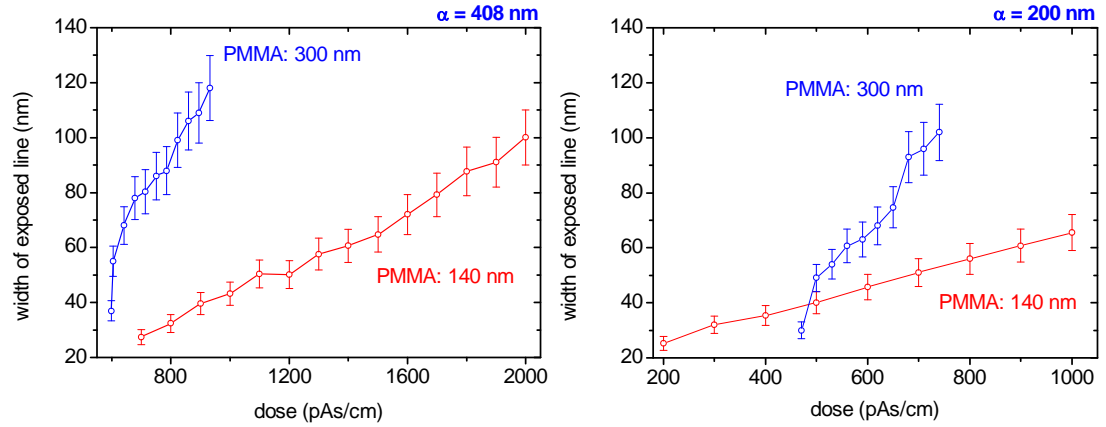


Figure 3.2.9: The effect of the dose on the width of single pixel exposed lines for two different resist thicknesses. On the *left*, the grating period is 408 nm and on the *right* the grating period is 200 nm.

By employing thinner resist, higher control is gained against adhesion but the grating structures can't be deeper than the PMMA thickness due to the poor etching selectivity between PMMA and fused silica. Hence, the 140 nm PMMA thick film was chosen because this is the maximum etch depth required for the gratings for polymer lasers. A 140 nm thick film of most conjugated polymers supports only the fundamental transverse electric mode, allowing thus for increased gain of the lasing mode.

(c) Proximity correction

The backscattered electrons can cause a distortion in the transferred pattern, especially in areas where the feature density is higher, or on the border between two different structures. Both of these effects are shown in figure 3.2.10, for a square lattice diffraction grating and for linear grating in the proximity of an etched slab waveguide. In the case of the square lattice photonic crystal, the central parts of the exposed areas receive a higher dose than the edges as indicated by their larger diameter. In regards to the linear grating, this has received a higher dose at its edges due to the exposure of the adjacent slab waveguide.

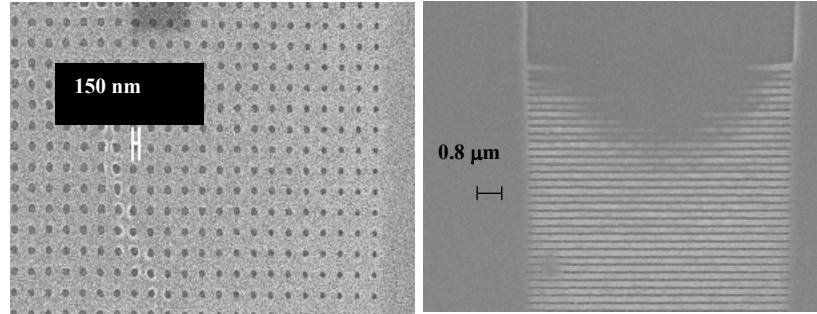


Figure 3.2.10: *Left:* a square lattice diffraction grating not proximity-corrected. *Right:* an etched slab waveguide causing significant distortion to a linear grating causing in its proximity.

Calculating the exposure dose that each feature receives and varying it accordingly to compensate against the unavoidable excess of dose can correct both of these defects. The proximity correction calculation can be performed by the software package accompanying the lithography system. To do so, certain parameters enter the calculation that depend on the substrate and resist material used. These parameters are the range of forward scattering (α), the range of backward scattering (β) and the ratio of the forward to backward scattered electrons (η). These parameters can define the dose as a function of position through the following relationship:

$$p(r) = \frac{1}{\pi (1 + \eta)} \cdot \left[\frac{1}{\alpha^2} e^{-\frac{r^2}{\alpha^2}} + \frac{\eta}{\beta^2} e^{-\frac{r^2}{\beta^2}} \right] \quad (3.3)$$

To determine the proximity correction parameters, the doughnut method is used [9]. A matrix of rings with varying inner diameter and dose, but constant outer diameter was fabricated on PMMA on fused silica. The two variables are varied in an orthogonal fashion: the dose varying across the y-axis, while the inner diameter across the x-axis. By identifying the dose D at which each column receives the clearing dose, the proximity correction factors (α , β and η) can be identified by fitting against them and D_0 using the following relationship [10]:

$$D = \frac{D_0 \cdot (1 + \eta)}{\exp[-R_1^2/\alpha^2] + \eta \cdot \exp[-R_1^2/\beta^2]} \quad (3.4)$$

Figure 3.2.11 depicts the results of this study, where the aforementioned parameters were measured to be $\alpha = 0.4$ nm, $\beta = 1.065$ nm and $\eta = 0.001$. By employing these values, the proximity correction can take place by modulating the dose accordingly.

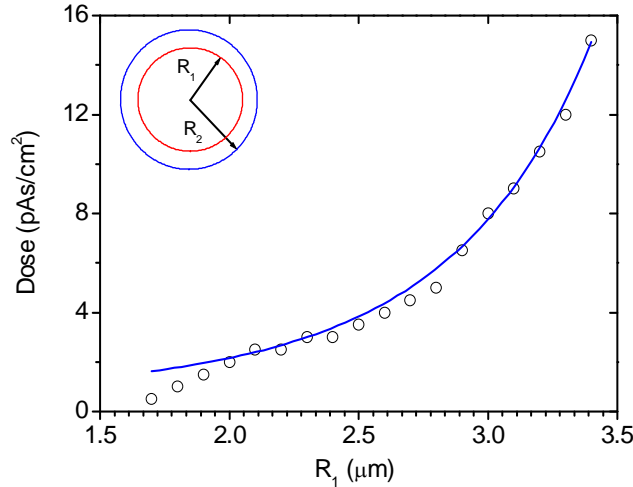


Figure 3.2.11: The variation of the clearing dose for certain inner ring diameter.

An indicative structure is shown in figure 3.2.12. The structure is a linear grating with a period of 408 nm, including a line defect of 930 nm. Such a structure is extremely prone to proximity effects, especially at the edges of the defect. The successful application of the proximity correction allowed for the definition of a uniformly linear defect, but also for a constant fill factor across the structure.

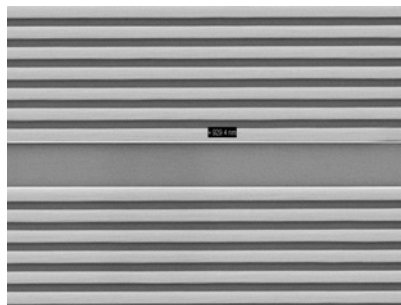


Figure 3.2.12: A linear grating including a defect structure, proximity corrected.

3.3 Ellipsometry

3.3.1 Introduction

Ellipsometry is a contact-less and thus non-destructive tool for measuring the thickness and the optical constants of thin films. There are no restrictions in the material composition of the measured films and thus ellipsometry has been proven as a useful tool with applications ranging from organic and polymer films to in-situ monitoring of semiconductor growth. The experiments performed for this thesis were based on a commercial apparatus purchased from J. A. Wollam Co., Inc (M-2000DI).

The sample is mounted on a translation stage and held there by vacuum. The measurement involves the illumination of the sample at different angles with a linearly polarised, broadband source. The polarised radiation has its two orthogonal electric field components perpendicular and parallel to the plane of incidence with a phase difference equal to zero. The reflection spectrum from the sample surface is detected with a spectrometer and a rotating analyser determines its polarisation state. A generic schematic of the apparatus is shown in figure 3.3.1.

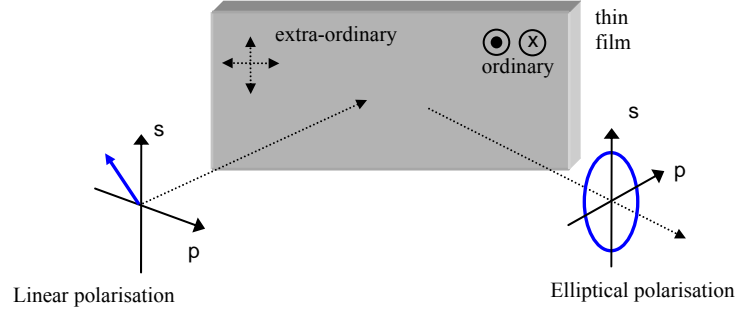


Figure 3.3.1: A simplified schematic of the ellipsometry apparatus.

The experiment involves the measurement of the change of the polarisation state upon reflection that depends on the optical constants and the thickness of the thin film. This change is determined by the change in amplitude (Ψ) of the s- and p-polarisation of the reflected beam and the difference in their phase (Δ). They both depend on the Fresnel reflection coefficients for s- and p-polarized light:

$$\frac{R_p}{R_s} = \tan(\Psi) \cdot e^{i\Delta} \quad (3.5)$$

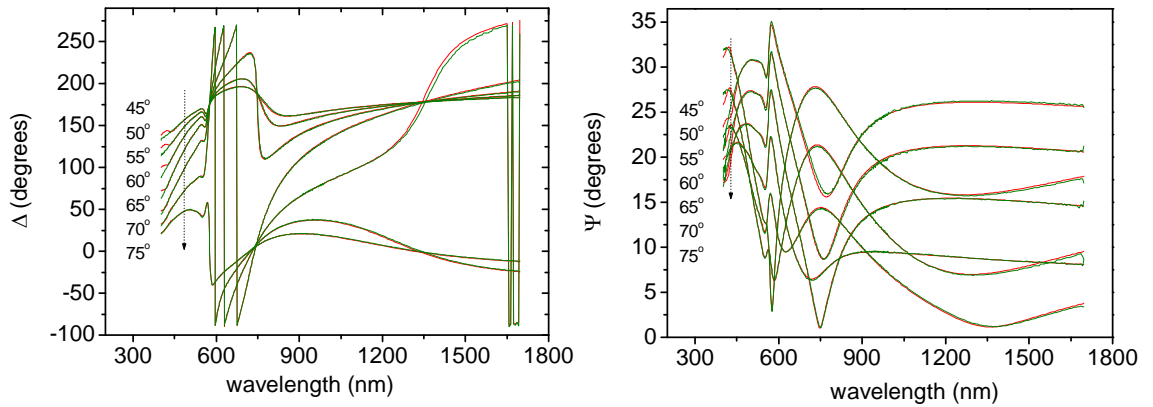


Figure 3.3.2: The experimental Ψ and Δ values in red as measured for the different angles; the regression results in black.

Having measured the Ψ and Δ at different illumination angles, a regression analysis is carried out in which the dielectric function and the thickness of the film are the fitting parameters.* The objective is to construct a material model that its calculated response of Ψ and Δ will match the experimental values. Typical experimental and fitting results

* The regression follows the Levenberg-Marquart algorithm.

are shown in figure 3.3.2 that corresponds to a thin film of the conjugated polymer MEH-PPV on a spectrocil substrate. The first task is to determine the film thickness in the transparent spectral region using a Cauchy model [11]. The Cauchy model can also describe a uniaxial material system, accounting thus for the ordinary and extraordinary indices of refraction corresponding to light polarised parallel and perpendicular to the plane of the film. During this step, an initial estimation of the optical constants is also obtained that is used in the subsequent step of the point by point fit in the entire spectral region.

The final step involves the construction of a parameterized model and the fitting of this model with the optical constants obtained from the point-by-point fit. The parameterisation involves the inclusion of oscillators corresponding to the absorbing region of the spectrum. In this way, the obtained optical constants are consistent with the Kramers – Kronig relationship. It has been useful to ensure that the generated absorption spectra match the experimental ones measured with an absorption spectrometer [12]. A typical result of a measurement and regression is shown in figure 3.3.3 for a thin film of amorphous Si on SiO₂.

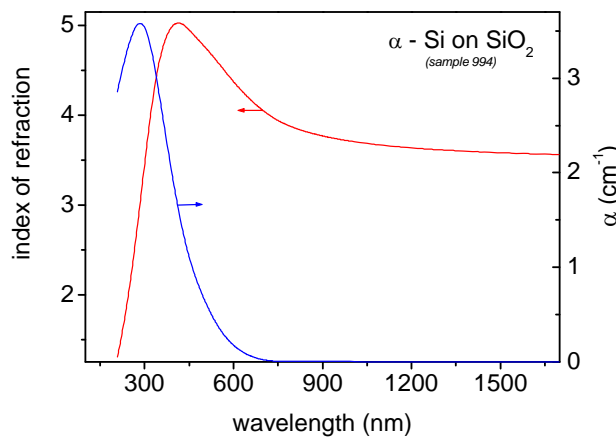


Figure 3.3.3: Typical results of the optical constants (both real and imaginary) of a thin film of amorphous Si grown on SiO₂ (the sample was provided by E. Rafailov, University of Dundee).

3.3.2 Ellipsometric investigations

Ellipsometry has proven an extremely useful tool in investigating the quality of several processing steps during the grating fabrication. For example it was used to find that during reactive ion etching the plasma is not uniform across the sample's surface. This is attributed to edge effects and its magnitude was characterised for Si etching on a SOI sample (Si on insulator) using ellipsometry. The sample was etched to remove the Si epilayer using SF_6 and CHF_3 chemistry, under certain conditions of voltage and gas pressure. The differential etch rate resulted in a substantial thickness variation of the epilayer across the sample surface. The results are shown in figure 3.3.4 for the two axes of the sample. The etch rate in the centre of the sample was lower than the edges resulting in 85 % thickness difference.

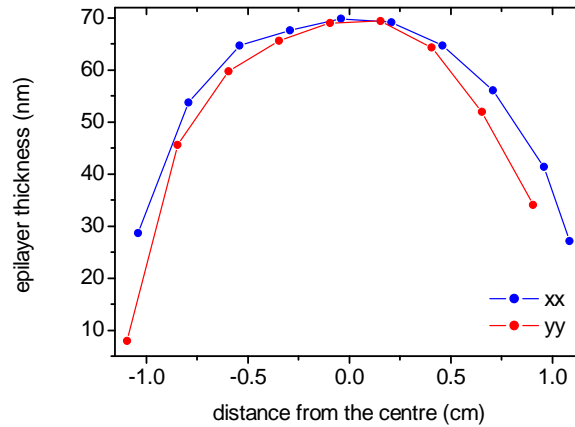


Figure 3.3.4: The Si epilayer thickness variation measured across the surface of the sample. The remaining epilayer thickness variation is indicative of the differential etch rate due to surface effects (the sample was provided by Steven Moore).

Ellipsometric measurements were also performed in order to identify the refractive indices of the materials involved in the laser fabrication. Two prototypical-conjugated polymers that were frequently used were measured: MEH-PPV (poly(2-methoxy-5-(2'-ethyl-hexyloxy)-p-phenyl-enevinylene)) and PFO (poly[9.9-dioctylfluorene]). The measurements were performed for film thicknesses $\sim 150 - 200\text{nm}$ and their dispersion is shown in figure 3.3.5 in good agreement with the literature [13, 14]. The measurements indicated the birefringent nature of conjugated films and the ordinary index values were accurately determined at the wavelengths of the gain maximum that

is of interest for lasing in a single transverse electric (TE) waveguide modes. In addition, two possible solid matrices were investigated, namely polystyrene and PMMA and their indices of refraction are plotted in figure 3.3.6 (*left*). This type of materials has been used in the context of dye-doped gain media.

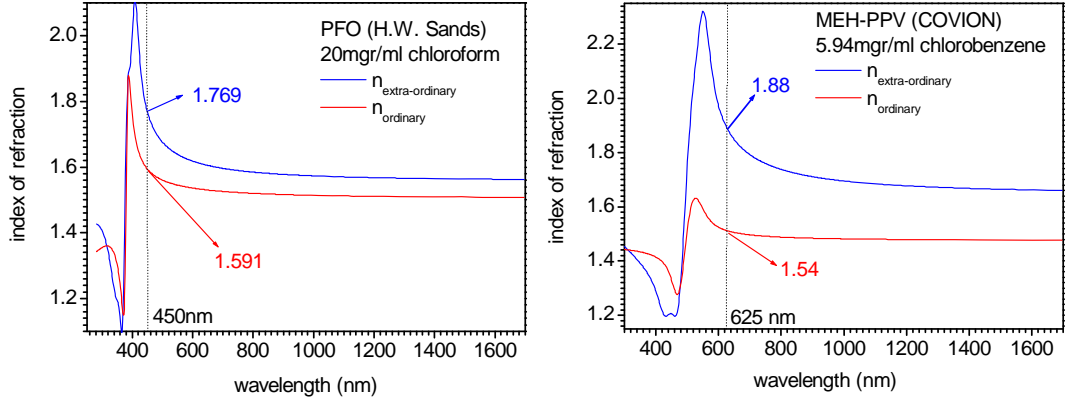


Figure 3.3.5: The material dispersion curves for PFO (left) and MEH-PPV (right). The ordinary and extra-ordinary curves are shown in red and blue respectively.

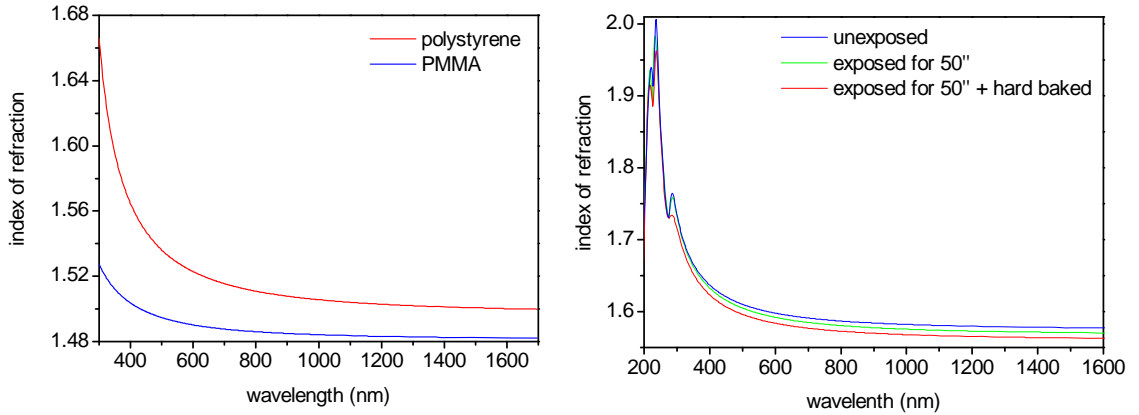


Figure 3.3.6: *Left:* The dispersion relationship for PMMA (260 nm) and polystyrene (800 nm). *Right:* The refractive index of the SU8 film following each fabrication step.

Another investigation involved the negative tone photoresist SU₈ [15]. In this experiment, the optical constants of SU8 were measured in order to identify the feasibility of volume hologram fabrication in SU8 [16]. For this type of fabrication, a thin SU8 film (~ 450 nm) is exposed to the interference pattern of the 325 nm line of a HeCd laser. Index changes can occur due to cross-linking during the post-exposure bake in the illuminated areas, creating thus a periodic structure. To identify the magnitude of the index modulation of this process, the refractive index of the polymer

was measured using ellipsometry. Three samples were measured, following each of the processing steps: the initial soft bake, immediately after UV exposure and after the post-exposure bake (figure 3.3.6). To ensure a uniform exposure over a large area, the films were flood exposed with a UV lamp. In figure 3.3.6, the respective results are illustrated. It can be observed that the exposure and subsequent baking steps lead to a reduction in refractive index across the spectral range. Overall, there is an index change of -0.014, which is comparable to other polymeric materials used for bulk holograms [17].

3.4 Optical design and characterisation

3.4.1 Design

The operation of microstructured polymer film lasers is based on the periodicity of the refractive index, with the feedback condition defined by the relationship between the wavelength of the laser beam and the optical period. Consequently, when the color of the emission, but also the direction of the output beam need to be specified or tuned, one must consider the period of the grating used and its relationship with the laser emission wavelength. In polymer microstructured films, lasing occurs when the following conditions are fulfilled [18]:

- a. The wavelength of the emitted photons satisfies the Bragg condition [19].
- b. The wavelength of the Bragg condition and the peak of the material gain coincide^{*}.
- c. The excitation density is adequate so that the gain exceeds the cavity losses.

^{*} The gain peak of the polymer medium corresponds to the wavelength, where Amplified Spontaneous Emission (ASE) occurs.

A simple way to determine the lasing wavelength in this type of structures is to neglect the periodicity of the refractive index profile. This is a valid approximation, since the width of the stop-bands in polymer microstructured films is in the order of a few nm, thus resulting in a similar accuracy. Despite the plethora of tools to directly solve the Maxwell's equations for periodic systems, this assumption features a rapid method to determine the lasing wavelength in a polymer diffractive laser.

The Bragg condition^{**} is satisfied when the half vacuum wavelength is an integer multiple of the optical period. The optical period in this case is the product of the effective refractive index (n_{eff}) of the relevant mode and the lattice constant:

$$m \cdot \frac{\lambda_i}{2} = n_{i,\text{eff}} \cdot \Lambda \quad (3.6)$$

A graphical illustration of condition (a) and relationship 3.6 is shown in figure 3.4.1, where the diffraction grating is a two-dimensional square lattice in this case and its Fourier representation is shown in green [20]. The sphere represents the equifrequency surface for a propagating mode within the waveguide (effective index n_{eff}) and thus with a radius of $r = k_0 n_{\text{eff}}$. The Bragg condition is satisfied at the intersection points between the lattice and the sphere. The position of the reciprocal lattice is not lying in the plane denoted by k_x and k_y , but is elevated at a height k_{z0} to account for the effective refractive index.

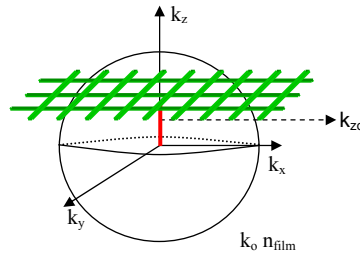


Figure 3.4.1: A schematic illustrating the fulfilment of the Bragg condition for a 2D square diffractive lattice.

^{**} Or the Laue condition in the context of wavevectors.

In this way, the identification of the lasing wavelength problem is reduced to determining the effective refractive index by solving the wave equation for an unperturbed* polymer waveguide. Having calculated the effective index of the fundamental transverse electric mode for the polymer, the subsequent step in the optical design of the polymer diffractive laser is relatively simple. For a given grating period, one has to determine the appropriate thickness that will satisfy the Bragg condition at the wavelength of the gain peak of the material. The frequencies of the propagating modes of a polymer waveguide are described by the eigenvalues of the wave equation corresponding to the respective boundary conditions. The solutions of interest are the bound modes, confined by the potential described by the index distribution. Other modes (leaky modes), will suffer from significantly decreased confinement and hence gain. In figure 3.4.2, the notation for the electric and magnetic fields of a slab polymer waveguide is illustrated. The wave equation can be solved by applying continuity conditions for both the magnetic and electric field at the polymer-substrate and polymer-air interface and solving numerically the following reduced mode equation** [21, 22]:

$$\frac{4 \cdot \pi \cdot d}{\lambda_0} \cdot \sqrt{n_g^2 - n_{\text{eff}}^2} = 2 \cdot \arctan \left[\sqrt{\frac{n_{\text{eff}}^2 - n_a^2}{n_g^2 - n_{\text{eff}}^2}} \right] - 2 \cdot \arctan \left[\sqrt{\frac{n_{\text{eff}}^2 - n_s^2}{n_g^2 - n_{\text{eff}}^2}} \right] - 2 \cdot M \cdot \pi \quad (3.7)$$

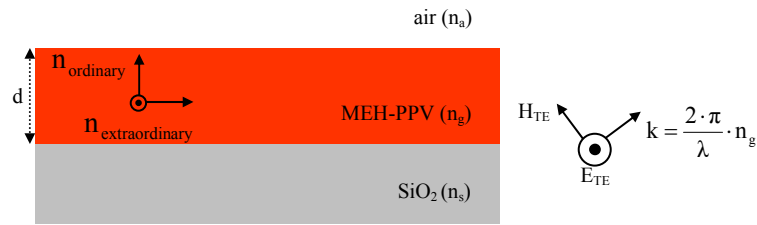


Figure 3.4.2: The cross – sectional view of a polymer waveguide, with the notation for the TE modes and the ordinary and extraordinary refractive indices.

Due to the birefringent nature of conjugated polymers, TE modes experience higher confinement factors for a certain polymer film thickness than the TM modes. From

* The ‘unperturbed waveguide’ denotes the absence of the refractive index modulation.

** This mode equation is valid for TE modes and the constants that enter the calculation are described in figure 3.4.2.

equation 3.7, it can be observed that for certain waveguide, superstrate and substrate indices, the effective refractive index of a waveguide mode will vary with the film thickness. For a MEH-PPV film, at $\lambda_0 = 630$ nm, the effective index dispersion of the fundamental TE mode is shown in figure 3.4.3. The values were calculated by solving equation 3.7. For comparison, the respective results from the CAMFR solver are also plotted in complete agreement [23]. It is worth mentioning that the polymer film thickness is a way to tune the laser emission by varying the film thickness and thus the effective refractive index.

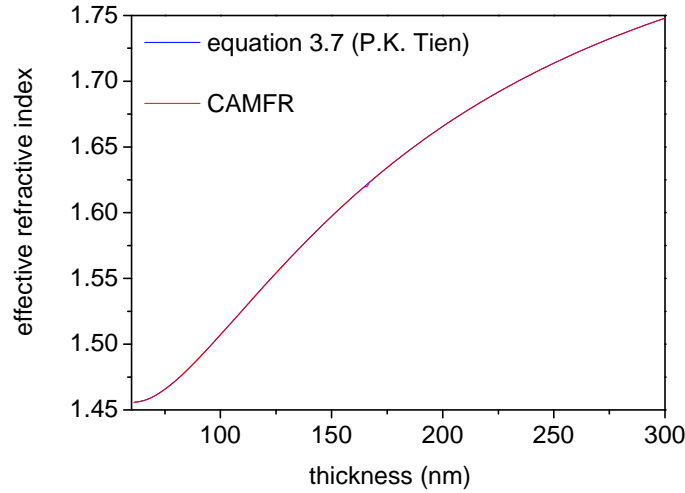


Figure 3.4.3: The effective index for a TE₀ mode in a MEH-PPV film as a function of the film thickness. The calculation was performed with two methods: equation 3.7 and the Maxwell's equation solver CAMFR.

For a more accurate analysis of the optical properties of polymer microstructures, one must take into consideration the periodic nature of the refractive index. In the case of an infinite structure, the function of the dielectric constant can be expanded into a Fourier series of plane waves that satisfy the periodic boundary condition, which is in essence the Laue condition. The expansion can be performed, either numerically or analytically depending on the geometry of the index interface within the primitive cell [24]. In addition, under the Bloch theorem, the electric and magnetic fields are periodic functions and can be also expanded in the same basis of plane waves. The wave equation in this case is a matrix eigenvalue problem and can be solved using numerical techniques. This method is the Plane Wave Expansion method (PWEM) [25-27].

For the purposes of this thesis, the PWEM was used in order to determine the dispersion relationships of 1-D and 2-D periodic polymer systems. The method that was followed is outlined in detail in reference [28]. The problems were reduced from three to two dimensions by assuming the transverse dimension infinite under the effective index approximation [29]. The number of plane waves was determined by studying the convergence of the eigenvalues at the wavevectors corresponding at the edges of the Brillouin zone. An indicative convergence calculation at the Γ and K points of the Brillouin zone of a square lattice is shown in figure 3.4.4. The calculation was performed for a square lattice, with an index contrast of $\Delta n = 0.2341$, corresponding to a 220 nm thick MEH-PPV film spun on a silica grating. The relevant band-structure is plotted in chapter 4 (figure 4.3.2). The convergence is approximately met for high enough number of plane waves (>2000). Higher accuracy can be achieved for an increased number of plane waves. However higher accuracy demands increased computation time as shown in figure 3.4.4 (right) *. Indicatively for a lattice constant of 268 nm by increasing the number of special frequencies from 2601 to 2809, the first eigenvalues at the Γ point differ in wavelength by $\Delta\lambda = 4 \cdot 10^{-5}$ nm. To this end, 2809 plane waves were considered adequate for this particular problem.

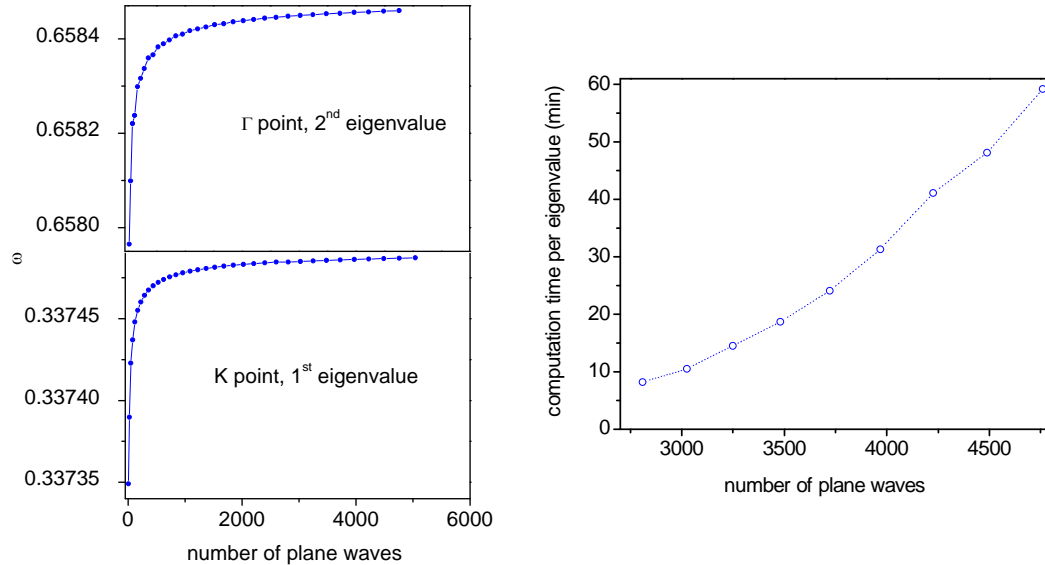


Figure 3.4.4: *Left:* The convergence plot for the different frequencies at the K and Γ points of the Brillouin zone. *Right:* the time needed to calculate a single eigenvalue as a function of the number of plane waves used.

* The measurements were based on a desktop computer.

3.4.2 Optical characterisation

The laser characterisation of polymer microstructures involves their excitation with a pulsed laser emitting at a wavelength that matches the absorption peak of the conjugated polymer. The energy of the pump light is thus efficiently transferred to the gain medium. The pump laser used throughout most of the thesis was a passively Q-switched Nd: YVO₄ that produces pulses of ~ 1 nsec duration (ALPHALAS PULSELAS-532-30-THG). Occasionally, a laser with longer pulse duration was used (7.5 nsec), especially in the context of the fibre experiments (LASER2000, LCSDTL374QT10). The emission of the polymer laser is coupled to a fibre and directed to a CCD spectrometer (Bruker Chromex 500 IS/SM, ANDOR DV420-OE). To avoid photooxidation, the polymer laser sample is held under vacuum at typically 10^{-5} mbar during operation.

The optical properties of diffractive nanostructures can be also characterised below threshold, where the direction of the spontaneous emission can be modified due to the resonant properties of the refractive index modulation. Experimentally this is achieved by performing angle dependent photoluminescence measurements, which essentially reveal information about the dispersion curve and scattering losses of a propagating mode in the periodic structure [30, 31]. The apparatus for such an experiment is shown in figure 3.4.5. The structure is illuminated by a CW laser beam and the spontaneous emission spectra are collected at different angles θ to the normal using a fibre coupled CCD spectrometer. The symmetries of the Brillouin zone are determined via the polarisation state of the scattered light by placing a thin Polaroid film is before the collection optics. The polariser is rotated at different angles Φ to select certain lattice planes.

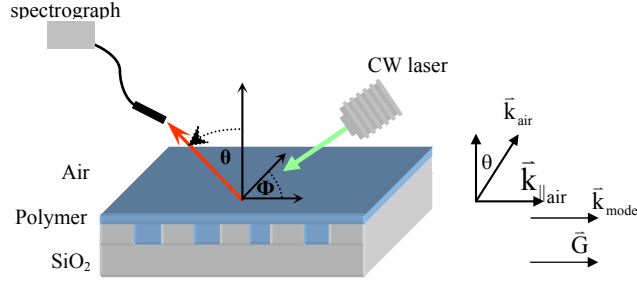


Figure 3.4.5: *Left:* The angle dependent photoluminescence apparatus. *Right:* A diagram illustrating the wavevectors involved in the phase matching condition.

In essence, the different wavelengths of the spontaneous emission couple to different waveguide modes propagating in the polymer with wavevector \mathbf{k}_{mode} . The phase matching condition in the plane of the film requires the conservation of momentum for a certain diffraction order (m) between the waveguide modes, the in-plane component of the radiation modes' wavevector ($\mathbf{k}_{\parallel\text{air}}$) and the grating vector (\mathbf{G}):

$$\bar{\mathbf{k}}_{\parallel\text{air}} = \bar{\mathbf{k}}_{\text{mode}} + m \cdot \bar{\mathbf{G}} \Rightarrow \frac{2\pi}{\lambda} \cdot \sin\theta = \pm \frac{2\pi}{\lambda} \cdot n_{\text{eff}} \pm m \cdot \frac{2\pi}{\Lambda} \quad (3.8)$$

Relationship 3.8 demonstrates how the angle of the scattered light can be linked to the in-plane wavevector for the different wavelengths of the spontaneous emission. The dispersion relationship above the light line can be mapped in this way by plotting the pairs of λ and θ .

A typical measurement for a 220 nm thick MEH-PPV film spun onto a square array diffractive grating with a lattice constant of $\alpha = 268$ nm is shown in figure 3.4.6. The square lattice is characterised by two lattice plane symmetries, the ΓM and the ΓK that are at an angle of $\Phi=45^\circ$ to each other^{*}. The collected spectra are plotted in 3.4.6 (*left*) both for a microstructured film with the polariser parallel to the ΓK at three diffraction angles (θ) and a planar film. The planar film exhibits a featureless spectrum, with a Lambertian angular intensity distribution (not shown). The spontaneous emission of the microstructured MEH-PPV film is different due to the wavelength dependence of

^{*} More information about the resonant properties of square diffractive lattices is given in section 4.3.1.

the phase matching condition. At each angle, waveguide modes of different wavelength are coupled out of the polymer following the band-structure at this particular wavevector window. Due to the difference in the lattice plane spacing at each symmetry of the Brillouin zone, the measured dispersion was different at each angle Φ (figure 3.4.6, right).

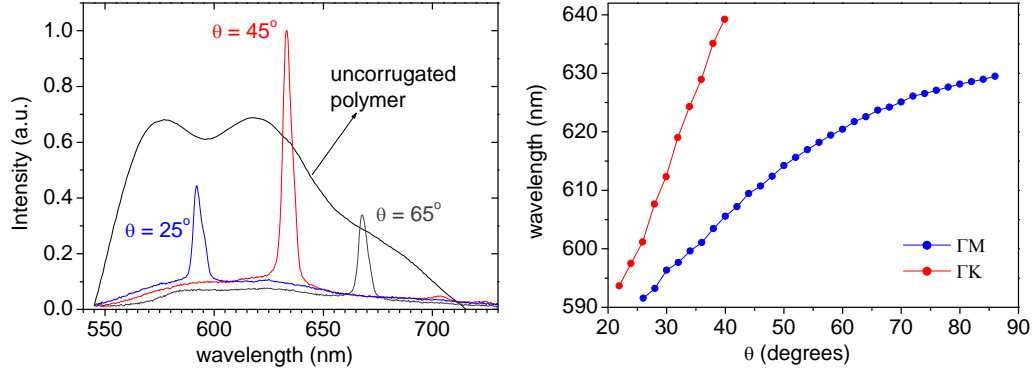


Figure 3.4.6: *Left:* A comparison between the spontaneous emission of a planar and a microstructured MEH-PPV film at different angles. *Right:* The dispersion relationship above the light line, measured at the two symmetries of the Brillouin zone of the square lattice.

Such measurements can reveal information about the propagation properties of the Bloch modes of the waveguide and hence can be of interest in the context of polymer lasers. In the previous example, the angle dependent photoluminescence measurement indicated the presence of a stop-band at the M point of the Brillouin zone (figure 3.4.6, right, blue). The stop-band manifested itself via the decrease of the rate of change of the energy of the mode (λ) with its wavevector (θ), which is essentially the group velocity of the propagating mode. The group velocity is constant at the Γ point of the Brillouin zone and hence no in-plane reflectivity is associated with this symmetry at this wavelength range (figure 3.4.6, right, red). The lasing characterisation of this microstructure confirmed the angle dependent photoluminescence characterisation, since the laser beam was primarily coupled out from the edge of the film ($\theta = 90^\circ$) at $\Phi = 45^\circ$ corresponding to the M point of the Brillouin zone.

3.5 Summary

The theme of this chapter was the fabrication and characterisation methodology of microstructured polymer lasers. The preparation method of these lasers involves the spin coating of the polymer gain medium on top of a periodic silica substrate. In terms of the substrate's corrugation, the technique that was specifically developed for the purposes of this thesis was based on the electron beam lithography. The detailed process is outlined in section 3.2, along with the challenges that were met during its development, namely the substrate's insulating properties, the adhesion and the proximity effects. These were addressed by employing a thin PEDOT and Au film as charge dissipation layers, by controlling the PMMA resist layer thickness and by performing proximity correction calculations respectively.

Over the past decades, ellipsometry has been developed as a non-invasive technique for accurate measurements of optical constants and thicknesses of thin films. This technique was proved useful in terms of studying different aspects of polymer lasers. The refractive indices of the conjugated polymers MEH-PPV and PFO were measured and their values were carefully incorporated into the design of polymer lasers. Several fabrication procedures were also examined using ellipsometry. The differential etch rates on a single sample due to 'edge effects' were determined. In addition, the feasibility of the fabrication of volume holograms in SU₈ films using a single-step exposure was also confirmed.

In section 3.4, the design rules for the operation of polymer lasers were outlined. Initially, a rapid and simple method to identify the laser wavelength was described, under the assumption that the periodicity of the refractive index does not perturb the waveguiding properties of the thin polymer films. The Plane Wave Expansion method is a more accurate technique for the aforementioned study and was also briefly described, mainly focusing on the aspect of the eigenvalue convergence and the required computational time. Finally, the characterisation techniques of polymer

microstructured films were analysed, both in the context of laser and waveguide dispersion characterisation.

These studies were critical in the context of optimising the operation characteristics of organic semiconductor lasers. The electron beam lithography provided the freedom to fabricate several types of feedback lattices for polymer lasers and mainly the 1st order gratings and Distributed Bragg Reflector lasers that are discussed in chapter 4 and 5 respectively. In addition, the PWE method provided the necessary insight to the radiation losses of gratings that are also outlined in chapter 4.

3.6 References

1. P. Rai - Choudhury, 'The SPIE handbook on Microlithography, Micromachining and Microfabrication', SPIE - International society for optical engineering (1997).
2. <http://www.gel.usherb.ca/Casino/index.html>, (freeware).
3. M.A. Mccord, 'Introduction to Electron-beam lithography', Short course notes on Microlithography, SPIE's International Symposium on Microlithography, 22 (1999).
4. J.W. Coburn, 'Plasma etching and reactive ion etching', SPIE's annual international symposium on Microlithography (2001).
5. M. Hatzakis, 'Electron resists for microcircuit and mask production', Journal of electrochemical society **116**, 1033 (1969).
6. M. Aggelopoulos, J.M. Shaw, K.-L. Lee, W.-S. Huang, M.-A. Annick, L. Tissier, M. Tissier, 'Lithographic applications of conducting polymers', Journal of vacuum science and technology **B9**, 3428 (1991).
7. F. Jonas, J.T. Morrison, '3,4- Polyethylenedioxythiophene (PEDT): conductive coatings technical applications and properties', Synthetic Metals **85**, 1397 (1997).
8. L.B. Groenendaal, F. Jonas, D. Freitag, H. Pielartzik, J.R. Reynolds, 'Poly(3,4-ethylenedioxythiophene) and its derivatives: past, present and future', Advanced Materials **12**, 481 (2000).
9. L. Stevens, R. Jonckheere, E. Froyen, S. Decoutere, D. Lanneer, 'Determination of Proximity Correction parameters using the doughnut method', Microelectronic Engineering **5**, 141 (1986).
10. A. Rampe, 'Lithography training course', Raith GmbH (2003).
11. I. J.A. Wollam Co., 'Application note: Genosc analysis of SiNx film', (2004).

12. O. Guadin, 'Private communication', (2005).
13. M. Tammer, A.P. Monkman, 'Measurement of the anisotropic refractive indices of spin cast films thin Poly(2-methoxy-5-(2'-ethyl-hexoly)-p-phenyl-enevinylene (MEH-PPV) films', *Advanced Materials* **14**, 210 (2002).
14. X.H. Wang, M. Grell, P.A. Lane, D. D. C. Bradley, 'Determination of the linear optical constants of poly[9.9-dioctylfluorene]', *Synthetic Metals* **119**, 535 (2001).
15. K.Y. Lee, N. LaBianca, S.A. Rishton, S. Zolgharnain, J.D. Gelorme, J. Shaw and T.H.P. Chang, 'Micromachining applications of a high resolution ultrathick photoresist', *Journal of vacuum science and technology* **13**, 3012 (1995).
16. F.M. Bain, A.E. Vasdekis, G.A. Turnbull, 'Holographic recording of sub-micron period photonic crystals in the photoresist SU8', *Proc. SPIE Int. Soc. Opt. Eng.* **5931**, 334 (2005).
17. W. J. Gambogi, A.M. Weber, T. J. Trout, 'Advances and applications of DuPont holographic photopolymers', *Holographic Imaging and Materials*, T. H. Jeong, ed., *Proc. SPIE* **2403**, 2 (1993).
18. C. Riechel, C. Kallinger, U. Lemmer, J. Feldmann, A. Gombert, V. Wittwer, U. Scherf, 'A nearly diffraction limited surface emitting conjugated polymer laser utilizing a two dimensional photonic band structure', *Applied Physics Letters* **77**, 2310 (2000).
19. C. Kittel, 'Introduction to Solid State Physics', John Wiley, New York **6th**, 36).
20. S. Wang, S. Sheem, 'Two-dimensional distributed-feedback lasers and their applications', *Applied Physics Letters* **22**, 460 (1973).
21. P.K. Tien, 'Integrated optics and new wave phenomena in optical waveguides', *Review of Modern Physics* **49**, 361 (1977).
22. A.B. Buckman, 'Guided Wave Photonics', Saunders College Publishing, 40).
23. P. Biestman, 'CAMFR 1.2', Ghent University (2003).
24. D.C. Champeney, 'Fourier transforms and their physical applications', Academic Press, London and New York, 8 (1973).
25. M. Plihal, A.A. Maradurin, 'Photonic band structure of two dimensional systems: The triangular lattice', *Physical Review B* **44**, 8565 (1991).
26. K. Sakoda, *Optical properties of photonic crystals*. Berlin: Springer-Verlag, (2001).
27. K.M. Leung, 'Plane-wave calculation of photonic band structure', *Photonic band gaps and localisation*, edited by C.M. Soukoulis, 269 (1993).
28. S. Guo, S. Albin, 'Simple plane wave expansion method for photonic crystal calculations', *Optics Express* **11**, 167 (2003).
29. M. Qiu, 'Effective index method for heterostructure-slab-waveguide-based two-dimensional photonic crystals', *Applied Physics Letters* **81**, 1163 (2002).
30. G. A. Turnbull, P. Andrew, W. L. Barnes, I. D. W. Samuel, 'Photonic mode dispersion of a two-dimensional distributed feedback polymer laser', *Physical Review B* **67**, 165107 (2003).

31. G. A. Turnbull, P. Andrew, M. J. Jory, W. L. Barnes, I. D. W. Samuel, 'Relationship between photonic band structure and emission characteristics of a polymer distributed feedback laser', *Physical Review B* **64**, 125122 (2001).

CHAPTER 4:

Distributed Feedback polymer lasers and radiation losses

4.1 Introduction

Nano-structured polymer films have been widely studied as a simple and effective method to realise DFB lasers. These laser structures show some of the lowest lasing thresholds for polymers, and so are of interest in the continuing quest for electrically pumped organic semiconductor lasers. In this chapter, the use of novel resonators based on the conjugated polymer poly(2-methoxy-5-(2'-ethylhexyloxy)-1,4- phenylene vinylene) (MEH-PPV) is presented that aim to optimise the laser performance by further reducing their threshold.

In polymer DFB lasers, the periodic modulation of the refractive index within the waveguide is responsible for the formation of a standing wave and thus feedback as described in section 2.4.2. However, there can be additional diffractive processes present that can add further functionalities to polymer DFB lasers, such as surface emission. Any light path that is not part of the feedback loop contributes to the radiation losses of the resonator, thus increasing the threshold.

The experimental evidence that the reduction of radiation losses greatly enhances the performance of polymer DFB lasers is the core of this chapter. This objective was primarily accomplished by directing the laser beam from the surface to the edge, by

employing 1st order diffractive feedback instead of the ‘traditional’ 2nd order one. This cancelled the radiation losses and as a result a substantial reduction of the threshold was observed as summarized in figure 4.1.1 for a DFB laser based on the conjugated polymer MEH-PPV. The exact details of these results will be outlined in the following sections.

Initially, in section 4.2 the origin and the generation mechanism of diffractive losses will be discussed using diffraction theory. Their effect on the operating characteristics of polymer lasers will be outlined using the plane wave expansion method for periodic photonic structures, allowing for a more pragmatic description of this type of losses. The experimental attempts to reduce these radiation losses and reduce the threshold of polymer lasers will cover the subsequent parts of this chapter. To this end, the initial attempts involved the employment of an alternative mirror symmetry of a square diffraction lattice. In section 4.3, this experiment is analysed starting with the analysis of the symmetries of a square lattice. The optical characterisation of the polymer laser will follow, where a reduction of the threshold by an order of magnitude was observed. In addition, the observation of dual mode operation, the characterisation of the beam divergence and the attempts to experimentally determine the Q-factor of the laser mode will be discussed.

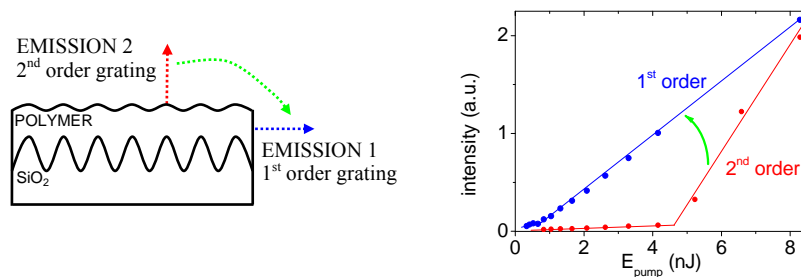


Figure 4.1.1: *Left:* A cross sectional view of a microstructured polymer laser. The two possible emission directions are depicted. *Right:* the reduction in threshold associated with the edge, or surface emission of 1st and 2nd order diffraction gratings respectively.

The beam quality improvement will be addressed in section 4.4. Edge-emitting polymer DFB lasers can suffer from a highly divergent output beam and thus the

benefit of surface emission becomes clear. This experimental study focused on how to re-direct the edge-emitted beam back to the surface by maintaining the low-threshold operation. This was achieved by integrating a surface-emitting output coupler in the proximity of an edge-emitting resonator. Different positions for the coupler were studied to achieve the optimal combination.

4.2 Radiation losses

The radiation loss is a type of ‘light leakage’ in wavelength-scale nanostructures and originates from the periodic nature of their dielectric constant. In polymer DFB cavities and under certain circumstances the laser field within the waveguide can couple to free space radiation due to the presence of the grating, limiting thus the net gain and increasing the threshold.

4.2.1 Diffractive processes in periodic structures

Coherent scattering in different directions is a manifestation of the diffractive nature of polymer nanostructured thin films. Each direction corresponds to a certain order of diffraction and occurs at an angle determined by the momentum conservation in the plane of the polymer film. Apart from the feedback, the other orders of diffraction contribute to the losses of the resonator. A way to envisage this plurality of diffraction orders within a single grating is the expansion of the dielectric constant into Fourier series: each Fourier coefficient corresponds to a different diffraction order [1]. Apart from its periodic nature, the relationship between the optical period* of the grating and the wavelength of the light involved is also important. This is frequently described as the *grating order*, which for a lattice constant α and wavelength λ_m is defined as:

* Optical period: the product of the actual period with the refractive index.

$$p = \frac{2 \cdot \alpha}{\lambda_m} \quad (4.1)$$

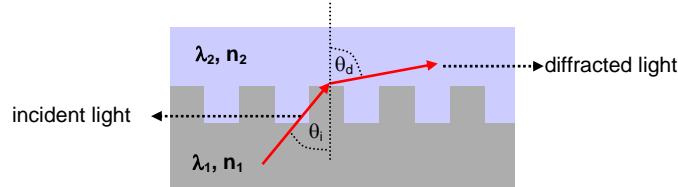


Figure 4.2.1: Diffraction from a grating embedded in a polymer waveguide

The grating order is correlated to the direction of the diffracted light. A simple method to investigate this effect is within the particle picture of photons (figure 4.2.1). In medium 1 (index n_1 and wavelength λ_1), the incident light is characterised by a wavevector \mathbf{k}_1 and respectively in medium 2 (n_2 , λ_2) the diffracted light by \mathbf{k}_2 . By applying the momentum conservation condition in the plane of the waveguide, one can obtain the following relationship, where G is the grating vector and m is the diffraction order:

$$\vec{k}_{//1} - m \cdot \vec{G} = \vec{k}_{//2} \quad (4.2)$$

Assuming that the light is propagating in the polymer waveguide at the critical angle and that the refractive index modulation is very weak ($n_1 \sim n_2$), a relationship between the diffraction angle, the order of diffraction m and the grating order p can be derived:

$$\sin(\theta_d) = 1 - \frac{2 \cdot m}{p} \quad (4.3)$$

Relationship 4.3 addresses the functionality of nanostructured polymer films. If a 1st order grating is employed ($p = 1$) then the 1st order diffraction process ($m = 1$) will essentially reflect the incident light in the opposite direction, since $\theta_d = -90^\circ$. This is

the origin of the feedback loop in polymer DFB lasers. In the case of a second order grating ($p = 2$), the same mechanism will be provided by a 2nd order diffraction process ($m = 2$), while the first order diffraction will be responsible for the surface coupling of the light traveling in the polymer waveguide ($\theta_d = 0^\circ$).

4.2.2 Radiation losses and laser operation

The transition from first to second order gratings has two major consequences. The first is the direction of emission, which for a 1st order grating can only be from the edge. In the case of a 2nd order grating, the laser emission can exit either from the edge, or from the surface (figure 4.1.1). The cancellation of the coupling to radiative modes in 1st order gratings also manifests itself in the operating characteristics. A 1st order grating suffers from significantly lower losses and thus its threshold is reduced in comparison to 2nd order gratings (figure 4.1.1).

The mechanism of coupling to free space radiation in polymer lasers can be also visualized in a dispersion diagram of a periodic nanostructure. Such a diagram provides a useful tool for rapid identification of whether a DFB laser -regardless of the dimensionality of its periodicity- for a certain grating period and wavelength will be surface emitting or not.

In figure 4.2.2, such a diagram is plotted for a thin MEH-PPV film (120 nm) spun on top of a linear silica grating (60 nm deep), which was calculated using a plane wave expansion method (PWEM) under the effective index approximation [2, 3]. In a defect free structure and due to an increased photon density of states, stimulated emission can primarily occur at the edges of the Brillouin zone (points A and B in figure 4.2.2). The conditions for feedback are also naturally met at other points of the dispersion curve

(formation of Floquet-Bloch modes), but the dispersion curve is not as flat indicating that the coupling strength is not as high resulting in higher end losses [4].*

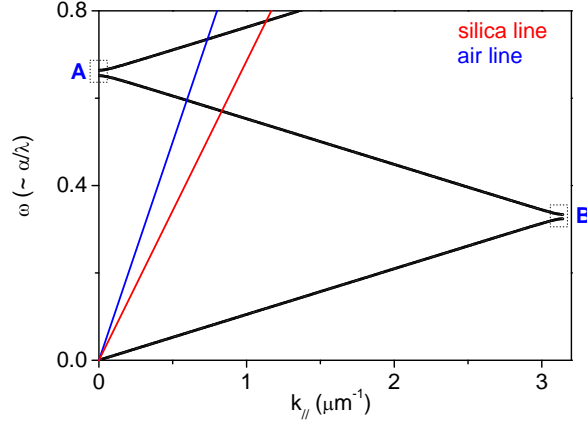


Figure 4.2.2: Dispersion of the fundamental TE mode of a thin film of MEH-PPV (120 nm) spun on a linear silica grating.

One of the differences between these points is their position with respect to the light cone, which is depicted in blue for the air-line ($\omega = \kappa$) and red for the substrate-line ($\omega = \kappa \cdot n_{\text{silica}}$). In essence, the light cone consists of photonic states that extend infinitely in the region outside the polymer waveguide. The modes with dispersion points above these lines are radiative modes, while purely guided modes can only exist below them [5].

The difference between radiative and non-radiative modes is illustrated in the transverse electric field distributions in figure 4.2.3 (the calculation was performed using CAMFR, section 3.4.1). For a laser operating at the A point of the dispersion diagram within the light cone, there are two main features to be noted. The first is the formation of a standing wave within the polymer waveguide and the second is the formation of plane wave normal to its plane. Surface emission is not present for a laser operating at the B point, where the Bloch mode is purely confined within the polymer.

* The end losses are losses in the plane of the waveguide due to reduced distributed reflection. Accordingly, the mode with higher end losses propagates further within the structure before it is reflected back.

In terms of performance, the laser operating at B is expected to have lower threshold due to the increased confinement of the laser mode within the polymer gain medium.

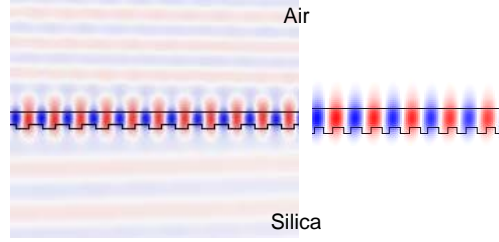


Figure 4.2.3: The transverse field distributions for points A (left) and B (right) points of the dispersion. Red denotes the positive values of the electric field, while blue the negative.

4.3 Low threshold edge emitting polymer DFB laser based on a square lattice

From the preceding analysis, it becomes obvious that an effective strategy to reduce the threshold of polymer lasers is to minimise the radiation losses and optimise the operating characteristics of polymer lasers. To this end, the selection of the correct grating order becomes critical. In the following, the case study of a square lattice is presented. This inherently comprises of two different grating orders and for a given wavelength it can operate either as a surface or an edge emitting polymer laser. Choosing the correct grating order resulted in a decrease of the threshold of approximately an order of magnitude.

4.3.1 The resonant symmetries of a square lattice

A square lattice diffraction grating comprises of ‘atoms’ with a higher or lower refractive index to the background arranged in a square formation. If the distance between the scatterers is α , then the elementary $\{\alpha_{//1}, \alpha_{//2}\}$ and reciprocal lattice vectors $\{b_{//1}, b_{//2}\}$ can be expressed as:

$$\begin{aligned}\bar{a}_{//1} &= \begin{pmatrix} \alpha \\ 0 \end{pmatrix}, \quad \bar{a}_{//2} = \begin{pmatrix} 0 \\ \alpha \end{pmatrix} \\ \bar{b}_{//1} &= \begin{pmatrix} 2\pi/a \\ 0 \end{pmatrix}, \quad \bar{b}_{//2} = \begin{pmatrix} 0 \\ 2\pi/a \end{pmatrix}\end{aligned}\tag{4.4}$$

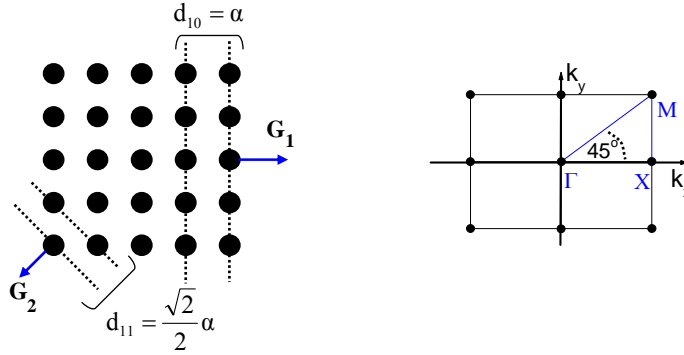


Figure 4.3.1: The real space representation of a 2D square lattice (left) and the respective Fourier space representation (right).

The real space representation and the first Brillouin zone of such a periodic structure is shown in figure 4.3.1. In real space, one can observe that the square lattice is comprised of two different mirror reflections under which the structure is invariant [6]. These symmetry directions are defined by the Miller indices (10) and (11) (figure 4.3.1) and are at an angle of 45° .^{*} Under the Bragg condition, each of these lines could provide feedback, but at a different wavelength since their interplane spacing is different, which for the aforementioned lattice constant are:

$$\begin{aligned}d_{10} &= \alpha \\ d_{11} &= \frac{\sqrt{2} \cdot \alpha}{2}\end{aligned}\tag{4.5}$$

In the corresponding Fourier space representation, the respective grating vectors are denoted as G_1 and G_2 (figure 4.3.1) and point along the two edges of the Brillouin zone ΓX and ΓM . The optical response of such a periodic structure can be studied using its band diagram. Such a diagram is plotted in figure 4.3.2 for a thin MEH-PPV film (200

^{*} The two mirror symmetries are also characterized by rotational symmetry at 90° , 180° and 270° .

nm), spun on a square silica grating, 60 nm deep with a hole radius of $0.3 \cdot \alpha$. In comparison to figure 4.2.2, the increased number of dispersion lines is indicative of the two dimensionality of the square lattice.

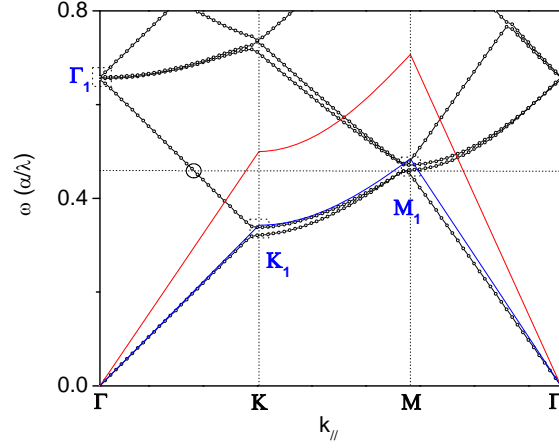


Figure 4.3.2: Dispersion of the fundamental TE mode of a thin film of MEH-PPV (220 nm) spun on a square lattice silica grating.

As already mentioned in section 4.2, the candidate modes for lasing are situated at the edges of the Brillouin zone Γ , K and M . The current literature of polymer lasers focuses mainly on the Γ point, where feedback is provided by the G_1 grating vector [7]. Resembling the fourfold rotational symmetry of the square lattice, there will be four modes coupled through the lattice vector. In addition, the Γ modes being inside the light cone will couple to free space radiation through a first order diffraction process, forming thus a vertical emitting polymer laser.

The following experiments were performed for a laser that operated at the M_1 dispersion point, which is situated below both the silica and air lines. The coupling to radiation modes is thus forbidden and the cavity losses are reduced significantly. The fourfold rotational symmetry again manifests itself via the presence of four dispersion points at this wavevector value, suggesting that four modes are coupled to form feedback through the grating vector G_2 .

The mirror symmetry at these two laser operating points of the Brillouin zone will manifest itself in the distribution of the electric field. These are plotted in figure 4.3.3 for the Γ_1 and M_1 points using the PWEM. It is clear that the fields at the M_1 and Γ_1 resemble the lattice vector direction and equivalently form 2-D standing waves with the resonant axes at an angle of 45° degrees to each other [8]. In addition, the position of the laser field antinodes with respect to the grating planes differs in each case indicating that a different order of diffraction is involved in the Bloch mode formation, as explained in more detail in section 2.4.2 (figure 2.4.4).

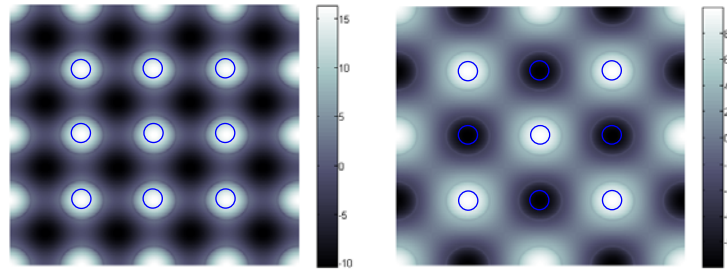


Figure 4.3.3: The electric field distributions of the lasing mode of the lower band at the Γ_1 (*left*) and M_1 (*right*). The grey scale to the right corresponds to the field values (white for positive and black for negative).

4.3.2 Low threshold operation

In the following experiment, the M_1 dispersion point was employed in order to reduce the radiation losses [9]. First order diffraction provided the feedback at a wavelength of 630 nm and the laser was configured as an edge-emitting one, resulting in a significantly reduced threshold in comparison to surface emitting lasers based on the same gain medium.

The substrate grating was a two-dimensional square lattice on SiO_2 and defined holographically resulting in a sinusoidal profile of the modulated interface (figure

4.3.4). It had a depth of approximately 60 nm and periodicity of $\alpha = 268$ nm (figure 4.3.1). For such a structure the grating pitch is either 268 nm, or 189 nm (4.5) and thus a laser can operate on the Γ_1 and M_1 points of the dispersion diagram respectively. For the latter and in the red part of the spectrum, the grating is first order and so will provide feedback via first order diffraction ($\theta_d = -90^\circ$).

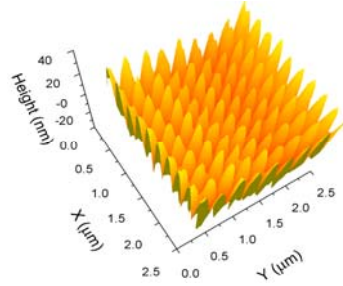


Figure 4.3.4: An atomic force microscopy image of a holographically defined square diffraction grating (image provided by G.A. Turnbull).

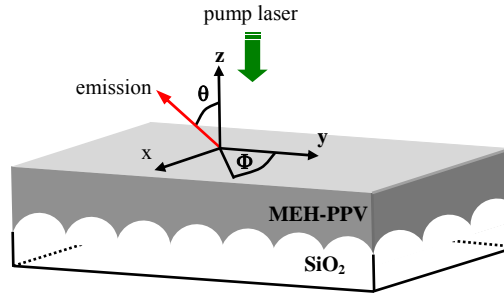


Figure 4.3.5: A cross-sectional view of a 2-D DFB polymer laser; the angles θ (polar angle to the z-axis) and Φ (azimuthal angle in the x-y plane) correspond to the direction of emission.

The optical gain medium was a thin film (200 nm thick) of the conjugated polymer MEH-PPV that was spin-coated on the grating. For this thickness, this asymmetric waveguide supported only the fundamental transverse electric mode in the spectral region of the polymer gain. Figure 4.3.5 shows a generic schematic of the device. The refractive index modulation is two-dimensional and the emission direction is defined by the polar angle to the z-axis (θ) and the azimuthal angle to the x-y plane (Φ). The

symmetries of the Brillouin zone are also defined by angle Φ : the ΓX at 0° and the ΓM at 45° .

The polymer laser was pumped optically using a frequency-doubled, passively Q-Switched Nd: YVO₄ microchip laser that produced 1 ns pulses at a wavelength of 532 nm, lying within the absorption peak of the MEH-PPV. The beam was focused to a uniform spot of approximately 50 μm diameter and the output of the polymer laser was measured using a fiber-coupled CCD spectrometer. In figure 4.3.6, the output spectra are shown for different pump intensities. These were measured parallel to ΓM symmetry direction ($\Phi = 45^\circ$), from the edge of the polymer film ($\theta = 90^\circ$). Two modes reached threshold in this device, at 630.8 nm and at 632.1 nm. The threshold for the longer wavelength mode was 0.66 nJ and for the shorter wavelength mode 1.2 nJ (figure 4.3.7). In comparison to previous surface emitting lasers, the threshold of this device was reduced: a value of 4 nJ was reported for a surface emitting polymer laser based on the same gain medium, where a 65% deeper square lattice grating was used with a period of 409 nm [7].

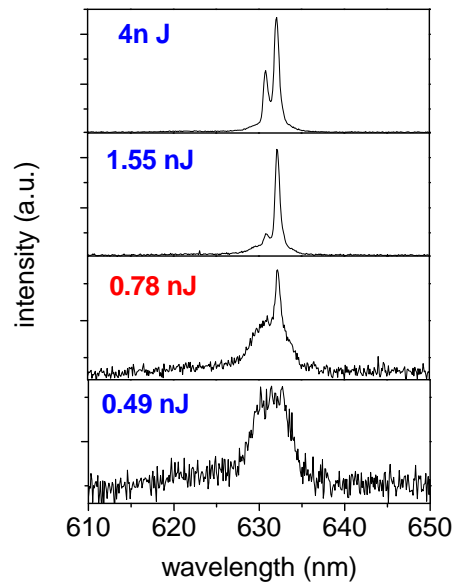


Figure 4.3.6: The edge emitted spectra for increasing excitation densities.

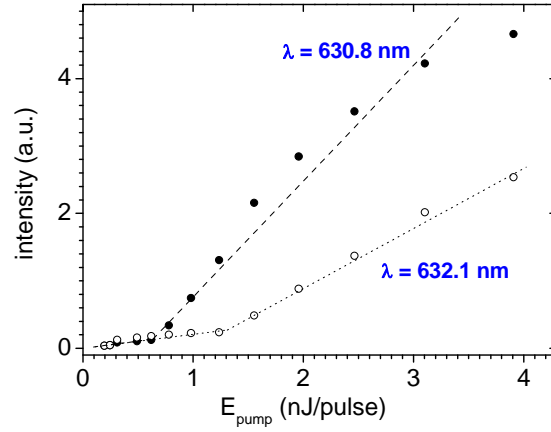


Figure 4.3.7: The output spectra of the polymer laser above and below threshold.

The factor that led to the lower threshold operation of the current device is the increased Q-factor of the resonant modes that is associated with the fulfilment of the Bragg condition below the light line [10]. Employing first order diffractive feedback and cancelling the emission normal to the surface reduced the radiation loss. The high quality factor of the band-edge modes at the M_1 operating point has been also reported by other groups and in the context of inorganic lasers, but this is the first report in organic lasers [11].

4.3.3 Dual mode operation

In the low threshold edge-emitting polymer laser, dual wavelength operation was observed. The two lasing modes were located at 630.8 nm and at 632.1 nm and their input-output relationship is shown in figure 4.3.7. The thresholds of these two modes were different, suggesting that there is a difference of amplification associated with them.

Previous reports on two wavelength operation of a square lattice polymer DFB laser, attributed this effect to an induced mismatch in the periodicity between the horizontal and vertical grating vectors [12].* However, the authors measured the thresholds of the two modes to be the same. This is expected because in essence the two-dimensional grating is comprised of two different resonators that suffer from the same losses and experience similar amplification. In addition, the supported Bloch modes by each grating will not be competing for gain being well spatially separated. The observation of the same threshold is distinctly different from my measurements.

Another type of asymmetry in the grating structure that could lead to dual wavelength operation would be an asymmetric unit cell. Such a laser has been previously demonstrated, where the holes of the photonic crystal were elliptical and not circular [13]. In this nanostructure, the fill factors are essentially different across the x and y axes, inducing a band-splitting at the operating point of the dispersion curve and thus the appearance of 1-D band-edge modes of a certain polarisation. This effect is also not expected to induce two modes of different thresholds.

A further hypothesis is the non-uniform excitation density of the cavity. Such an experiment has been previously performed, where an intentional defect in the pump size resulted in dual mode operation [14]. The pump size defect used was relatively large, covering ~15 % of the total contact area. In the edge-emitting polymer DFB laser however, a uniform excitation spot was consistently employed and thus the excitation asymmetry argument is not met as well.

The gain asymmetry manifesting itself via the different thresholds of the two modes can be attributed to the simultaneous lasing of two different band-edge modes at the M_1 operating point of the dispersion curve. Each mode can satisfy the Bragg condition for the same lattice constant ($\Lambda = 189$ nm), but for different effective refractive indices and thus different wavelengths:

* The lattice in this case was not a square one, but an orthogonal one since $\alpha_x \neq \alpha_y$.

$$\frac{\lambda_i}{2} = n_{i_{eff}} \cdot \Lambda \quad (4.6)$$

The difference in effective refractive indices can originate from the different localisation of each mode with respect to the grating planes [15]. Consequently, the formation of Bloch modes is permitted, but each mode samples a different region of the nanostructure. This is illustrated in figure 4.3.8, where the electric field distribution for the two Bloch modes is plotted using the plane wave expansion method.* The prominent difference is the field distribution of the two modes. The high wavelength mode (*left*) is localized more on the high index material (the holes in this case), while the low wavelength mode is localized in the low index medium. This induces the aforementioned difference in the effective refractive indices.

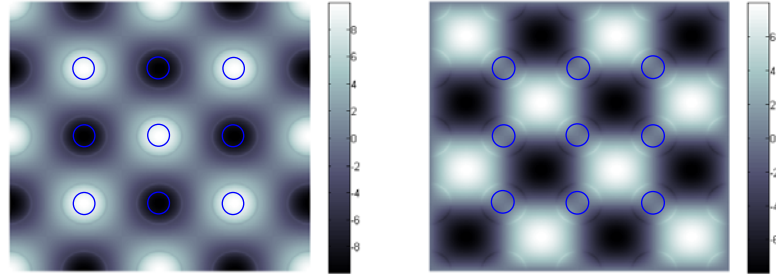


Figure 4.3.8: The electric field distribution for the two Bloch modes. The left one corresponds to the long wavelength laser mode and the right to the short wavelength one.

In this way, the threshold difference can be attributed to the difference in amplification that each mode experiences. The long wavelength mode will experience more gain than the low wavelength mode, which agrees with the experimental observation of the respective difference in their thresholds. The second interesting feature in figure 4.3.8 is that the two modes are spatially demultiplexed and thus they would not compete for gain. This competition would manifest itself via the dominance of one mode.

* The calculation was performed for a square lattice comprised of holes; this index profile is different to the sinusoidal experimental one but still useful in terms of visualising the effect, which is expected to be the same.

The observation of two-wavelength operation is different from other two-dimensional, vertical-emitting polymer DFB lasers. In such lasers, the two band-edge laser modes are formed inside the light cone and thus both suffer from significant radiation losses. However, each mode couples to free space with different coupling strength giving rise to a strong discrimination between the two band-edge modes [4]. The observation of two-mode oscillation shows that the mechanism of strong mode discrimination is not present when operating below the light line, where the radiation losses are significantly reduced.

4.3.4 Beam quality

The polymer film that covered the diffraction grating had a typical thickness of 200 nm. The vacuum wavelength of the light involved is approximately 3 times longer than the film thickness. Hence, in an edge-emitting configuration the beam divergence is expected to be quite high, an effect associated with a sub-wavelength aperture emission.

To this end, the angular dependence of the Γ M edge emitting polymer laser was measured. The laser was pumped 1.5 times above threshold (pump energy ~ 1 nJ) and the monochromatic emission was measured using a fibre-coupled CCD spectrometer at a distance of approximately 10 cm from the edge of the film. The experimental set-up was configured to allow the angular resolution of the intensity of the laser emission. The results are shown in figure 4.3.9 for a scanning direction parallel to the Γ M direction, essentially the resonator axis.

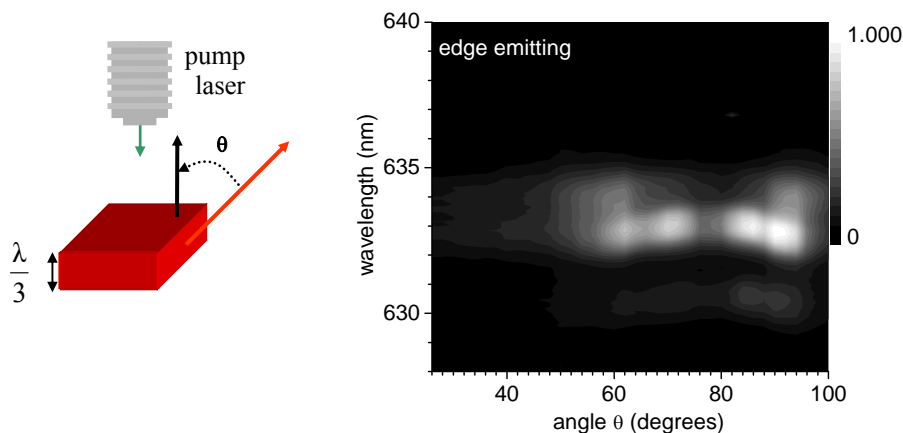


Figure 4.3.9: *Left:* the experimental set-up for measuring the divergence of the laser emission. *Right:* a contour plot showing the measurement of the emission spectra at different angles.

As expected, the laser emission was found to be most intense at an angle $\theta = 90^\circ$. However, two additional features can be also observed. The first one is the high divergence of the laser emission, which at a distance of 10 cm suffers from an angular dispersion of approximately $\Delta\theta = 40^\circ$. The second feature is the non-uniformity of the angular emission variation. This is attributed to the poor quality edges of the polymer laser that are not expected to be uniform for a spin-coated film. This non-uniformity is also expected to result from the process of cleaving such a structure. Polymers are not crystalline materials and thus cannot be cleaved. A result of such an attempt is shown in figure 4.3.10: a thin polymer film was spun on a SOI (silicon on insulator) substrate. Upon cleaving, the substrate forms very smooth interfaces, indicative of its crystallinity. On the contrary, the polymer being soft-matter forms a rather rough interface, mechanically deformed by the cleaving process.

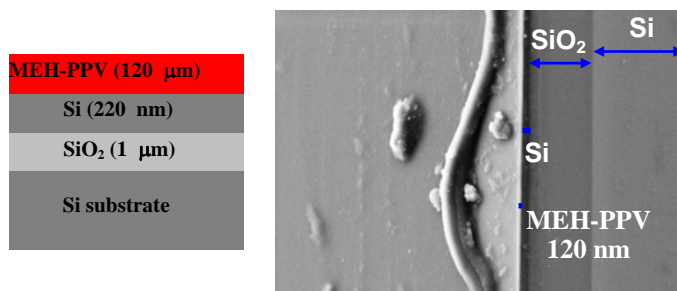


Figure 4.3.10: A SEM image of the edge of the structure shown to the left. The top layer is a thin MEH-PPV film that was spun on an SOI substrate.

4.3.5 The Q-factor of the resonator

The Q-factor of a resonator denotes the rate at which the stored energy is dissipated. In laser physics, this depends on the losses of the cavity and thus is highly correlated to the laser threshold. In this context, it can be expressed as a function of the resonant wavelength λ_o and the bandwidth of the resonant response $\Delta\lambda$ [16]:

$$Q = \frac{\lambda_o}{\Delta\lambda} \quad (4.6)$$

In the low threshold edge-emitting polymer laser, the measurement of the Q-factor would be advantageous in terms of a more direct comparison of the cavity losses with surface emitting lasers. Unfortunately, it was not possible to determine the Q-factor of the cavity mode in this experiment. The methods that were followed will, however, be discussed for sake of completeness.

Below threshold, the resonant mode cannot be seen in the spontaneous emission spectrum due to the low signal to noise ratio. Consequently, an alternative measurement in the time domain was attempted by measuring the decay time of the spontaneous emission. In essence, such an experiment would allow the determination of the Purcell factor, a direct measure of the modification of the spontaneous emission rate due to its coupling to a resonant mode [17]. This effect can be very significant in photonic crystal cavities [18-20]. For a mode of volume V , quality factor Q and wavelength λ , the Purcell factor is given by [17]:

$$f = \frac{3 \cdot Q \cdot \lambda^3}{4 \cdot \pi^2 \cdot V} \quad (4.7)$$

Two polymer samples were used. One was spun on a planar and one on the aforementioned corrugated fused silica substrate. By comparing the radiative lifetimes of these two samples at a single wavelength, one could determine the Purcell factor f

and indirectly the Q-factor of the resonant mode from equation 4.7. The samples were excited by femtosecond pulses (200 fsec) at high repetition rate (80 MHz). The emission was resolved by a streak camera and spectrometer simultaneously.

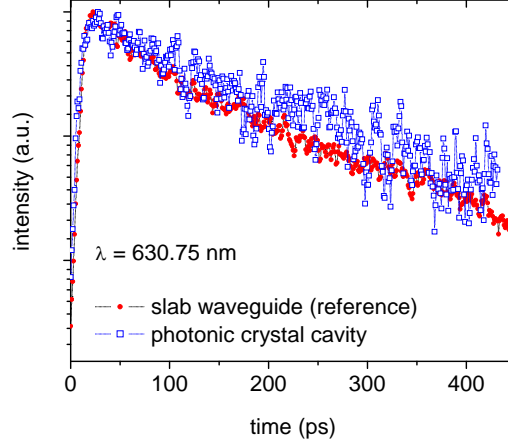


Figure 4.3.11: The decay rate of the spontaneous emission at a wavelength of 630 nm for the two samples. *Dr. M. Goossens contributed to these measurements.*

The results are shown in figure 4.3.11. No substantial difference can be observed between the two samples for multiple reasons [21]. First of all for a high enough Purcell factor, the optical modes must be well confined within the cavity. This did not occur in the photonic crystal structure due to the angular dependence of the reflectivity of the photonic crystal, but also due to the broad emission spectrum of the conjugated polymer. Secondly, an efficient energy transfer into the cavity modes must occur. To this end, the dipoles must be oriented perpendicular to the cavity axis, which is not perfectly met for spin coated polymer films. Thirdly, the measured value is the total photoluminescence decay time, while the Purcell effect is expected to affect only the radiative lifetime. Classically, the total decay rate is related to the quantum efficiency of the emitter and radiative and non-radiative decay rates via the relationships:

$$\Phi = \frac{\tau_{\text{rad}}^{-1}}{\tau_{\text{tot}}^{-1}}, \tau_{\text{tot}}^{-1} = \tau_{\text{rad}}^{-1} + \tau_{\text{non-rad}}^{-1} \quad (4.8)$$

Typically, for MEH-PPV $\Phi = 20\%$, $\tau_{\text{rad}}^{-1} = 1.2\text{ ns}$ and $\tau_{\text{non-rad}}^{-1} = 450\text{ ps}$ [22]. Consequently, for a Purcell factor of 0.1 the photoluminescence decay time would decrease by only 3 %, which would be within the experimental uncertainty. This is the reason why the first experiments in this field were performed in cryogenic temperatures where the non-radiative processes are reduced [23].

The aforementioned reasons prohibited an independent measurement of the Q-factor of the ΓM resonant symmetry in the time domain. However, the experimental measurement of the threshold reduction is adequate evidence and can be securely attributed to the effect of the increase of the Q-factor due to reduced radiation losses.

4.3.6 Summary

In summary, by employing a different symmetry of a square lattice the emission normal to the plane of the surface was cancelled, resulting in significantly reduced radiation losses. This in turn led to an optimised performance of polymer DFB lasers, where the threshold was reduced in comparison to surface emitting counterparts by a factor of 6. A weak output coupling of the laser field at $\theta = 35^\circ$ was also observed. This is due to the fulfillment of the phase matching condition for a mode propagating at $\Phi = 45^\circ$ being scattered by \mathbf{G}_1 (figure 4.3.5). This condition is clearly depicted in the band diagram of figure 4.3.2, where two longitudinal wavevectors correspond to the laser operating eigenfrequency; the one at the M_1 point and the other in-between the Γ and K points (circled in figure).

In addition, in contrast to previous reports two laser mode oscillation was observed. This was attributed to the absence of the discrimination due to the radiation losses that is the origin of single mode operation in surface-emitting polymer lasers. The edge-emitted beam was found to be highly divergent, an effect associated with the

subwavelength aperture emission from a thin polymer film. The experimental attempts to determine the Q-factor were also outlined.

4.4 Low threshold surface emitting polymer DFB laser: integration

From the preceding analysis, it becomes obvious that the surface emission has a negative effect on the laser operation by increasing its threshold. However, surface emission can have a great advantage in terms of low divergence beams since the emission aperture can be larger than the case of edge emitting polymer lasers. To this end, surface emitting polymer lasers suffer neither from non-uniform emission intensity variation, nor from high beam divergence. The beam quality has been found to have a M^2 value of 2.1, indicative of its high quality [7].*

For comparison, the angular dependence of the intensity of a surface-emitting laser is shown in figure 4.4.1. The laser was based on the blue emitting conjugated polymer PFO that was spun on the same substrate as the red edge-emitting laser. For a thickness of 250 nm, the laser operated at the Γ point of the dispersion diagram, where the feedback and output coupling is provided via second and first order diffraction respectively. The reason for using the same grating, but operating at a different wavelength, was to ensure that the grating quality is excluded from this comparative study.

It can be observed that the emission is centered at 0° to the normal. In comparison to the edge-emitting laser, the beam divergence at the same distance ($z = 10$ cm) is significantly lower, approximately 10 times smaller than the edge-emitting laser. This comparative study suggests that surface emission can act as a source of loss, but at the

* At a distance z from the source, the M^2 is defined through the relationship: $\omega = \omega_0 \cdot \sqrt{1 + \left(M^2 \cdot \lambda \cdot z / \pi \cdot \omega_0^2 \right)^2}$

same time it provides a useful means of out-coupling the laser radiation in a coherent manner.

In this section, a study will be discussed where the polymer laser was configured as a low threshold and surface emitting. This was performed in order to preserve the low beam divergence and angular uniformity, but also the requirement of low pump energies to reach threshold. Integrating an edge-emitting resonator with a surface output coupler allowed such a task to be achieved [24, 25].

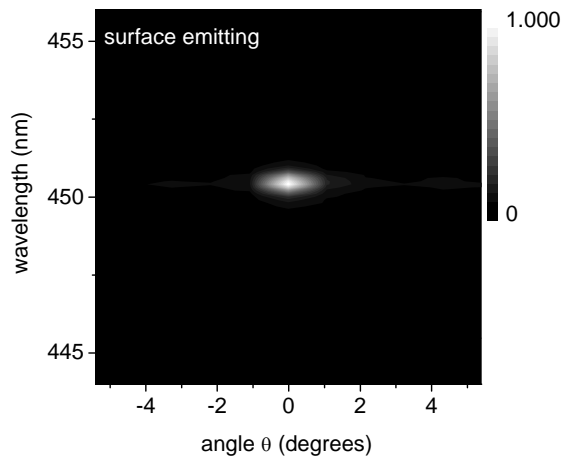


Figure 4.4.1: A surface plot of the measurement of the emission spectra at different angles.

4.4.2 Integration of an output coupler: low threshold and surface emission

The integration was employed to provide the functionality of surface emission, but also maintain the threshold at low levels. As already discussed, this is not possible in second order ($p = 2$) polymer lasers because the laser field experiences amplification, but extensive radiation losses simultaneously (figure 4.2.3/left). To this end, the regions of population inversion and output coupling must be separated and thus minimise the cavity losses. With this strategy, a low threshold, surface-emitting polymer DFB laser was realised.

Electron beam lithography allowed for such an experiment to be realised. With this technique, it was possible to perform the aforementioned integration, a challenge that cannot be met using more traditional lithographic techniques, such as optical holography. The substrate used was a 25x25 mm² fused silica wafer. This allowed for the definition of several structures on the same substrate, avoiding thus the non-uniformities of the polymer film thickness associated with small surface area substrates. In addition, several cavities of different parameters could be tested simultaneously in this manner under the same experimental conditions.

The cavity resonator was a linear 1st order grating ($p = 1$). In this, the grating vector is one-dimensional and consequently the laser field is also of the same dimensionality. The period of the grating was 205 nm and its fill factor 25 %. Feedback is provided by first order diffraction ($\theta_d = 90^\circ$) and no coherent radiation losses are expected to occur, since the phase matching condition for $\theta_d \neq 90^\circ$ cannot be met. Their total size was 80x80 μm^2 , forming thus a very compact resonator (figure 4.4.2).

At a distance of 20 μm from the cavity, an output coupler was defined. This was a linear 2nd order grating ($p = 2$) with a period of 410 nm and fill factor 21 %. This diffractive nanostructure can scatter the incident light normal to the surface ($\theta_d = 0^\circ$) providing the surface output coupling via 1st order diffraction. Additionally, second order diffraction provides in plane scattering ($\theta_d = 90^\circ$). To avoid the back-reflections into the cavity, the grating vector of the coupler was at an angle of 20° with respect to the cavity vector. In this way, the laser light was scattered from the coupler by second order diffraction escaping thus the system limiting the quantum efficiency (figure 4.4.2). The technique of an angled output coupler has been also employed in input-output coupling experiments where the amplification properties of thin polymer films have been measured [26].

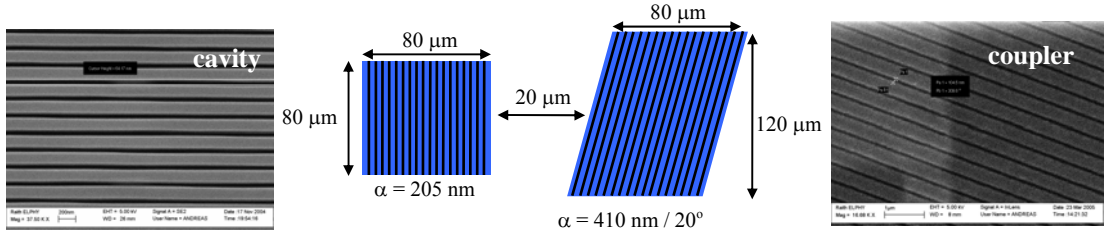


Figure 4.4.2: A top view of the integrated 1st order cavity with a 2nd order grating coupler. The SEM images of the respective gratings are also depicted.

The periods of the resonator and coupler gratings were matched, so that the laser light scatters at normal incidence from the surface. This matching included a factor of the integer 2 difference in their periods ($\alpha_{\text{coupler}} = 410 \text{ nm}$ and $\alpha_{\text{resonator}} = 205 \text{ nm}$ respectively) and the similarity in their fill factors. The latter is limited by the resolution of the available electron beam lithography system.

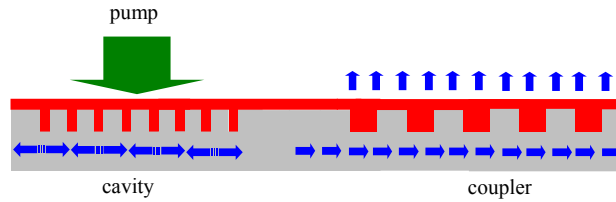


Figure 4.4.3: A cross sectional view of the integrated nanostructure, where the light path is also depicted.

To form a laser, a thin MEH-PPV film was spun on the substrate. The polymer used in this experiment is the same as in the experiments of the edge-emitting DFB laser to allow for a direct comparison. To this end, the pump laser source was also the same. The latter was focused to an excitation spot of $50 \mu\text{m}$ diameter on to the cavity resonator only. Thus, population inversion can only occur in this region. The generated light from the area of the cavity propagates then along the polymer waveguide and upon entering the coupler region, the distributed 1st order diffraction allows it to coherently scatter from the surface (figure 4.4.3). In the following experiment, the laser emission was collected from the surface.

Upon increasing the excitation density, a narrow peak appears at a wavelength of 634.55 nm denoting the onset of lasing (figure 4.4.4). The threshold pulse energy was low, at approximately 0.5 nJ. It was also found that lasing could be achieved when the excitation was focused on the output coupler that acts as a second order DFB polymer laser. The thresholds were significantly different due to the reduced radiation losses as discussed in section 4.3.

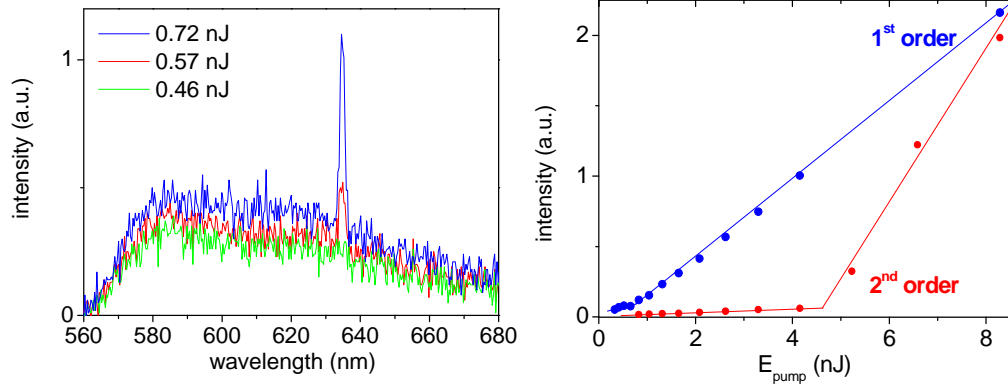


Figure 4.4.4: *Left:* the surface emitted spectra below and above threshold of the integrated polymer cavity when exciting the 1st order grating. *Right:* The input-output relationship of the 1st order laser. In comparison, the input-output curve of the 2nd order DFB resonator is plotted.

In comparison to the 2D edge-emitting polymer laser from the previous section, the threshold of the 1st order linear DFB laser was further reduced. This reduction is attributed to the complete cancellation of radiation losses and the improved quality of the grating. Several laser devices were tested of slightly different fill factors, ranging from 25 % to 35 % for the resonator (the fill factor of the coupler varied from 21 % to 25 % respectively). It was found that the effect of the fill factor is minimal in this case. The operating characteristics of polymer DFB lasers were further improved by integrating an output coupler within the proximity of the polymer resonator. Short and long period nanostructures operated as 1st and 2nd order gratings, allowing thus the low loss operation of the cavity, but also the advantageous surface emission from the structure.

4.4.3 Alternative position of the coupler

In the previous experiment, the output coupler was spatially separated from the cavity allowing thus the separation of the resonator with the source of radiation losses. An alternative strategy was also followed, namely the attempt to incorporate the coupler within the cavity [27]. To this end, the 1st order grating was divided into two sections and in-between a 2nd order grating was defined to allow for output coupling (areas A and B respectively in figure 4.4.5).

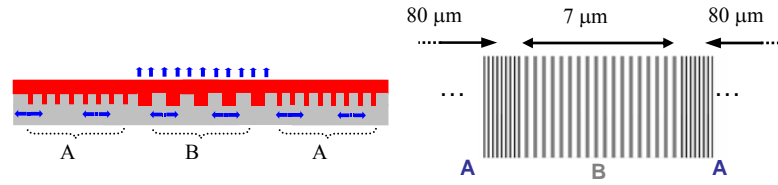


Figure 4.4.5: A cross sectional (*left*) and top view (*right*) of the hybrid, dual period polymer resonator.

In essence, this resonator is a hybrid one comprising of two components that can provide the functionality of feedback and surface emission separately. This structure provides additionally the control of the radiation losses through the length of region B. The excitation spot was focused across the whole structure, providing gain in both A and B areas. The generated spontaneous emission experiences both amplification and the distributed reflections of area A, building thus the laser field. Area B also scatters out from the surface from the central region, forming a surface-emitting laser.

The structures were fabricated using electron beam lithography and an SEM image of a typical structure is shown in figure 4.4.6. The size and period of each 1st order grating is $80 \times 80 \mu\text{m}^2$ and $\alpha = 200 \text{ nm}$ respectively, while these values for the 2nd order one are $7 \times 80 \mu\text{m}^2$ and $\alpha = 400 \text{ nm}$ (4.4.6/right). In terms of the fill factor, this was chosen to allow similar etching conditions for both components of the structure [28]. The etching depth of the exposed areas of the unit cell is dependent on its width and similar widths result in similar etch depths. In this experiment, this occurred for the optimal experimental fill factors of 40 % for the grating A and 22 % for grating B.

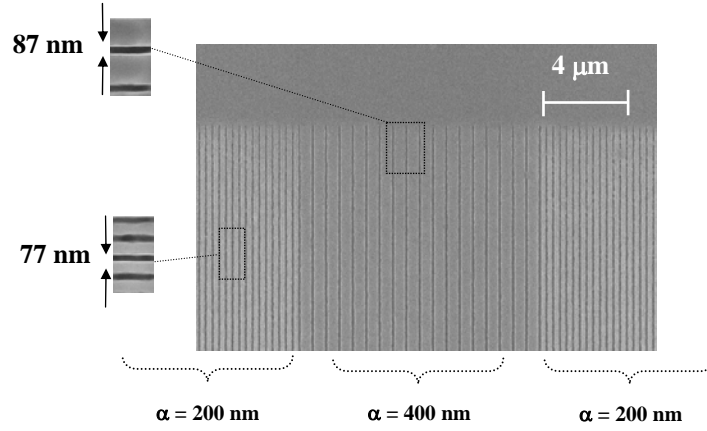


Figure 4.4.6: An SEM image a respective dual period hybrid structure.

The conjugated polymer used for amplification in this experiment was again a thin MEH-PPV film. In the optical characterisation, a circular excitation spot of 75 μ m radius was chosen to illuminate the hybrid structure. Upon increasing the excitation density, two laser modes appear. A probable cause for this effect is the difference in the resonant properties of the two components of the cavity. Such a potential difference would lead to dual wavelength operation.

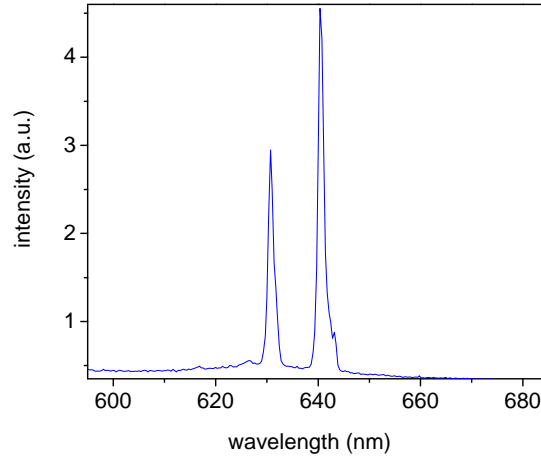


Figure 4.4.7: The surface emitted spectra of the hybrid structure above threshold.

To identify the origin of the two modes, a surface scan measurement was performed.

In the surface scan measurement, the sample is translated across the excitation spot, the position and pulse energy of which are kept constant (figure 4.4.8). In this way, each component of the cavity is excited above threshold and its resonant properties can be identified in the far field through the surface coupled stimulated emission.

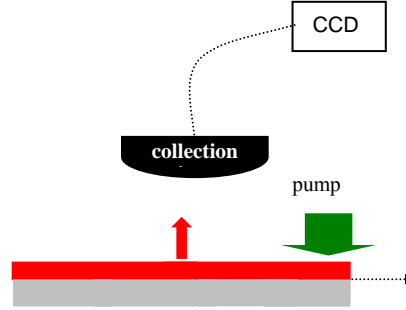


Figure 4.4.8: The experimental configuration of the surface scan measurements, including the translated sample, the excitation spot and the surface response measurement.

In figure 4.4.9 (*left*), a typical surface scan measurement is shown. The graph is a contour plot, displaying information about the spectral response for each position of the excitation on the sample, but also the respective intensities. It can be observed that two different modes reach threshold, at wavelengths of $\lambda_1 = 630$ nm and $\lambda_2 = 640$ nm. The transition from the one to the other occurs at an x-axis value of $50\text{ }\mu\text{m}$. The symmetry of the surface response resembles the structural symmetry of the hybrid resonator. The selective excitation of the A and B components of the cavity results into stimulated emission at the two different wavelengths λ_1 and λ_2 respectively. This finding suggests that each grating operates as a separate cavity, hindering thus the single frequency operation when the whole structure is illuminated. For comparison, the same measurement was performed in the cavity outlined in section 4.4.4. The excitation spot in this experiment was of $25\text{ }\mu\text{m}$ radius. The surface response of the resonator differed as well depending on whether the 1st (A) or the 2nd (B) order grating was illuminated (figure 4.4.9/*right*). However, it is relatively simpler to achieve single frequency operation in this structure by exciting the 1st order grating only.

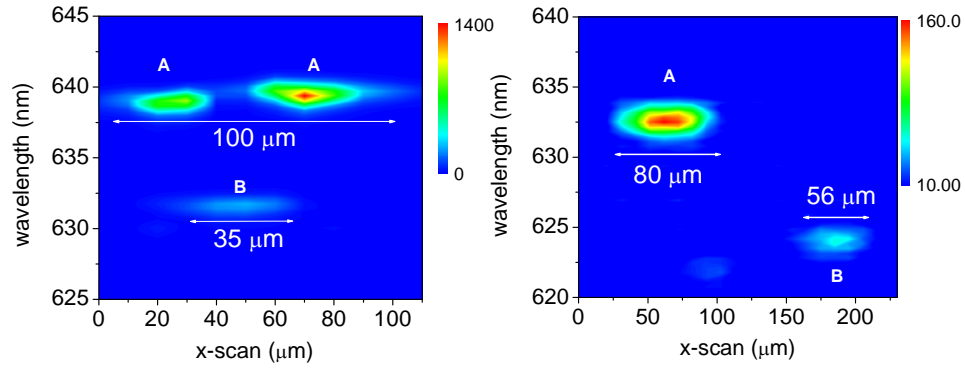


Figure 4.4.9: A surface scan plot of the surface emission of the hybrid dual-period polymer laser (*left*) and of the integrated cavity and coupler structure of section 4.4.4 (*right*).

In the hybrid structure, the requirements of single mode operation and simple alignment would both be met if the fill factors of the two gratings completely matched. In this case, the reflectivity spectra of the 1st and 2nd order gratings would display the center of the stop-band at the same wavelength, providing the same response. Such a task would require however a high degree of fabrication accuracy and in addition the differential etch rate would need to be considered. In addition, it would be more demanding to obtain the same response function from gratings fabricated by solvent assisted micro-molding, hindering thus this attractive option of mass production. On the contrary, the integrated laser and coupler case can achieve both with a simpler preparation and less demanding cavity design, offering thus a more attractive option for a low-threshold, surface-emitting polymer laser.

4.5 Conclusions

The emission direction of a polymer nanostructured laser plays a significant role in its performance. Edge-emitting polymer lasers can exhibit low thresholds, an essential optimization towards electrical excitation. In this chapter, the effect of surface emission was studied. It was confirmed that by ‘steering’ the output beam from the surface to the edge, the threshold of polymer DFB lasers was significantly reduced.

To achieve this ‘steering’, a novel symmetry of a square lattice was initially employed. The grating in this case acted as a 1st order one and thus the laser field was confined only in the polymer waveguide structure and did not couple to radiative modes. The operation below the light line reduced the round trip losses of the photonic crystal cavity, allowing a significant reduction in the threshold in comparison to previous surface-emitting polymer lasers. In the square lattice laser, dual mode operation was observed, the condition of which was the reduced radiation losses: in contrast to surface emitting lasers, the loss discrimination between the two band-edge modes was not present in this laser. The measurement of the angular variation of the edge emitted output beam identified the considerable beam divergence associated with the edge-emission of thin films.

To overcome the divergence of the output beam, surface coupling was revisited. It is known that surface-emitting polymer DFB laser exhibit good beam quality and to this end a low threshold surface-emitting laser was targeted. This was achieved by integrating an edge-emitting resonator with an output coupler that scatters the laser light from the surface. These two components were spatially separated and consequently the amplification region did not suffer from radiation losses. The threshold of this laser was further reduced in comparison to the square lattice edge-emitting laser due to the complete cancellation of the radiation losses. An alternative architecture to achieve both surface emission and low threshold was also studied, where the output coupler was defined in the centre of the edge-emitting resonator. It was found that the lithography resolution in such a nanostructure becomes very critical in terms of single frequency operation. Dual mode operation was observed as each area of the hybrid nanostructure lased independently. Surface scan measurements were performed to confirm the different resonant properties of the coupler and the cavity. These revealed that the integration of the output coupler in the proximity of the cavity is advantageous in terms of single mode operation.

4.6 References

1. A. Yariv, P. Yeh, *Optical waves in crystals*, Wiley, New Jersey (2003).
2. S. Guo, S. Albin, 'Simple plane wave expansion method for photonic crystal calculations', *Optics Express* **11**, 167 (2003).
3. M. Qiu, 'Effective index method for heterostructure-slab-waveguide-based two-dimensional photonic crystals', *Applied Physics Letters* **81**, 1163 (2002).
4. R. Kazarinov, C.H. Henry, 'Second order distributed feedback lasers with mode selection provided by first order radiation losses', *IEEE Journal of Quantum Electronics* **21**, 144 (1985).
5. S.G. Johnson, S. Fan, R. Villeneuve, J.D. Joannopoulos, 'Guided modes in photonic crystals', *Physical Review B* **60**, 5751 (1999).
6. H.D. Megaw, 'Crystal structures: a working approach', *Studies in Physics and Chemistry*, Saunders College 10 (1973).
7. G.A. Turnbull, P. Andrew, W.L. Barnes, I.D.W. Samuel, 'Operating characteristics of a semiconducting polymer laser pumped by a microchip laser', *Applied Physics Letters* **82**, 313 (2003).
8. R. Harbers, N. Moll, R.F. Mahrt, D. Enri, W. Batchold, 'Enhancement of mode coupling in photonic-crystal-based organic lasers', *Journal of Optics A: Pure Applied Optics* **7**, S230 (2005).
9. A.E. Vasdekis, G.A. Turnbull, I.D.W. Samuel, P. Andrew, W.L. Barnes, 'Low threshold edge emitting polymer distributed feedback laser based on a square lattice', *Applied Physics Letters* **86**, 161102 (2005).
10. Y. Akahane, T. Asano, B-S. Song, S. Noda, 'High-Q photonic nanocavity in a two-dimensional photonic crystal', *Nature* **425**, 944 (2003).
11. S.-H. Kwon, H.-Y. Ryu, G.-H. Kim, Y.-H. Lee, 'Photonic bandedge lasers in two-dimensional square-lattice photonic crystal slabs', *Applied Physics Letters* **83**, 3870 (2003).
12. J. Stehr, J. Crewett, F. Schindler, R. Sperling, G. Plessen, U. Lemmer, J.M. Lupton, T.A. Klar, J. Feldmann, A.W. Holleitner, M. Forster, U. Scherf, 'A low threshold polymer laser based on metallic nanoparticle grating', *Advanced Materials* **15**, 1726 (2003).
13. S. Noda, M. Yokoyama, M. Imada, A. Chutinan, M. Mochizuki, 'Polarisation mode control of two-dimensional photonic crystal laser by unit cell structure design', *Science* **293**, 1123 (2001).
14. M. Imada, S. Noda, A. Chutinan, T. Tokuda, M. Murata, G. Sasaki, 'Coherent two-dimensional lasing action in surface-emitting laser with triangular-lattice photonic crystal structure', *Applied Physics Letters* **75**, 316 (1999).
15. H. Benisty, D. Labilloy, C. Weisbuch, C. J. M. Smith, T. F. Krauss, D. Cassagne, A. Beraud, C. Jouanin, 'Radiation losses of waveguide-based two-dimensional photonic crystals: Positive role of the substrate', *Applied Physics Letters* **76**, 532 (2002).
16. O. Svelto, *Principles of laser physics*, Plenum Press (1997).
17. E.M. Purcell, 'Spontaneous emission probabilities at radio frequencies', *Physical Review* **69**, 681 (1946).

18. A. Badolato, K. Hennessy, M. Atature, J. Dreiser, E. Hu, P.M. Petroff, A. Imamoglu, 'Deterministic Coupling of Single Quantum Dots to Single Nanocavity Modes', *Science* **308**, 1158 (2006).
19. M. Fujita, S. Takahashi, Y. Tanaka, T. Asano, S. Noda, 'Simultaneous inhibition and redistribution of spontaneous light emission in photonic crystals', *Science* **308**, 1296 (2005).
20. P. Lodahl, A. F. Driel, I. S. Nikolaev, A. Irman, K. Overgaag, D.L. Vanmaekelbergh, W.L. Vos, 'Controlling the dynamics of spontaneous emission from quantum dots by photonic crystals', *Nature* **430**, 654 (2004).
21. G. R. Hayes, F. Cacialli, R.T. Phillips, 'Ultrafast study of spontaneous emission from conjugated polymer microcavities', *Physical Review B* **56**, 4798 (1997).
22. N. T. Harrison, G. R. Hayes, R. T. Phillips, R.H. Friend, 'Singlet Intrachain Exciton Generation and Decay in Poly(p-phenylenevinylene)', *Physical Review Letters* **77**, 1881 (1996).
23. U. Lemmer, R. Hennig, W. Guss, A. Ochse, J. Pommerehne, R. Sander, A. Greiner, R. F. Mahrt, H. Bassler, J. Feldmann, E.O. Gobel, 'Microcavity effects in a spin-coated polymer two-layer system', *Applied Physics Letters* **66**, 1301 (1995).
24. H. Rigneault, F. Lemarchand, A. Sentenac, H. Giovannini, 'Extraction of light from sources located inside waveguide grating structures', *Optics Letters* **24**, 148 (1999).
25. A. Mekis, A. Dodabalapur, R.F. Slusher, J.D. Joannopoulos, 'Two-dimensional photonic crystal output couplers for unidirectional light output', *Optics Letters* **25**, 942 (2000).
26. V. C. D. Amarasinghe, A. Ruseckas, A. E. Vasdekis, M. Goosens, G. A. Turnbull, I.D.W. Samuel, 'Organic Optical Amplifier Based on the conjugated polymer MEH-PPV', *Applied Physics Letters* **89**, 201119 (2006).
27. C. Karnutsch, C. Gyrtner, V. Haug, U. Lemmer, T. Farrell, B.S. Nehls, U. Scherf, J. Wang, T. Weimann, G. Heliotis, C. Pflumm, J.C. Demello, D.D.C. Bradley, 'Low threshold blue conjugated polymer lasers with first- and second-order distributed feedback', *Applied Physics Letters* **89**, 201108 (2006).
28. Y. H. Lee, Z.H. Zhou, 'Feature-Size Dependence of Etch Rate in Reactive Ion Etching', *Journal of Electrochemical Society* **138**, 2439 (1991).

CHAPTER 5:

Distributed Bragg Reflector polymer lasers and applications

5.1 Introduction

Organic semiconductor lasers based on Distributed Bragg Reflector resonators (DBR) were some of the initial resonators to be investigated during the early attempts to demonstrate and optimise laser action from organic solid state media [1, 2]. As discussed in chapter 2, in these lasers the organic amplifier is placed between two reflective mirrors that provide a wavelength dependent reflectivity and can thus be utilised in the context of laser mode selection and single mode operation.

DBR lasers exhibit certain structural and more importantly operational similarities to the well-documented and extensively characterised microcavity polymer lasers [3-6]; however, the operation principle of microcavities is significantly simpler. To this end, I fabricated and characterised a polymer microcavity laser and its operation will be discussed first in section 5.2. The fabrication, characterisation and detailed analysis of polymer DBR lasers will follow in section 5.3 and the differences between DBR lasers and microcavities will be discussed to illustrate the advantages of the former. A comparative analysis with surface-emitting DFB lasers will be also discussed in the same section, outlining both the experiments and the effects observed.

In section 5.4, a major result of my thesis is described, namely the demonstration of diode pumped polymer lasers. This experiment lead to a new operational regime of solid-state polymer lasers, where the traditional excitation source – the frequency

doubled microchip laser – is replaced with the more compact and thus more practical inorganic GaN semiconductor diode laser. The demonstration of a silicon based polymer laser is outlined in section 5.5. This type of device was based on a novel DBR resonator design on a silicon-on-insulator chip. It combines the well-established silicon processing and the solution processing of organic semiconductors and could provide an alternative route to cost-effective silicon based optical interconnects. The performance of silicon based lasers was analysed under optical excitation conditions and compared to the all silica DBR polymer lasers. G. Tsiminis and J.-C. Ribierre contributed to the diode experiments and S. Moore to the silicon based polymer lasers.

5.2 Microcavity lasers

The microcavity laser consists of a thin polymer film placed between two highly reflective mirrors. The mirrors were purchased from a commercial source* and consisted of a multilayer coating on fused silica cylindrical substrates. They were designed to exhibit high reflectivity in the wavelength region of 615 nm - 640 nm (figure 5.2.1, *left*) that matches the gain spectrum of MEH-PPV.

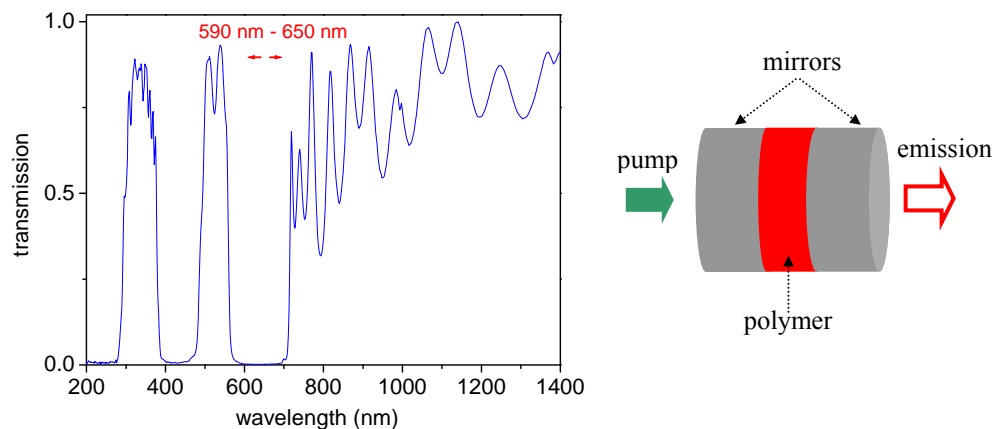


Figure 5.2.1: *Left:* The transmission spectrum of a single mirror. *Right:* A general schematic illustrating the structure of a microcavity polymer laser.

* LaserOptik, A050519.

The microcavity structure is shown in figure 5.2.1 (*right*). The polymer was spin coated from a 5.85 mg/ml chlorobenzene solution on both mirrors at a spin-speed of 1200 rpm, giving a thickness of approximately 120 nm. The cavity was made by manually pressing the two polymer films together in nitrogen atmosphere at 60°C. During this process, care was taken in order not to slide the two surfaces with respect to each other, which could induce a thickness variation across the polymer film [5, 6]. In order to optically excite the microcavity polymer lasers, the 532 nm line from the microchip laser was focused to a spot of 200 μm in diameter, while spontaneous emission measurements were performed using a continuous wave laser at the same wavelength. For both cases, the excitation and detection configuration was the same and shown in figure 5.2.1.

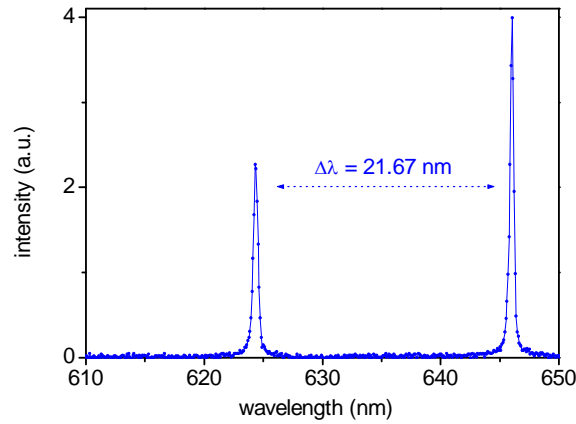


Figure 5.2.2: The spontaneous emission spectrum when the microcavity is pumped with a CW source.

The spontaneous emission spectrum from the polymer microcavity is shown in figure 5.2.2. Two longitudinal modes appear at wavelengths of 624.4 and 645.8 nm, with a mode spacing of approximately 26 nm. The reason for the dual mode operation lies in the cavity length, which is long enough for the resonant condition to be satisfied at the two wavelengths. From the mode spacing, the effective cavity optical length can be deduced and found to be approximately 7 μm . This value corresponds to sum of the optical thickness of the polymer film and the penetration depth at each mirror. The Q-factors of the short and long wavelength mode were measured to be 1562 and 1612 respectively. This difference is small and can be explained by the slightly higher

reabsorption losses at the shorter wavelength, or a small change in the transmission losses.

The angular dispersion of the resonant modes was measured by collecting the spontaneous emission spectra at different angles with respect to the normal to the film plane. The measurements are shown in the contour plot of figure 5.2.3, where it can be observed that the wavelength of the resonant modes remains constant in the range of $\pm 4^\circ$, indicating that the resonant condition is not angle dependent close to normal incidence. Such an effect is expected because the reflectivity spectrum of the mirrors does not vary significantly with the angle of incidence in this angular range.

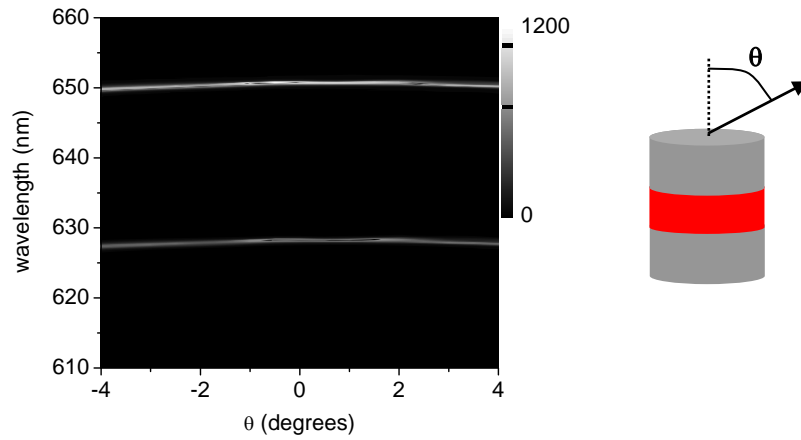


Figure 5.2.3: The angle-dependent photoluminescence measurement for the polymer microcavity, pumped with the CW source.

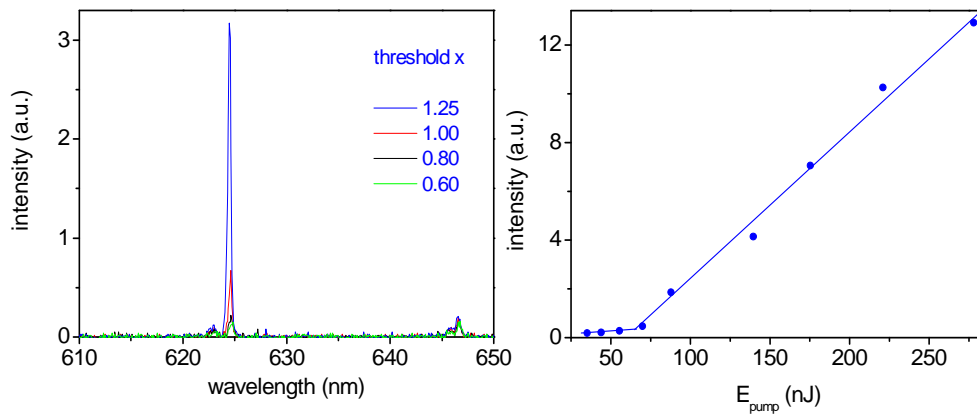


Figure 5.2.4: *Left:* The emission spectra for different excitation densities, below and above threshold. *Right:* The input-output relationship for the polymer microcavity

When the polymer microcavity is excited with the pulsed microchip laser, the emitted spectra resemble the ones obtained with the CW source. Above a certain excitation density, the resonant mode at 624.4 nm increases faster in intensity in comparison to the longer wavelength mode that remains ‘pinned’ at the same intensity value (figure 5.2.4, left). This sharp increase in the emitted intensity is clear evidence of the onset of lasing from the polymer microcavity (figure 5.2.4, right). The origin of the selectivity between the two wavelength modes above threshold is attributed to the lower gain of the conjugated polymer at the wavelength of the second resonant mode.

In terms of its operating characteristics, the polymer microcavity laser exhibits a higher threshold energy in comparison to microstructured thin films (see for example chapter 4, or reference [7], where the excitation conditions were the same with this experiment). The origin of the poorer performance is the relatively short length of the cavity, limited by the thickness of the polymer film. Consequently in order for the gain to exceed the losses, higher singlet exciton densities are required for lasing threshold. To overcome this, thicker polymer films should be employed, but longer cavity lengths are expected to decrease the spectral purity of the emitted beam. In the context of fabrication, microcavity resonators exhibit additional drawbacks, mainly due to the relatively long preparation method, the high cost of the mirrors and the incompatibility with cost-effective fabrication techniques such as soft lithography.

5.3 Microstructured DBR polymer lasers

5.3.1 Introduction

As for the case of photonic crystal polymer lasers, in DBR lasers the feedback arises from diffraction from a microstructured fused silica substrate. The substrate comprises two components: the two Bragg mirrors and a planar area in-between them, onto

which a 120 nm thick MEH-PPV film is deposited*. The planar middle area will be referred to as defect, since it is the component that breaks the translational symmetry of the microstructure. In figure 5.3.1 a general schematic of such a structure is shown: the planar polymer film in the defect area acts as an amplifier and the adjacent gratings form the resonator. The optical excitation is centered in the planar polymer film and the emission forms a standing wave field in the polymer guide due to the reflection from the Bragg mirrors.

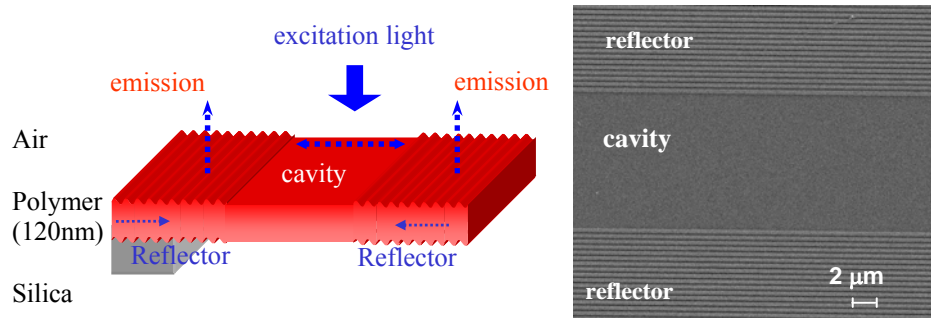


Figure 5.3.1: *Left:* A cross-sectional schematic of a polymer DBR laser. *Right:* An SEM image of the fused silica oscillator.

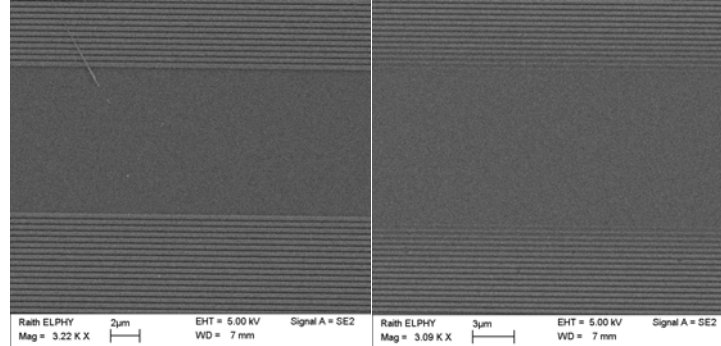


Figure 5.3.2: An SEM image of a proximity corrected DBR structure (*left*) and a similar of an exposed structure, where proximity correction was not implemented.

The fused silica resonator was defined using electron beam lithography. For these structures it was found the implementation of the proximity correction was relatively critical as described in chapter 3. In figure 5.3.2, SEM images of two DBR silica resonators are shown: the left one is proximity corrected, while for the right one the correction was not implemented. In the absence of correction, the width of the grating

* The spin coating conditions were the same as in section 5.2.

lines in the mirrors varies significantly in the proximity of the defect area. This occurs due to the difference of the exposure dose between the mirror and the defect regions.

For these experiments, the mirrors were designed as second order linear gratings with lattice constant $\alpha = 408$ nm and fill factor 31 %. With such gratings, the laser field localises in the defect area and is both reflected in the plane of the guide and scattered from the surface, through second and first order diffraction respectively. In this way, a compact and surface-emitting polymer laser is formed. In figure 5.3.3, SEM images of the Bragg mirror at high magnification (*left*) and a detail of the edge of the mirror and the defect area are shown (*right*). The area between the gratings is etched to a depth of approximately 100 nm, allowing the formation of a channel waveguide for lateral confinement.

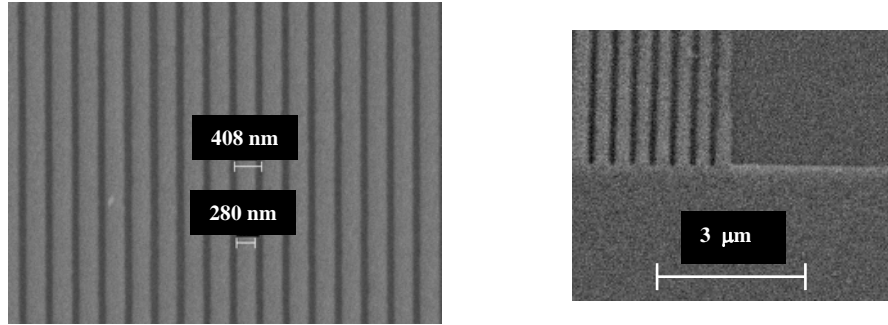


Figure 5.3.3: SEM image of the linear second order grating that acts as the Bragg mirror (*left*) and a detailed image taken at the edge of the a mirror and the defect area (*right*).

5.3.2 Characterisation below threshold

In order to investigate the spectral properties of polymer DBR lasers, the microstructures were first optically excited below threshold. For this investigation, a defect size of $50 \mu\text{m}$ was initially chosen, while the dimensions of the mirrors were $40 \times 100 \mu\text{m}^2$. Both the mirrors and the defect area were illuminated and the spontaneous emission was collected in a direction normal to the plane of the polymer

film with a fibre-coupled CCD spectrometer. The measurements are depicted in figure 5.3.4.

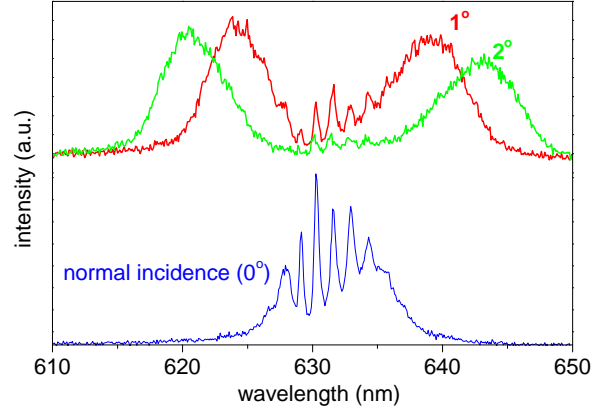


Figure 5.3.4: The spontaneous emission from a 50 μm long defect cavity at normal incidence (blue) and at 1 and 2 degrees from the normal (red and green respectively).

At normal incidence, six distinct resonant modes are detected from the surface, periodically spaced at approximately $\Delta\lambda = 1.2$ nm. These modes are the cavity's defect modes, at frequencies within the stop-band of the Bragg mirrors. As in the microcavity case, these modes are evanescent in the adjacent mirrors, but spaced more closely due to the longer cavity length, which is not limited by the film thickness. The angle-dependent photoluminescence measurements are shown in figure 5.3.4. At small angles away from the normal, the resonant modes do not show an angular dispersion, in agreement with those of the microcavity (figure 5.2.3). On the other hand, there are two additional peaks, whose resonant wavelength changes with the scattering angle. These modes can be identified as surface-coupled Bloch modes of light emitted within the Bragg mirrors (section 3.4.2). The peak wavelength, full width at half maximum and the Q-factors of the resonant defect modes are shown in the following table:

mode	wavelength (nm)	F.W.H.M. (nm)	Q-factor
1	629.12	0.27495	2288.12
2	630.32	0.34213	1842.34
3	631.63	0.39196	1611.46
4	632.99	0.52406	1207.86
5	634.33	0.52298	1212.92

One of the distinct differences of the polymer microcavity with the DBR is that the quality factors of the resonant modes decreases with wavelength. On the contrary, in the microcavity case the Q-factor slightly increased with wavelength. The origin of this is attributed to the different out-of-plane radiation losses that each DBR defect modes experiences. This effect is not present in the microcavity, where the reflectivity is due to purely in plane Bragg scattering.

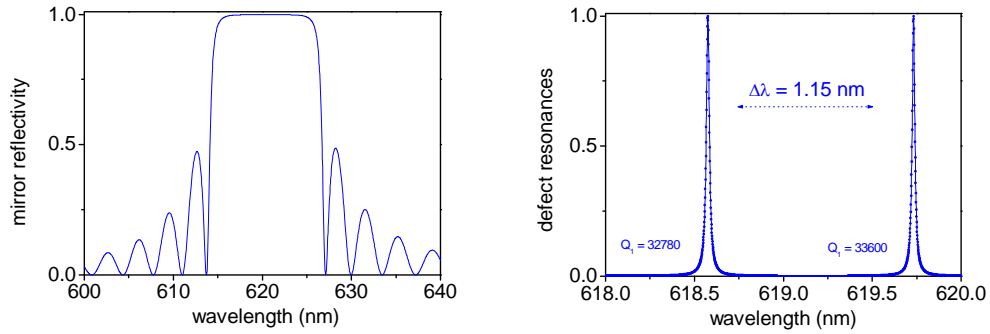


Figure 5.3.5: TMM calculations corresponding to the reflectivity of a single Bragg mirror ($\alpha = 408 \text{ nm}$, f.f.: 31 %, *left*) and to the transmission of the $50 \mu\text{m}$ defect cavity within the stop-band (*right*).

To further investigate this, Transfer Matrix Method calculations (TMM) [8] were performed for the DBR. The results are shown in figure 5.3.5 for the reflectivity of the single mirror (*left*) and the transmission of the composite system including the $50 \mu\text{m}$ defect (*right*). The defect modes manifest themselves with the high transmission resonances at wavelengths within the high reflectivity bands of the Bragg gratings. It was found that the Q-factor does not vary significantly with wavelength because the TMM calculations are purely one-dimensional and the out-of-plane radiation losses are not considered.

The effect of the diffractive losses has been investigated in the context of circular DFB lasers using coupled-wave mode theory [9]. In this work, the gain curve was calculated for both positive and negative detuning from the Bragg condition for an ideal square pulse shape index modulation. It was found that the modal gain is lower for shorter than longer wavelengths within the stop-band. Such calculation suggests that the losses are lower for longer wavelengths, in contrast to what I experimentally observed. A

possible reason for this discrepancy is that the experimental refractive index modulation is not uniformly square as in the aforementioned reference. The polymer film distribution is expected to be non-uniform within a unit cell with a non-flat top surface and this may reverse the radiation losses variation across the stop-band of the Bragg mirrors. An exact calculation would require prior knowledge of the polymer film distribution within the grating.

It was also observed that the number of defect modes depends on the length of the defect. This was experimentally investigated by performing the same spectroscopic studies for two additional cavities of 20 μm and 30 μm defect sizes. The spontaneous emission spectra are shown in figure 5.3.6. For the 20 μm defect, two resonant modes are present, while an additional mode is observed for the 30 μm case. This is anticipated since the resonance condition for the longitudinal modes is dependent on the length of the cavity, as in the microcavity case.

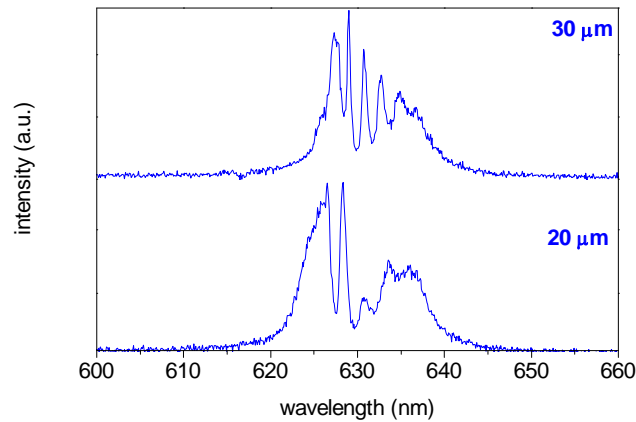


Figure 5.3.6: The surface-emitted spontaneous emission spectra for defect sizes of 20 and 30 μm .

The Q-factor of the defect modes was found also to be dependent on the defect size. In figure 5.3.7, the Q values for the two shortest wavelength resonant modes are plotted as a function of the physical mirror separation. This dependence was measured to be linear, with a slope approximately 3 % higher for the shorter wavelength mode. The linear dependence is also expected, since longer cavity lengths allow longer photon lifetimes [10]. In addition, this linearity suggests that the mirror losses are the same

irrespective of the defect size, confirming the similar mirror quality and the reproducible fabrication.

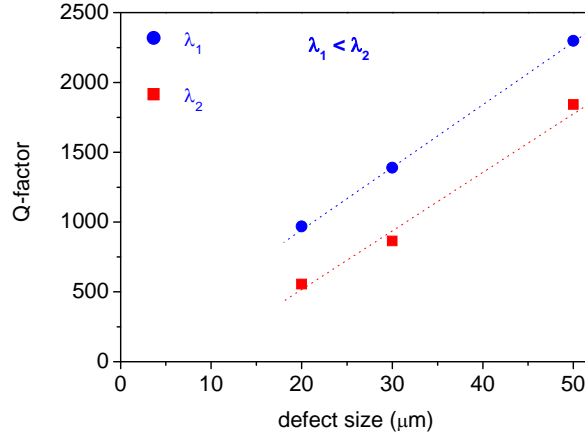


Figure 5.3.7: The variation of the Q-factor of the resonant defect modes as a function of the physical mirror separation.

5.3.3 Characterisation above threshold

The spectra below and above threshold (*left*) and input-output relationship (*right*) are shown in figure 5.3.8 for a defect size of 30 μm. Below threshold, the intensity of all the defect modes increases linearly with the pump energy. For excitation pulse energies above 2.4 nJ, the intensity of the shortest wavelength defect mode increases at a higher rate and, as observed in the microcavity, the others remain ‘pinned’ at the same intensity level. This behaviour is a clear indication of the laser being pumped above threshold; at higher excitation energies the emission spectrum becomes dominated by the intensity of a single defect mode. The threshold of the polymer DBR resonators is significantly lower than the microcavity lasers and this is attributed to the increased cavity length and consequently to the increased amplification experienced in a single round-trip.

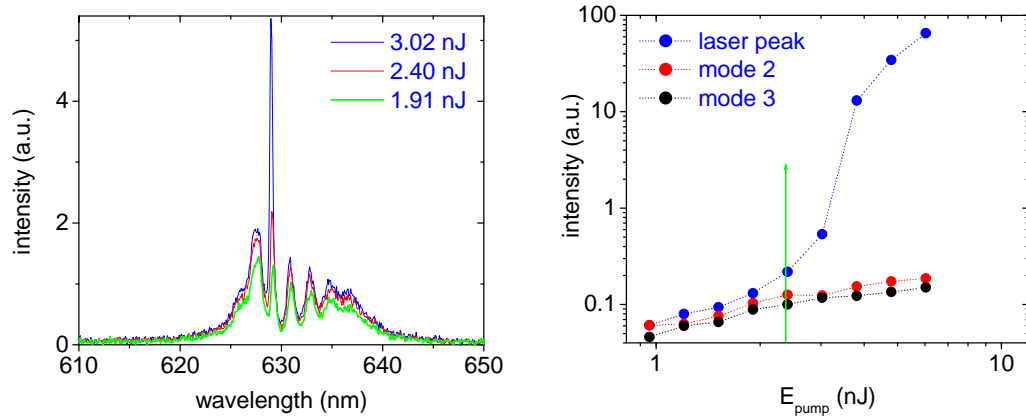


Figure 5.3.8: *Left:* the spectra below (green) and above (blue and red) threshold. *Right:* the input output relationship for the DBR laser is a log-log scale.

The laser operation of DBR lasers for defect sizes of 20, 30, 50 and 90 μm is illustrated in figure 5.3.9. All devices displayed single mode operation, which always takes place at the shortest wavelength defect mode. This behaviour was observed for excitation energies up to 30 nJ, above which significant levels of photo-oxidation resulted in a permanent damage of the conjugated polymer films. The origin of the single mode laser operation is attributed to the different scattering losses that each defect mode experiences, as identified by the wavelength variation of the Q-factor in the previous section.

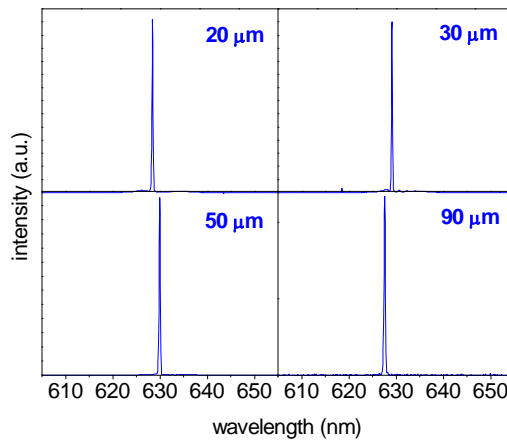


Figure 5.3.9: The spectra above threshold for different defect sizes, at excitation densities corresponding to 1.25x above threshold.

In order to further investigate the performance of the DBR lasers, the threshold variation as a function of the defect size was measured. The different DBR resonators studied were on a single wafer, thus maintaining similar testing conditions for different structures. The excitation area had a radius of 40 μm for the DFB case (no defect), while for the DBRs it inevitably varied within 25 % due to the different positions of the resonators on the sample with respect to the focusing length^{*}. In figure 5.3.10, the lasing threshold variation for the different defect sizes are shown. The principal feature to note on this graph is that the threshold of all DBR polymer lasers is lower than the threshold of the DFB case, where the size of the defect is zero. The higher threshold for the DFB (zero defect size), in comparison to the DBR suggests that the cavity losses are lower in the presence of the defect. This is attributed to the main structural difference between the two resonators, namely the separation of the regions of population inversion and the refractive index modulation. As discussed in chapter 4, second order gratings induce extensive radiation losses, which increase the threshold of the DFB lasers. In the case of the DBRs however, this type of losses is expected to be lower since the coupling to free space takes place in an area smaller than the total cavity length.

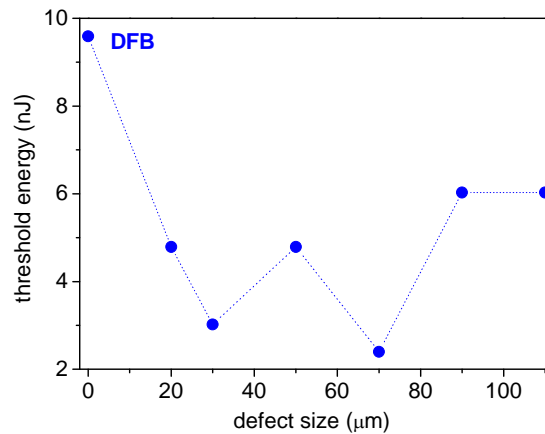


Figure 5.3.10: The lasing threshold energy variation for the different defect sizes.

An additional consequence of the mirror separation is the planarisation of the top surface of the amplifier. When a polymer film is spun on top of a corrugated substrate,

^{*} At the time of the thesis more detailed experiments on the DBRs were not possible due to equipment issues in regards to the microchip laser.

the corrugation is transferred to the top-surface of the polymer film. The associated non-uniformity can lead to extensive incoherent scattering losses. The top surface roughness was identified by Atomic Force Microscopy (AFM) and shown in figure 5.3.11 (*left*) for a measurement taken for a MEH-PPV coated DBR and in a region sampling both the grating and the defect. In contrast to the grating areas, the top-surface of the polymer in the defect region is planar.

A third factor which is also expected to contribute to the threshold decrease is the increased chromophore density in the amplifying region of the DBRs. In these structures, the refractive index modulation is absent in the amplifier area and its volume is solely comprised of excited chromophores that give gain. On the contrary, in the DFB case the chromophore density is limited by the fill factor of the grating and consequently the energy transfer from the pump source to the gain medium is not expected to be as efficient (figure 5.3.11, *right*).

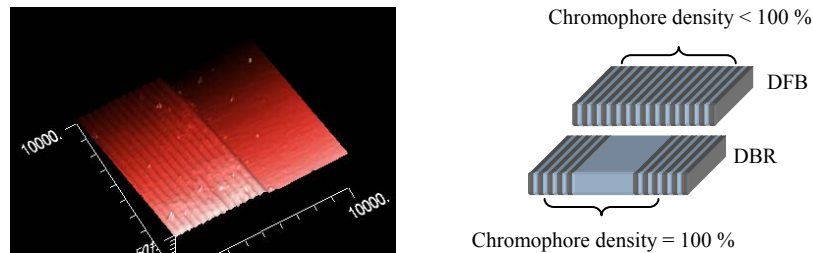


Figure 5.3.11: *Left:* AFM images taken from a polymer film on top of a DBR, sampling both the grating and defect areas. *Right:* A schematic illustrating the chromophore density differences between the DBR and the DFB.

5.4 Diode pumped polymer lasers

5.4.1 Introduction

The excitation scheme of polymer lasers involves a pulsed laser and as mentioned in the introduction, one of the current objectives in the field of solid-state polymer lasers

is the decrease of the size and the complexity of the pump source. To this end, GaN diode lasers are a promising candidate, since their violet emission lies within the absorption spectrum of most organic materials. Their direct electrical excitation and the absence of frequency up-conversion optical components also allow the realization of compact resonators.

The significant challenge in demonstrating direct diode-pumped organic lasers is the low output powers from GaN laser diodes, which places strong demand on achieving low thresholds by using optimised resonators and gain media. To this end, several groups have recently attempted this, mainly focusing on polyfluorene derivatives as gain media and distributed feedback resonators [11, 12]. Within this thesis, diode pumped organic lasers were demonstrated based on the surface emitting DBR resonators and the poly(paraphenylene-vinylene) derivative MEH-PPV [13].

5.4.2 Gain medium

The pump source used was a GaN diode laser emitting at a wavelength of 409 nm. At this wavelength, the absorption of the MEH-PPV is low (figure 5.4.1, *left*) and to overcome this, a strategy of light harvesting with a second chromophore was explored. This involved non-radiative energy transfer by blending the MEH-PPV in an appropriate host [14, 15]. The dye Coumarin 102 (Lambda Physik) was employed, which fluoresces at the absorption maximum of the MEH-PPV and also exhibits a strong absorption band at the GaN laser emission wavelength. The diode laser light harvesting was optimised in this way and an increase of the absorption coefficient by a factor of 3 at the wavelength of interest was achieved with this method (figure 5.4.1, *left*) [13].

The energy transfer process was investigated in the context of both the photoluminescence quantum yield (PLQY) and the threshold of the Amplified Spontaneous Emission (ASE) [13]. The ASE experiments were performed by exciting

the films with the 407 nm emission from an OPO (Continuum Panther EX) focused to a stripe with dimensions 170 μm by 3.8 mm and the results are plotted in figure 5.4.1 (right). In terms of incident pump energies a clear threshold minimum occurs at the concentration of 50:50 wt. %. When correcting for the amount of light absorbed in each blend, the ASE thresholds become comparable indicating the successful light harvesting of the blend, while maintaining the amplifying properties of the conjugated polymer. At high concentrations (>50 % per weight), the ASE threshold increases and a possible explanation for this effect is the increased scattering losses due to the formation of aggregates, or a phase separation between the dye molecules and the polymer. In the following experiments the optimal blending concentration of 50:50 wt. % was used.

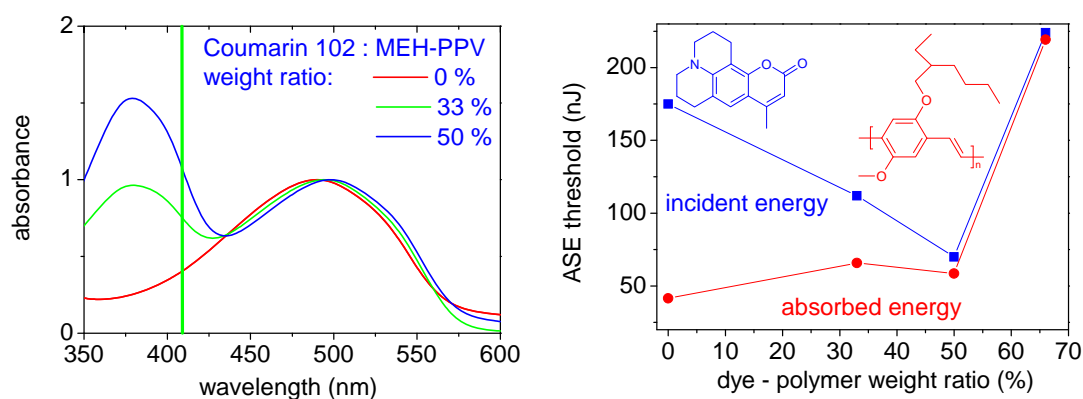


Figure 5.4.1: *Left:* The absorption spectra of the MEH-PPV neat film and its blends with Coumarin 102 at concentrations of 33 and 50 wt. %; the green arrow denotes the emission wavelength of the GaN diode laser. *Right:* the variation of the ASE threshold as a function of the dye-polymer weight ratio, both for the incident energy (blue) and the absorbed energy (red). *Inset:* the molecular structures of MEH-PPV (red) and Coumarin 102 (blue). The ASE and absorption experiments were performed with G. Tsiminis and J.-C. Ribbierre.

5.4.3 Lasing studies

The diode laser used for lasing studies was a pulsed GaN purchased from Jobin Yvon Horiba. The maximum pulse energy and the pulse duration were 0.67 nJ and 1 nsec respectively, while the variable repetition was set at 10 kHz for these experiments. The output from the diode laser was astigmatic and highly divergent and was focused using a spherical lens to an elliptical spot on the surface of the polymer laser with a diameter along the major and minor axis of 76 μm and 66 μm respectively. In the optical

experiments care was taken so that the major axis of the excitation area was parallel to the resonant axis of the cavity and that the polarisation of the pump light was parallel to the grating grooves. The configuration of the polymer DBR resonators was as described in section 5.2.1.

In figure 5.4.2 (a) typical emission spectra below and above threshold are shown for a mirror separation of $20\text{ }\mu\text{m}$. Below threshold, the spontaneous emission couples to four distinct optical modes at 624 nm , 625.7 nm , 628.2 nm and 630.4 nm . As discussed in section 5.3, the modes at the shortest and longest wavelength correspond to the Bragg scattered modes that originate from the periodic nature of the gratings. Their presence is enhanced by the optical excitation of the grating mirrors since the excitation spot is larger than the mirror separation. The intermediate modes at wavelengths 625.7 nm and 628.2 nm are the resonant modes of the DBR cavity. These modes appear within the stop-band and are excited only when the pump light is centered between the Bragg mirrors.

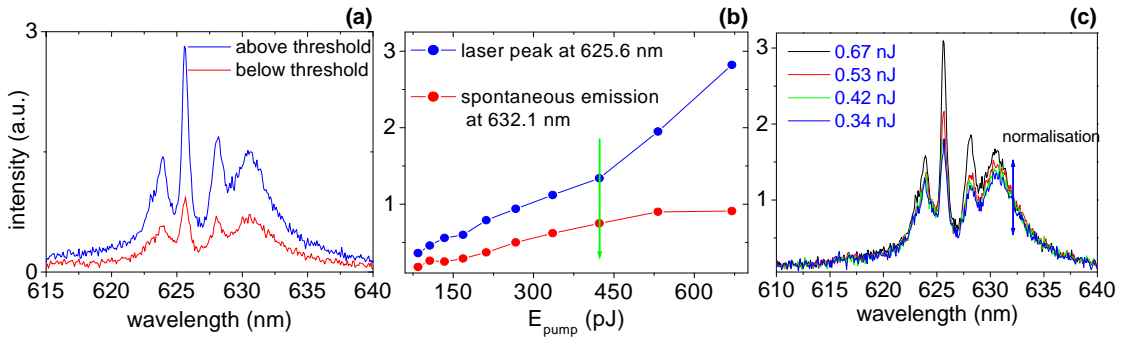


Figure 5.4.2: (a): The emission spectra above (0.67 nJ) and below threshold (0.27 nJ). (b): The input-output relationship for the laser peak at 625.6 nm (blue) and the spontaneous emission at 632.1 nm (red). The lines are a guide to the eye. (c): The normalized emission spectra for different excitation densities. The normalization level was chosen at the wavelength of 632.1 nm.

Above an excitation energy of 0.42 nJ , a change in the emitted light is observed. This can be seen in figure 5.4.2 (b). There is an increase in growth of the DBR mode at 625.6 nm and a flattening of the spontaneous emission at 632.1 nm . The faster growth of one of the modes and the pinning of the others is an indication of lasing, as described in section 5.3. This behaviour can also be seen in figure 5.4.2 (c), where the

emission spectra are normalized at the wavelength of 632.1 nm. Below threshold, the spectra evolve linearly with the pump intensity and hence completely overlap when normalized. Above threshold, the laser peak increases faster than the background indicating the non-linearity associated with stimulated emission. The same behaviour was observed for 30 and 50 μm cavity lengths.

The state of polarisation of the pump light was found to be of critical importance at these low excitation energies. This is illustrated in figure 5.4.3, which shows the evolution of the emission spectra with the excitation density for the two different polarisation states of the pump light. When the polarisation is perpendicular to the grating grooves, the spectra evolution denotes the absence of lasing (left), in contrast to the same experiment when the polarisation is parallel to the grating grooves (right).

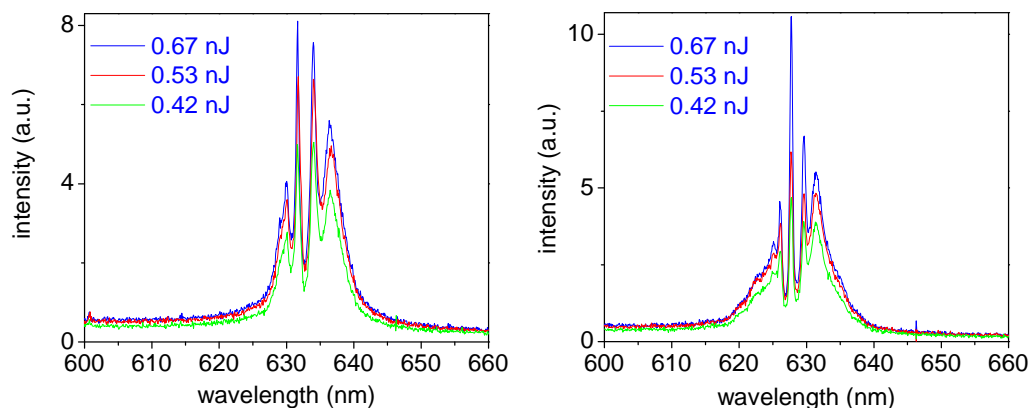


Figure 5.4.3: The evolution of the emission spectra from a 20 μm defect polymer DBR laser pumped with the GaN diode laser of different polarisations. The polarisation state is perpendicular (*left*) and parallel (*right*) to the grating grooves.

The origin of this observation is based on the selective excitation of the conjugated polymer segments depending on the polarisation state of the pump light. Under the dipole approximation, the excited polymer chains emit in a direction perpendicular to the chain axis. Assuming that most of the chains lie in the plane of the film, then for a polarisation state of the pump light perpendicular to the grating grooves, the organic chromophores emit at an angle of 90° to the resonator axis. For the parallel polarisation state, only the segments of the polymer chain perpendicular to the cavity axis are

excited. Consequently, the spontaneous emission couples more effectively to the cavity modes, since it is emitted in the same direction as the resonator axis.

Due to the limited output power from the GaN diode, the polymer DBR laser exceeded threshold by only 50 %. It is intriguing that at the time of the thesis, other researchers have not succeeded in demonstrating a diode pumped solid-state laser far above threshold, despite the employment of significantly optimised material combinations [11, 12]. In my experiments, commercially sourced materials were used and this achievement is attributed to the optimisation achieved with the DBR resonators.

5.4.4 Summary

In conclusion, a solid-state polymer laser pumped with an inorganic diode laser was discussed in this sub-section of the DBR polymer lasers chapter. The DBR resonator acted as a low threshold, surface-emitting laser and its optimised performance allowed this demonstration. A blend based on the dye Coumarin 102 and the conjugated polymer MEH-PPV was used to allow the efficient energy transfer from the GaN laser to the conjugated polymer. The importance of the state of the polarisation of low power pump sources was analysed, in the context of the selective excitation of the polymer chains that have a higher probability of coupling to the cavity modes and thus achieving lower oscillation thresholds.

The demonstration of diode-pumped polymer lasers is of significant importance in the field of solid-state polymer lasers, aiming towards less complex and more compact optical systems. The historical review of this field is illustrated in figure 5.4.5, where the size of the pump sources is plotted against their maximum output power. Since the first demonstration of a solid-state polymer laser pumped with a frequency doubled regenerative amplified Nd: YAG laser in 1996, a significant progress has been

achieved, due to the optimisation of both the involved gain materials and the resonators.

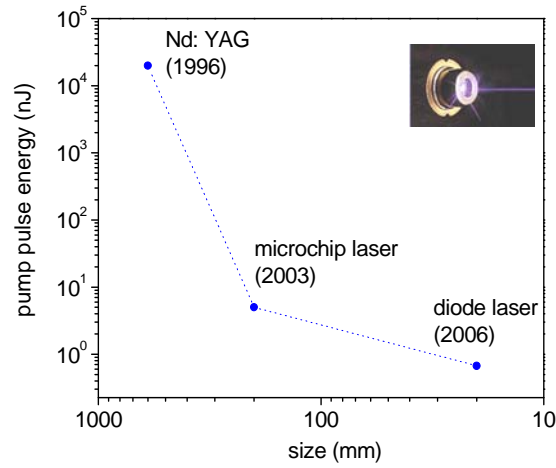


Figure 5.4.5: A graphical illustration of the evolution in the field of solid-state organic semiconductor lasers, from 1996 to 2006.

5.5 A silicon based polymer laser

5.5.1 Introduction

In this section, the demonstration of a silicon-polymer hybrid laser will be outlined. This type of structure was realised by combining microstructured silicon resonators and light-emitting organic semiconductors that provided the gain. Under optical excitation, the structure operated as a visible surface-emitting laser. The motivation for this type of device was to investigate as an alternative route to the realization of cost-effective optical interconnects based on CMOS fabrication processes, in which the integration of solution processible polymers adds only a simple supplementary fabrication step.

To this end, two significant challenges had to be addressed. One is the high dielectric constant of silicon, which presents serious constraints in realizing a polymer

waveguide, necessary for high amplification factors. The next constraint is the high absorption coefficient of silicon in the visible spectral range, which can act as an efficient quencher of the luminescence of polymers in the vicinity of silicon. Both of these challenges were addressed through a Distributed Bragg Reflector resonator design, based on a silicon-on-insulator (SOI) wafer.

The SOI substrate used had a silicon epilayer of 220 nm and an oxide layer of 2 μm on a silicon substrate. The developed structure is shown in figure 5.5.1. Two periodically microstructured Si segments act as Bragg reflectors and the Si epilayer in-between them is removed completely until the underlying SiO_2 layer is reached. The organic amplifying medium covers both regions and the area between the two periodically microstructured Si reflectors acts as a defect, breaking the symmetry of the Si photonic lattice. Due to the boundary conditions at the air-polymer and polymer- SiO_2 interfaces, a polymer waveguide is formed with the confinement factor limited only by the thickness of the polymer layer. The introduction of the polymer defect also served as a method to minimize the interaction of the laser light with the Si regions and address the high absorption coefficient of Si.



Figure 5.5.1: A schematic of the hybrid Si-polymer resonator.

To fabricate^{*} the structure, the thickness of the epilayer was initially decreased from 220 nm to 30 nm using fluorine based reactive-ion chemistry. The Bragg mirrors were defined using electron beam lithography on poly(methyl methacrylate) (PMMA), followed by the evaporation of a 30 nm Ni layer that acted as an etch mask during the pattern transfer into the Si epilayer. The Si microstructures were linear gratings with a period of 360 nm and fill factor of 30 %. The low fill factor was chosen in order to

^{*} The fabrication was performed by S. Moore.

minimise the volume of Si within the unit cell. For this lattice constant, and at the wavelength of 630 nm, the stop-band of the Bragg mirrors originates from second order diffraction and provides both the feedback and surface emitted output coupling. The emission wavelength of the polymer lies within the absorption band of silicon photodetectors, and in conjunction with the surface coupling of the laser emission, could be compatible with the prospect of lateral chip integration [16]. A 50 μm long defect area was defined between the mirrors and both components were coated with a 120 nm thick film of the conjugated polymer MEH-PPV*.

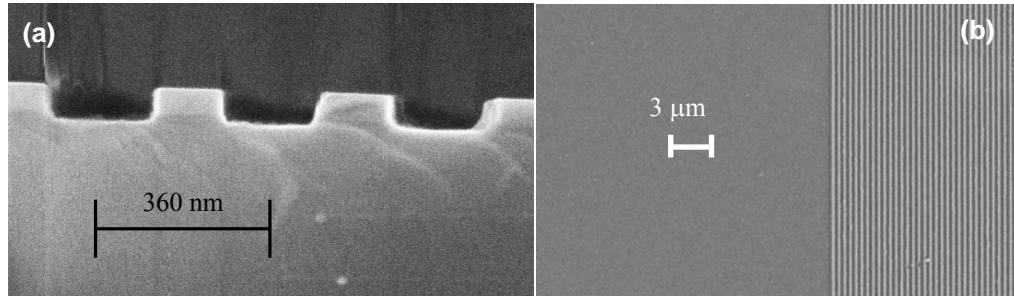


Figure 5.5.2: SEM images of the side and top view of the Si on insulator resonator in (a) and (b) respectively. *Image (a) was provided by S. Moore.*

5.5.2 Characterisation

The laser characterisation involved the optical excitation of the hybrid structures using the frequency-doubled microchip laser. The pump beam was focused to an excitation area of 85 μm in diameter and the emission from the polymer laser was collected from the surface using a fiber coupled CCD spectrometer of 2 \AA resolution.

In figure 5.5.3, the emission spectra below and above threshold for a 50 μm long defect are plotted (*left*). Below threshold, the spontaneous emission from the conjugated polymer couples to optical modes with frequencies within the stop-band of the Bragg mirrors. These modes manifest themselves in a series of narrow peaks, with a free spectral range of $\Delta\lambda = 1.25$ nm corresponding to an effective cavity length of

* The MEH-PPV film was spun from a chlorobenzene solution at a concentration of 5.2 mg/ml and at a spin speed of 1180 rpm.

150 μm . The band-edge modes are not evident below threshold in contrast to the case where the mirrors were based on SiO_2 . The likely reason for this difference is that the band-edge modes are Bloch modes, localised in the periodic lattice; consequently, they suffer from high absorption losses at these wavelengths due to the Si, which does not occur in SiO_2 . For excitation energies above 45 nJ, the intensity of the lower wavelength resonant modes increases at a faster rate indicating the laser threshold (figure 5.5.3, *right*) and at higher pumping levels they dominate the emission spectrum. Not all the waveguide modes reach threshold and this is attributed to the different absorption mirror losses that each mode experiences. These are expected to be wavelength dependent due to the different localization of the light in the Bragg mirrors.

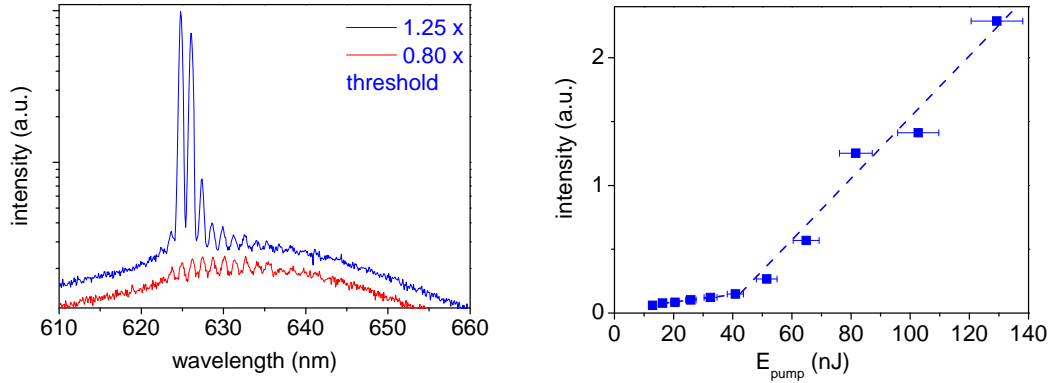


Figure 5.5.3: *Left:* The emission spectra above and below threshold for a 50 μm long polymer defect in the Si lattice. *Right:* the input-output relationship.

The number of longitudinal modes above threshold was found to be dependent on the size of the defect area. By increasing the length of the mirror separation, more longitudinal modes appear above threshold, broadening in this way the spectrum of the laser emission. The reason for this is that for longer defects, the effective cavity length increases and thus the resonant condition is satisfied at more wavelengths. In figure 5.5.4 (*left*), the surface-coupled emission spectra for three different defect sizes are plotted, at an excitation level of 1.25 times above threshold. For each defect size, the effective cavity length was deduced from the mode spacing. The optical dimensions of the cavity were found to vary in a linear fashion with the size of the defect, with a slope of 3.1 (figure 5.5.4, *right*). In DBR lasers, the effective cavity length is the sum

of the optical length of the defect size and the effective grating length^{*}. The slope in figure 5.5.4 (*right*) corresponds to the group index of the polymer waveguide (n_g) through the following relationship [17]:

$$L_{\text{eff. cavity}} = n_g \cdot L_{\text{defect}} + 2 \cdot n_g \cdot L_{\text{eff. grating}} \quad (5.1)$$

The group index for a 120 nm thick MEH-PPV film was calculated, considering both the material and waveguide dispersion. The material dispersion was identified by Ellipsometric measurements (chapter 3) and the waveguide dispersion was taken into account by solving the wave-equation at each wavelength separately. In this way, the group index can be determined from the slope in the relationship between the propagation constant ($\beta = 2 \cdot \pi \cdot n_{\text{eff}} / \lambda$) and the free space wavevector (inset of figure 5.5.4, *right*). The group index at the wavelength of 625 nm (or $k_0 = 10.04 \mu\text{m}^{-1}$) was found to be 2.7, in good agreement within experimental error with the measured value of 3.1.

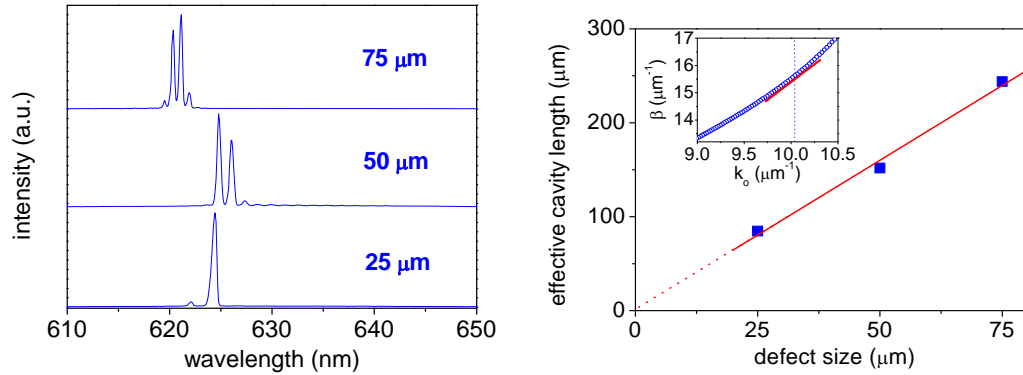


Figure 5.5.4: Left: The broadening of the laser emission spectra for increasing defect sizes. Right: The relationship between the physical length of the defect and the effective cavity length derived from the mode spacing (inset: the calculated variation of the propagation constant as a function of the free space wavevector).

The functionality of this type of devices could be further enhanced by the possibility of tuning the laser emission wavelengths and two main tuning mechanisms were identified. The first is based on the tuning of the laser wavelength with the grating period. It was found that by changing the lattice constant from 360 nm to 330 nm, the

^{*} The effective grating length is equivalent to the photon penetration depth at each mirror.

laser emission blue-shifted by 18 nm. In contrast to defect-free resonators, the tuning rate in the Si based polymer DBR lasers is not equal to the change of the grating period. In figure 5.5.5 (*left*), the contour plot of the reflectivity as a function of wavelength and lattice constant is plotted and the black dots denote the experimental values^{*}. It can be observed that despite the linearity of the maximum of the reflectivity of the Bragg mirrors, the tuning rate does not necessarily follow the same rate. The origin of this effect is attributed to the broad spectral gain of the polymer and the broad bandwidth of the Si mirrors. The threshold condition is satisfied at a wavelength where both the material gain and the mirror reflectivity are at a maximum. This does not necessarily occur at the centre of the stop-band (dotted line), since the reflection coefficient is constant across its width.

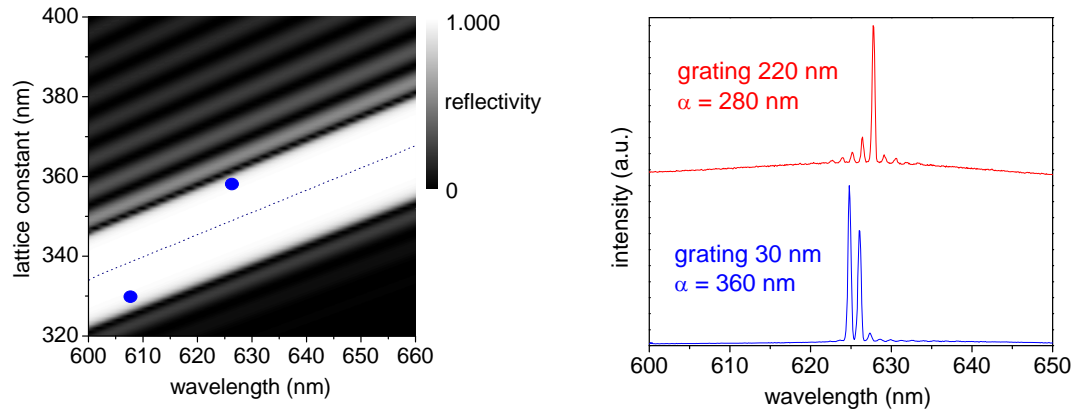


Figure 5.5.5: *Left:* A contour plot of the reflectivity as a function of wavelength and lattice constant. The dotted line denotes the reflectivity maxima and the blue dots the experimental values. *Right:* The emission spectra for a grating thickness of 220 nm (period: 280 nm) and 30 nm (period: 360 nm). The defect size in both cases is 50 μm and the polymer film thickness 120 nm.

A different tuning mechanism can be also based on the thickness of the Si grating. Thicker Si gratings correspond to an increased index contrast within the unit cell and consequently the Bragg condition for lasing is satisfied at longer wavelengths for the same lattice constant. This was confirmed for a 220 nm thick Si grating, where in order to achieve laser operation at the wavelength of 630 nm and for the same polymer film thickness, the grating period was decreased by 80 nm. The results are plotted in figure 5.5.5 (*right*). The values of the grating periods in both cases were found to be in good

^{*} The calculation was based on the transfer matrix method, and the mirrors consisted of 20 layers.

agreement with transfer matrix calculations [18]. However, an exact quantification would require a three-dimensional calculation.

5.5.3 Comparison with SiO₂ mirrors

In order to further investigate the performance of the hybrid Si-polymer lasers, I compared their lasing characteristics with those of DBR cavities of similar dimensions, but fabricated on fused silica substrates (section 5.3). One difference is the multiple longitudinal mode operation in the hybrid Si-polymer lasers, which is not observed in the fused silica case. As discussed in section 5.3, the single frequency operation in the SiO₂ case is attributed to the wavelength dependent scattering losses that each resonant defect mode experiences across the stop-band of the Bragg mirrors. This type of scattering loss is not expected to be significant in the Si case because the absorption losses are dominant. In addition, the width of the reflectivity band in the Si case is significantly broader and consequently the scattering losses are also not expected to vary significantly in the wavelength range that lasing is experimentally observed.

The thresholds were also different between the two cases. The Si based laser had a threshold of approximately 40 nJ, while the threshold for the SiO₂ based laser was almost an order of magnitude lower at 4.75 nJ. The improved performance in the all-silica case is attributed to the lower round-trip losses that the laser field experiences in comparison to the Si based laser. This effect was quantified through the threshold condition in the Si and SiO₂ based lasers, according to which the gain at threshold is equal to the sum of the polymer waveguide and mirror losses. If ‘ α ’ and ‘ R ’ are the waveguide loss and modal reflectivity respectively, then for a cavity length L and confinement factor Γ , the gain at threshold (g_{th}) can be expressed through the following relationship [19]:

$$\Gamma \cdot g_{th} = \alpha_i + \frac{1}{L} \cdot \ln\left(\frac{1}{R}\right) \quad (5.2)$$

For a cavity length of 50 μm and similar polymer film thickness, the confinement factor and the waveguide losses are the same in both the Si and SiO_2 case. The waveguide loss and confinement factor have been measured at 20 cm^{-1} and 0.35 respectively [20, 21]. The gain at threshold (g_{th}) was determined through the product of the stimulated emission cross section for MEH-PPV ($\sigma = 3 \cdot 10^{-16} \text{ cm}^2$ [22]) and the singlet exciton density at threshold (N_{th}). The exciton density was determined by numerically solving the exciton rate equation, where the exciton-exciton annihilation (at a rate $\gamma = 10^{-8} \text{ cm}^3/\text{s}$ [22]) and the exciton lifetime ($\tau = 300 \text{ ps}$ for MEH-PPV [20]) were taken into account [22]:

$$\frac{dN(t)}{dt} = \Lambda(t) - \frac{N(t)}{\tau} - \gamma \cdot N^2(t) \quad (5.3)$$

The time dependent term Λ accounts for the pumping rate, which for the purposes of this calculation was assumed to have a top-hat shape during the pulse duration. The pulse energy at threshold (E_{th}), excitation volume* (V_{exc}) and pulse duration (t_p) were experimentally determined for both the Si and SiO_2 lasers. Consequently the pump rate can be determined through the relationship:

$$\Lambda(t) = \frac{E_{\text{th}}}{V_{\text{exc}} \cdot h \cdot \nu \cdot t_p}, \text{ for } 0 \leq t \leq t_p \quad (5.4)$$

By determining the singlet exciton density and thus the gain at threshold, the modal reflectivity can be deduced for the Si and SiO_2 cases from relationship 5.2. The results are in the following table:

Mirror	L (cm)	E_{thr} (nJ)	V_{exc} (cm^3)	N_{th} (cm^{-1})	$\Gamma \cdot g_{\text{th}}$ (cm^{-1})	R
Si	0.05	41	$6.60 \cdot 10^{-10}$	$1.24 \cdot 10^{18}$	371.8	17.20%
SiO_2	0.05	4.79	$2.22 \cdot 10^{-10}$	$9.78 \cdot 10^{17}$	293.5	25.47%

* The excitation volume was determined via the product of the excitation area and film thickness, assuming that the pump light is uniformly absorbed throughout the film.

The Si modal reflectivity was calculated to be approximately 10 % lower than the all-silica case. This result is anticipated, because the number of photons reflected back into the defect in the Si case is expected to be lower due to the additional absorption losses that are not present in the SiO₂ mirrors. This difference in reflectivity is the origin of the observed difference in the thresholds between the two lasers.

5.5.4 Summary

A hybrid Si-polymer laser was the theme of this section. This laser was fabricated based on Si processing and solution processible conjugated polymer provided the optical gain. The motivation behind this study was to investigate alternative routes to cost-effective silicon based optical interconnects. The laser resonator was based on a novel DBR design on SOI substrates and was configured as surface-emitting.

In regards to the laser characterisation, this was performed both below and above threshold. It was found that the presence of Si in the Bragg mirrors hinder the appearance of the band-edge modes in the surface-scattered spontaneous emission spectra. Multi-mode operation was measured above threshold and a functional method to control the number of longitudinal modes based on the size of the defect was investigated. The simultaneous presence of multiple longitudinal modes is favored by the broadband gain spectra of conjugated polymers, which is of significant importance for communication applications due to the possibility of transferring and processing information through multiple wavelength channels [23]. This experiment allowed also the determination of the group index of the MEH-PPV waveguide. The functionality of this type of lasers was enhanced by investigating means to tune the emission wavelength. Two basic mechanisms were identified, namely the change of the grating period and the thickness of the silicon grating. A comparative analysis with an all-silica resonator took place in order to investigate the quality of the hybrid Si-polymer resonator. It was found that the round-trip losses are approximately 10 % higher in the Si case due to the absorption losses at the Bragg mirrors.

5.6 Summary

The introduction of a structural defect in a uniform Bragg grating induces resonant modes at frequencies within the stop-band of the periodic structure and intensities primarily localised within the defect. These are the DBR resonators and for second order Bragg gratings can form a compact, surface-emitting polymer laser. DBR polymer lasers offer the advantage of lower threshold in comparison to the absence of the defect. The origin of this optimised performance is attributed to the planarisation of the top-surface of the organic amplifier within the cavity area and the increased chromophore density, which in contrast to DFB polymer lasers is not limited by the fill factor of the grating (section 5.3).

The characterisation of this type of laser for different mirror separations below threshold showed that the number of defect modes can be controlled by the size of the defect. The Q-factor of the resonant modes was found to decrease with the wavelength, indicating the presence of wavelength dependent scattering losses. Each defect mode has a distinct optical frequency and consequently it samples a different area of the unit cell, which is likely to play an important role in the scattering strength it experiences. This wavelength dependent loss was the origin of single mode operation above threshold, irrespective of the size of the defect, at least for the range used in this work.

The optimised performance of the DBR resonators allowed the demonstration of diode pumped solid-state polymer lasers (section 5.4). An inorganic GaN diode laser was employed to this end with a significantly lower output power, in comparison to the frequency doubled microchip laser. Stimulated emission was observed from this optical system, exceeding threshold by approximately 50 %. Such demonstration is promising for practical polymer laser systems as it can allow the substantial reduction of complexity and size of the pump laser.

A novel DBR resonator design based on silicon-on-insulator substrates allowed the integration of polymer with silicon microstructures. With this architecture, the

significant challenges of the silicon absorbance and high refractive index in the visible were addressed and under optical excitation, the hybrid structure operated as a laser. This could provide an alternative route to the realization of cost-effective optical interconnects based on CMOS fabrication processes, in which the integration of solution processible polymers adds only a simple supplementary fabrication step. The laser was configured as surface-emitting, compatible with prospect of the lateral integration with silicon photodetectors.

5.7 References

1. M. Berggren, A. Dodabalapur, R.E. Slusher, 'Stimulated emission and lasing in dye-doped organic thin films with Forster transfer', *Applied Physics Letters* **71**, 2230 (1997).
2. I.P. Kaminow, H.P. Weber, E.A. Chandros, 'Poly(Methyl Methacrylate) Dye Laser with Internal Diffraction Grating Resonator', *Applied Physics Letters* **18**, 497 (1971).
3. N. Tessler, 'Lasers based on semiconducting organic materials', *Advanced Materials* **11**, 363 (1999).
4. N. Tessler, G.J. Denton, R.H. Friend, 'Lasing from conjugated-polymer microcavities', *Nature* **382**, 695 (1996).
5. T. Granlund, M. Theander, M. Berggren, M. Andersson, A. Ruseckas, V. Sundstrom, G. Bjork, M. Granstrom, O. Inganas, 'A polythiophene microcavity laser', *Chemical Physics Letters* **288**, 879 (1998).
6. M. Theander, T. Granlund, D.M. Johanson, A. Ruseckas, V. Sundström, M.R. Andersson, O. Inganäs, 'Lasing in a Microcavity with an Oriented Liquid-Crystalline Polyfluorene Copolymer as Active Layer', *Advanced Materials* **13**, 323 (2001).
7. G.A. Turnbull, P. Andrew, W.L. Barnes, I.D.W. Samuel, 'Operating characteristics of a semiconducting polymer laser pumped by a microchip laser', *Applied Physics Letters* **82**, 313 (2003).
8. A. Yariv, P. Yeh, 'Optical waves in crystals', Wiley Classics Library (2003).
9. G.F. Barlow, K.A. Shore, G.A. Turnbull, I.D.W. Samuel, 'Design and analysis of a low-threshold polymer circular-grating distributed-feedback laser', *Journal of Optical Society of America B* **21**, 2142 (2004).
10. O. Svelto, 'Principles of Lasers', Plenum Publishing, 4th Edition (1998).
11. T. Riedl, T. Rabe, H.-H. Johannes, W. Kowalsky, J. Wang, T. Weimann, P. Hinze, B. Nehls, T. Farrell, U. Scherf, 'Tunable organic thin-film laser pumped by an inorganic violet diode laser', *Applied Physics Letters* **88**, 241116 (2006).

12. C. Karnutsch, V. Haug, C. Gaertner, U. Lemmer, T. Farrell, B. Nehls, U. Scherf, J. Wang, T. Weimann, G. Heliotis, C. Pflumm, J. Demello, D.D.C. Bradley, 'Low threshold blue conjugated polymer DFB lasers', Conference on Lasers and Electro-optics, CLEO, paper CFJ3 (2006).
13. A.E. Vasdekis, G. Tsiminis, J.-C. Ribierre, L.O. Faolain, T.F. Krauss, G.A. Turnbull, I.D.W. Samuel, 'Diode pumped distributed Bragg reflector lasers based on a dye-to-polymer energy transfer blend', *Optics Express* **14**, 9211 (2006).
14. F. Marchioni, R. Chiechi, S. Patil, F. Wudl, 'Absolute photoluminescence quantum yield enhancement of poly(2-methoxy 5-[2'-ethylhexyloxy]-p-phenylenevinylene)', *Applied Physics Letters* **89**, 061101 (2006).
15. V. Bulovic, V.G. Kozlov, V.B. Khalfin, S.R. Forrest, 'Transform-limited, narrow-linewidth lasing action in organic semiconductor microcavities', *Science* **279**, 553 (1998).
16. D.A.B. Miller, 'Optical interconnects to silicon', *IEEE J. Sel. Top. Quantum Electron.* **6**, 1312 (2000).
17. Y.O. Barmenkov, D. Zalvidea, S. Torres-Peiró, J.L. Cruz, M.V. Andrés, 'Effective length of short Fabry-Perot cavity formed by uniform fiber Bragg gratings', *Optics Express* **14**, 6394 (2006).
18. A. Yariv, P. Yeh, 'Optical waves in crystals', Wiley Classics Library, New Jersey (2003).
19. T.F. Krauss, O. Painter, A. Scherer, J.S. Roberts, R.M. De La Rue, 'Photonic microstructures as laser mirrors', *Optical Engineering* **37**, 1143 (1998).
20. M. Goossens, A. Ruseckas, G.A. Turnbull, I.D.W. Samuel, 'Subpicosecond pulses from a gain-switched polymer distributed feedback laser', *Applied Physics Letters* **85**, 31 (2004).
21. G.F. Barlow, A. Shore, G.A. Turnbull, I.D.W. Samuel, 'Design and analysis of a low-threshold polymer circular-grating distributed-feedback laser', *Journal of the Optical Society of America B* **21**, 2142 (2004).
22. D. Amarasinghe, A. Ruseckas, A.E. Vasdekis, M. Goossens, G.A. Turnbull, I.D.W. Samuel, 'Broadband solid state optical amplifier based on a semiconducting polymer', *Applied Physics Letters* **89**, 201119 (2006).
23. M.A. Foster, A.C. Turner, J.E. Sharping, B.S. Schmidt, M. Lipson, A.L. Gaeta, 'Broad-band optical parametric gain on a silicon photonic chip', *Nature* **441**, 960 (2006).

CHAPTER 6:

Fluidic dye lasers based on photonic crystal fibres

6.1 Introduction

The experiments described in this chapter entail the demonstration of a fibre dye fluidic laser based on photonic crystal fibres, in an attempt to further explore the potential of this type of fibres for optofluidics. An additional motivation of this work was to investigate the possibility of realising a laser based on a periodic structure, where the feedback mechanism is provided by the periodicity transverse to the propagation direction. In essence, the laser modes would be Bloch modes propagating along the fibre axis, but originating from the transverse periodicity. Laser action was achieved in these systems, however it was found that the transverse resonant effects due to the periodic microstructure do not play a substantial role in the stimulated emission process. Although the transverse periodicity was irrelevant, an interesting frequency selection mechanism was observed, leading to a free spectral range that does not correspond to the length of the liquid cores.

The detailed preparation and characterisation methods are outlined in section 6.2, while the performance characteristics are analysed in section 6.3. It was found that the energy transfer from the excitation source to the fluidic lasers and the length of the liquid cores were critical in terms of their threshold and slope efficiency. In addition, the practicality of these systems was greatly enhanced by a convenient gain-tuning mechanism that allowed the emission wavelength to be varied from 608 nm to 652 nm by changing the chromophore density in the liquid cores. The details of the

unanticipated intracavity wavelength selection mechanism will be described in section 6.4. This effect was extensively investigated and several physical mechanisms were examined but excluded. The explanation of this laser mode structuring mechanism was based on the experimental observation of the linear dependence of the laser's free spectral range with the physical length of the fibres. Such linear dependence is attributed to a Vernier type resonant mechanism and experimental evidence will be provided for the exact nature of this effect.

6.2 The methodology of photonic crystal fibre based fluidic lasers

The fluidic fibre lasers were based on the photonic crystal fibre ESM-12-01 (Crystal Fibre), which consists of a hexagonal array of 54 capillaries with $3.68\text{ }\mu\text{m}$ in diameter and a silica defect core of $12\text{ }\mu\text{m}$ in diameter. The fused silica cladding and acrylate coating have diameters of $125\text{ }\mu\text{m}$ and $220\text{ }\mu\text{m}$ respectively. The coating of the fibres was removed and the inner side of the capillary walls was not chemically treated, unless otherwise stated. The fibre was examined using a SEM and shown in figure 6.2.1. The preparation of the lasers involved the cleavage of the fibres at appropriate lengths and their subsequent infilling by capillary action from dipping them in a toluene solution of the organic dye Perylene Red.

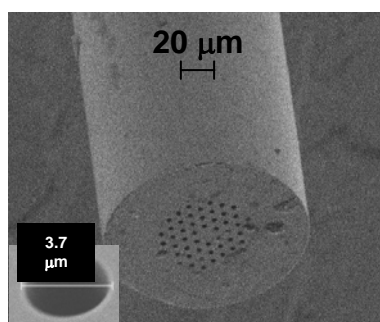


Figure 6.2.1: SEM image of the ESM-12-01 photonic crystal fibre. *Inset:* a higher magnification image designating the lateral dimensions of the individual cores.

Capillary action is the tendency of liquids to rise up in capillary tubes due to surface tension^{*}. The surface tension is the consequence of the molecular interaction between the liquid and the capillary walls that results in the curving of the free surface of the liquid in the capillary. Such curvature implies that the pressure under the surface of the meniscus is higher than the atmospheric pressure and consequently the excess external pressure forces the liquid up the tube until hydrostatic equilibrium. At equilibrium, the liquid has risen at a certain height within the capillary, where the additional pressure induced by the mass of the risen liquid is equal to the pressure difference due to the meniscus [1].

Toluene was chosen for its appropriate wetting properties with the capillary walls that can effectively infill longer pieces of the fibre. It was found that the infilling process was relatively rapid and was measured to be 1 $\mu\text{m}/\text{sec}$ on average for a 25 mm long test capillary tube with a 5 μm core diameter. The infilling process was monitored using a specifically built microscope for both white light illumination and epifluorescence imaging (fig. 6.2.2 a, b).

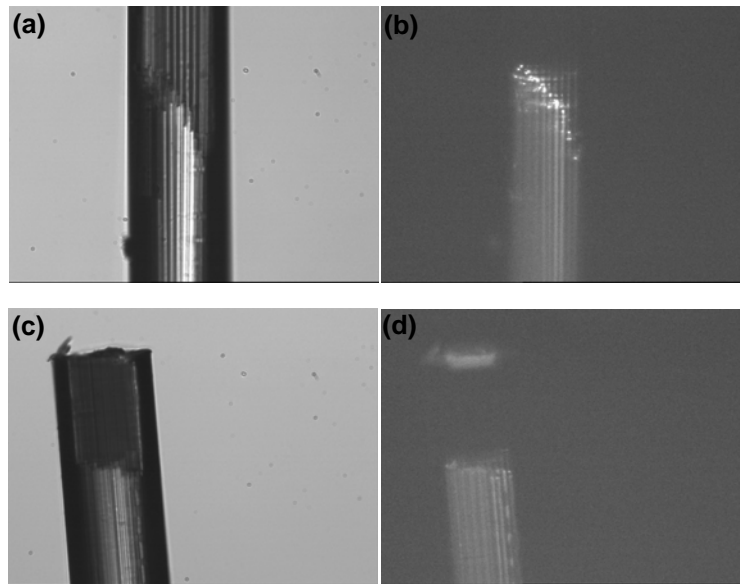


Figure 6.2.2: Microscopy images monitoring the capillary action for an ESM-12-01 in white light illumination (a) and epifluorescence mode (b); Lower set (c, d) corresponds to the same fibre, but imaged at the edge to demonstrate the air-bubble termination.

^{*} The surface tension (γ in N m^{-1}) describes the amount of work required in order to change the area of a surface by $d\sigma$: $dW = \gamma \cdot d\sigma$.

In epifluorescence mode, the sample is illuminated with a continuous wave laser beam at a wavelength that lies within the absorption spectrum of the chromophore and the resulted fluorescence is collected through a microscope objective and imaged on a frame grabber (Watec, WAT-902dm_{3s}). Using this technique, it was found that subsequent to infilling the fibres were characterised by the presence of on average 0.1 mm long air-plugs on either side, resulting in a mismatch of termination of the fluidic regions with respect to the fibre facets (fig. 6.2.2 c, d) [2]. As will be discussed below, such a mismatch was critical in terms of the optical excitation of the fibre lasers.

The final preparation step involved the dipping of the fibre lasers into a viscous solution of the polymer CYTOP®*. This step was taken in order to end-cap the fibre ends and to delay the evaporation of the solution and the photo-oxidation of the organic chromophore. A SEM image of a typical end-capped fibre fluidic laser is shown in figure 6.2.3, where the CYTOP coating was partially detached in order to image the sealing layers.

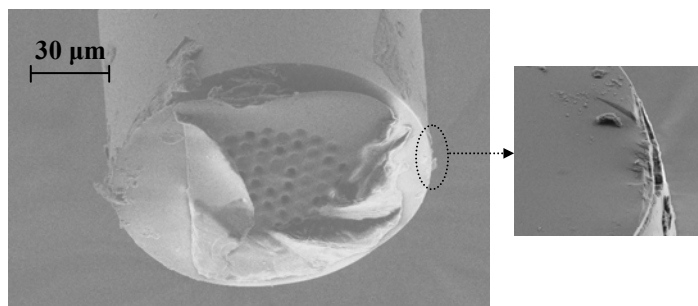


Figure 6.2.3: SEM images of a photonic crystal fibre, end-capped with the index-matched polymer layer.

The infilled photonic crystal fibre features an array of waveguides that can also exhibit gain. Toluene has a higher refractive index than fused silica so that each infilled core can act as a cylindrical liquid waveguide within the silica matrix [3]. For the relevant index difference and the waveguide diameter, seven transverse modes are supported at the wavelength of 620 nm. Optical gain was provided by the excitation of the red chromophore Perylene Red (BASF). This dye was chosen for its high photostability

* Sigma Aldrich 533572, 9 wt. % in perfluorotributylamine.

and its proven improved performance in comparison to the commonly used Rhodamine 6G [4-6]. The typical concentration of the organic dye was 0.5 mg/ml and its absorption and fluorescence spectra at this concentration, along with its molecular structure are shown in figure 6.2.4.

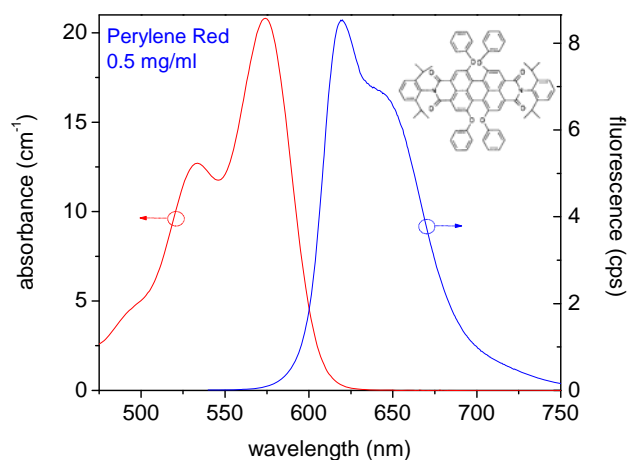


Figure 6.2.4: The absorption (red) and fluorescence (blue) spectra of the organic dye Perylene Red in toluene solution (0.5 mg/ml). *Inset:* the molecular structure of the dye.

The characterisation of the fluidic fibre lasers involved their longitudinal excitation at a wavelength of 532 nm, which lies within the absorption spectrum of the red chromophore. At this wavelength and for the aforementioned concentration, the excitation light is absorbed in the first 800 μm of propagation. In contrast to previous reports where transverse excitation of fluidic fibre lasers was employed, longitudinal excitation was chosen because of the need for homogenous excitation of the multiple fluidic cores [7]. In addition, longitudinal excitation was found to be less sensitive to external perturbations (e.g. optical table vibrations) and also provided long interaction lengths between the pump light and the dye molecules.

The optical pump source was a frequency-doubled diode pumped Nd: YVO₄ laser with repetition rate and pulse duration of 200 Hz and 7.5 nsec respectively. The laser beam was first coupled to an 8 μm core diameter silica fibre through a 25x microscope objective with a numerical aperture of N.A. = 0.5*. The longitudinal excitation of the

* Melles Griot 17 HMO001

laser involved the butt-coupling of the ‘pump’ fibre to the fluidic fibre lasers (figure 6.2.5). Compared with the direct excitation of the fluidic cores through a microscope objective, it was found that the employment of the pump fibre provided more repeatable results and was attributed to the homogeneity of the pump light distribution. The coupling efficiency of the laser beam to the ‘pump’ fibre was approximately 60 %, while the same value from the ‘pump’ fibre to the fluidic cores is not expected to exceed 30 %. In addition, the diameter of the pump fibre was found to be critical both in terms of threshold and quantum efficiency of the fluidic lasers. The 8 μm core diameter fibre provided the optimal coupling; the details of this study will be outlined in the following section.

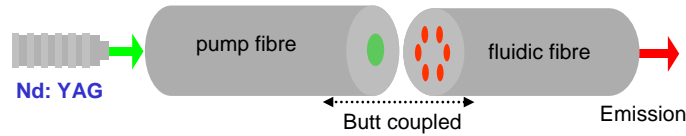


Figure 6.2.5: A schematic of the experimental set-up for the longitudinal excitation of the fluidic fibres.

The emission spectra of the photonic crystal fibre lasers was focused through the 25x objective on to a fibre coupled CCD spectrometer, which in the majority of the experiments had a 40 pm resolution. The output was also focused through the same optics on to a CCD camera* in order to obtain the near-field transverse intensity variation on the fibre facet. This type of imaging does not involve the detection of evanescent waves as in scanning near field optical microscopy, since the modes in this experiment are radiating modes. A typical image is shown in figure 6.2.6, illustrating the transverse distribution of the pump light at the detection end of the fibre. The cores of the photonic crystal fibre are darker, suggesting the pump light has been absorbed at this length (~ 20 mm). In contrast, the fibre cladding is bright, indicating that the launching conditions allow the excitation light to couple to cladding modes as well.

* Coherent LaserCam IIID

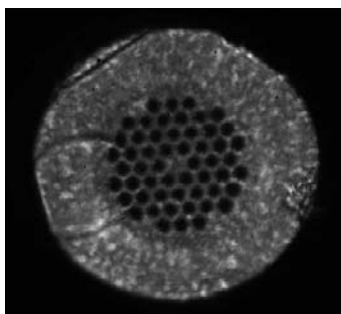


Figure 6.2.6: The distribution of the pump light at the end of the fibre.

6.3 Laser performance

6.3.1 Optical characterisation

When the fibres are longitudinally excited at low energy levels, the radially and axially emitted spectra exhibit certain differences [8]. Typical spectra for a 40 mm long photonic crystal fibre are shown in figure 6.3.1. The radial emission is similar to the fluorescence of the red chromophore, while the axial spectrum is narrower and is particularly reduced at the blue-end of the fluorescence in the wavelength range from 580 nm to 615 nm. In this window, the re-absorption losses are significant due to the overlap of the absorption and fluorescence spectra of the dye molecules in solution. This difference in the axially and radially emitted spectra is indicative of the likely gain spectrum within the optical fibre. Due to the short absorption lengths (800 μm) - in contrast to the total length of the liquid waveguide – the peak gain does not occur in the highest oscillation strength 0-0 transition. This effect was not observed in transversely excited liquid waveguides, where re-absorption losses are comparatively reduced due to the absorption saturation caused by the pump light.

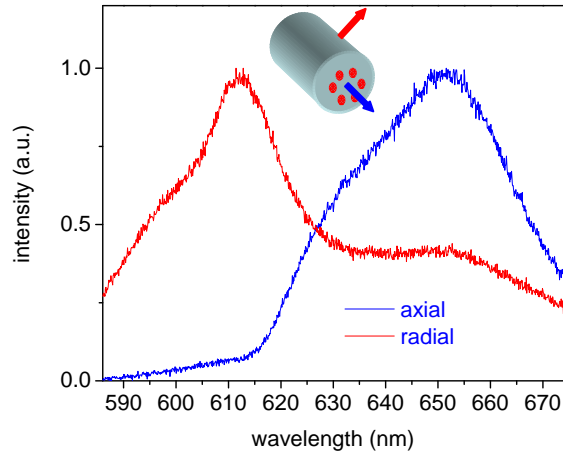


Figure 6.3.1: The radially and axially emitted spectra from the photonic crystal fibre fluidic laser, below threshold (0.79x threshold).

Above threshold, the axial emission is characterised by a series of narrow linewidth peaks with their intensity linearly increasing with the excitation density. In figure 6.3.2, the axially emitted spectra for different excitation densities are plotted for a 40 mm long fluidic fibre laser, pumped through a 50 μm core diameter fibre. For the concentration of 0.5 mg/ml, lasing occurs around the wavelength of 615 nm with the peaks typically spaced in the range of $\Delta\lambda = 1.2$ nm. In contrast, the above threshold radial emission remains unstructured as in figure 6.3.1.

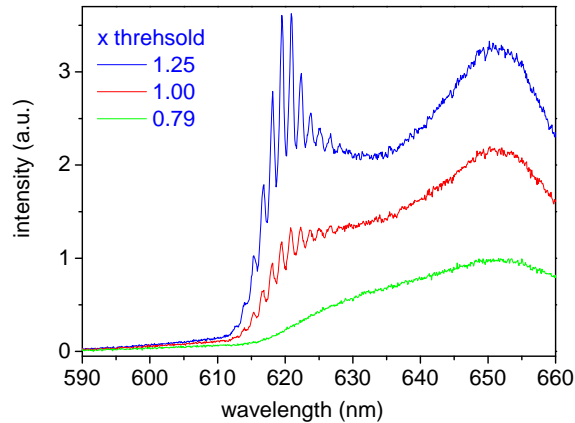


Figure 6.3.2: The axially emitted spectra from the photonic crystal fibre fluidic laser, at different excitation densities.

The near field images of the spontaneous and stimulated emission were captured using the CCD camera as described in section 6.2 and shown in figure 6.3.3. Below

threshold, the intensity distribution of the end-emitted light significantly leaks into the cladding of the photonic crystal fibre, indicative of the isotropy of the spontaneous emission. Above threshold, the emitted light is most intense within the fibre cores due to the directional nature of stimulated emission.

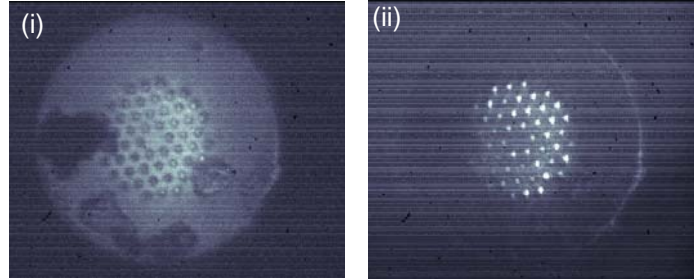


Figure 6.3.3: The near field images of the end-emission from the photonic crystal fibre below (i) and above (ii) threshold.

Similar geometries of lasers have been demonstrated in polymer photonic crystal fibres, where the gain was due to the Raman scattering in the PMMA matrix [9-11]. In order to confirm that in my experiments the laser action was not due to the Raman effect, the fibres were also excited using a tunable laser source. This source was a dye laser tunable over 50 nm, which itself was pumped by a Nitrogen laser. It was found that the emission wavelength from the photonic crystal fibre remains constant when the excitation wavelength was tuned from 510 nm to 535 nm (figure 6.3.4). This is a clear indication that the stimulated emission originates from the transitions between the electronic states of the dye molecules and not between the rotational and vibrational states of the toluene molecules.

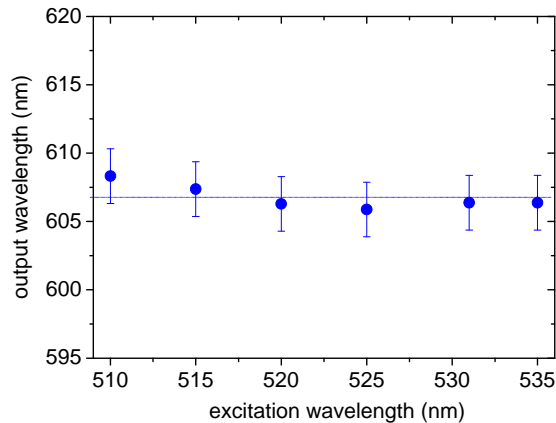


Figure 6.3.4: The emission wavelength from the photonic crystal fibre fluidic laser, as a function of the excitation wavelength.

6.3.2 Coupling efficiency and waveguide length

The coupling efficiency from the pump fibre to the liquid waveguides is critical in the context of the performance of the photonic crystal fibre fluidic lasers. This coupling is naturally hindered by the mismatch between the pump fibre facet and the liquid core termination due to the air-plug formation at either side of the fluidic lasers (section 6.2). The energy transfer to the liquid cores is less efficient for increasing lengths of the air-plugs (x) and was investigated by performing a calculation using the beam propagation method. The calculation was based on commercial software and in order to reduce the computation time it was performed in two dimensions and for a single liquid core. The coupling efficiency - normalized in the case of the absence of the air-plug ($x = 0$) - is plotted in figure 6.3.5(a) as a function of the length of the air-plug (x). In the case of the single fluidic core, the coupling efficiency decreases exponentially with the mismatch length. A calculation to determine the coupling to the multiple cores would necessitate a three dimensional treatment of the problem, but is expected to be of the same nature.

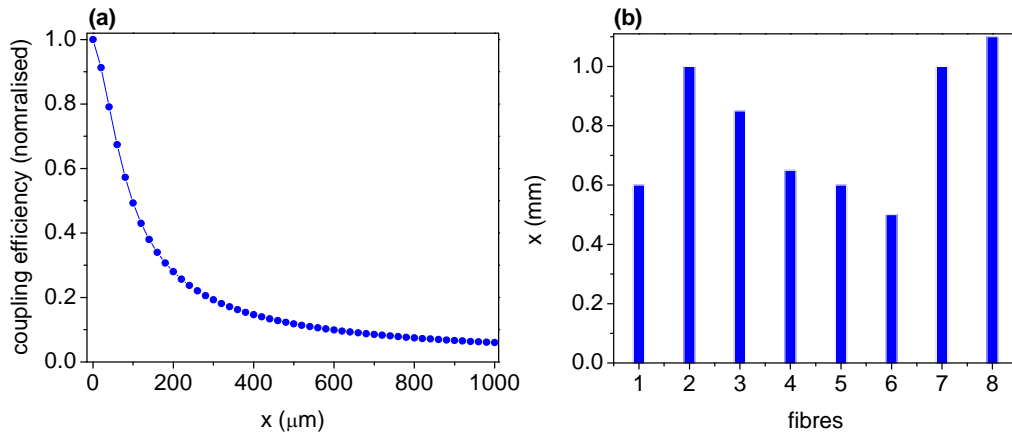


Figure 6.3.5: (a): The power coupling loss from an 8 μm core diameter pump fibre to a liquid waveguide (diameter 3.68 μm) as a function of the length of the air-plug. The normalisation level is the loss value at $x = 0$. (b): A histogram illustrating the variation of the length mismatch (x) for eight different fibres.

A quantitative investigation of the effect of the air-plug termination on the coupling efficiency was not trivial due to the need to measure the exact excitation power within the cores. For this measurement, one would need to discriminate between the

excitation power coupled to core and cladding modes, which was not feasible in most cases. In addition, this length mismatch (x) was found not to be consistent between different experiments and illustrated in figure 6.3.5b for eight consecutive infilled fibres.

To further investigate the effect of the coupling efficiency and optimise the performance of the fluidic lasers, two different types of pump fibres were employed (the number of fibres used was limited by their availability at the time of the experiment). The first pump fibre had a core diameter of 50 μm and the second of 8 μm while the same photonic crystal fibre was used in both cases. The threshold and slope efficiencies of the fluidic fibres were found to be different for the two cases and the measurements for a 40 mm long photonic crystal fibre are shown in figure 6.3.6. The change from the wider to the narrower core diameter resulted in a fivefold increase in the slope efficiency and a decrease in threshold by a factor of approximately 2.

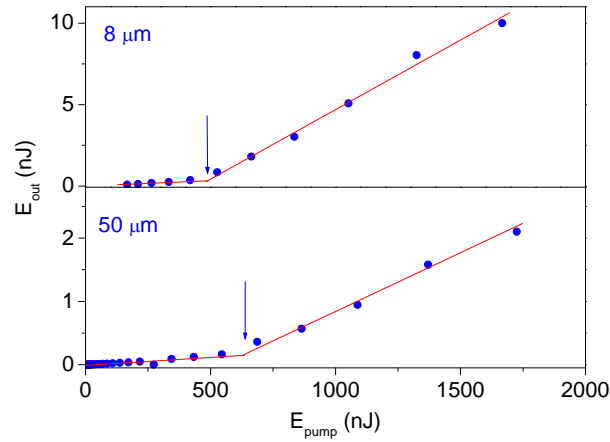


Figure 6.3.6: The input-output characteristics for a 40 mm long photonic crystal fibre laser, when pumped through an 8 μm and a 50 μm core diameter.

The difference in the laser performance depending on the core diameter of the pump fibre is due to the different coupling efficiency in each case. Due to the air-plug termination, prior to coupling to the liquid cores, the excitation light diffuses into the defect core and cladding. The optimised performance when using the 8 μm core

suggests that this type of loss is more profound for the larger core diameter of the pump fibre and that the power exchange between the cladding and liquid core modes is negligible. In addition, the coupling efficiency would be dependent of the mode profile at the end of the pump fibre. In regards to the mode intensity profile, this was determined by the beam propagation method, where a Gaussian source of a 5 μm line-width was used as the excitation and propagated for 50 cm along the two fibres. The calculation was based on commercial software and for calculation speed arguments it was again performed in two dimensions [12]. The results are plotted in figure 6.3.7. In contrast to the 8 μm core diameter, the mode intensity distribution is of larger diameter and multi-mode for the case of the 50 μm diameter core pump fibre. The non-uniform radial intensity variation is expected to be of crucial importance in the context of coupling efficiency.

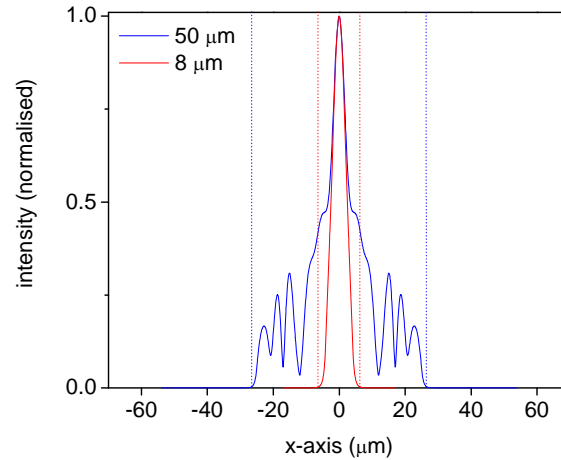


Figure 6.3.7: The mode intensity distribution after propagating 50 cm along an 8 μm (red) and 50 μm (blue) core diameter fibres.

The threshold and slope efficiency were also found to be dependent on the physical length of the liquid waveguides. For this study, an 8 μm core diameter pump fibre was used to excite three lasers based on the photonic crystal fibre with lengths 18 mm, 25 mm and 40 mm and the respective input-output characteristics are plotted in figure 6.3.8. For the increasing length of the fibre lasers, the thresholds were measured to be 333 nJ, 527 nJ and 664 nJ, while the slope efficiencies were 2.2 %, 1.4 % and 0.06 %.

The increase in threshold is indicative of the increased cavity losses within the fibre resonator.

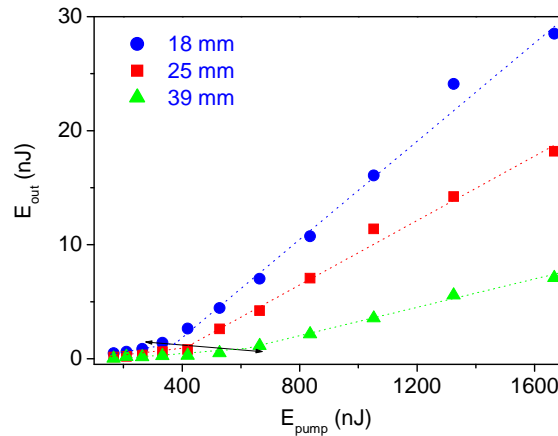


Figure 6.3.8: Comparative study of the input-output relationship for a photonic crystal fibre laser for different lengths. The black arrow designates the threshold energies for the three lasers.

In essence, the excitation light that is longitudinally launched into the cores is absorbed in the initial section of the fibre, which is approximately 800 μm . This is the absorption length and is equivalent to the gain length, since the emitted photons experience gain only in this initial propagation distance. However, the boundary conditions at either end of the liquid waveguide forces the optical field to propagate along the total length of the fibre. Except for the initial amplification length, the rest of the liquid waveguide acts as a source of loss due to the finite Stokes' shift in the electronic structure of the dye Perylene Red (figure 6.2.4). Hence the re-absorption losses are expected to be significant for these long propagation lengths, with the absorbance measured at the lasing wavelength to be 0.015 using a 1cm long cuvette. The length mismatch between the amplification section and the total propagation length is also responsible for the decreasing quantum efficiencies with the fibre length, since the re-absorption losses reduce the output intensity.

6.3.3 Tuneability

The emission wavelength was also found to be tunable by varying the concentration of the dye within the liquid waveguide. By increasing the chromophore density, the wavelength of the laser emission increased and is plotted in figure 6.3.9 for similar fibre lengths (~ 20 mm). The concentration of the solution was varied between 0.06 mg/ml to 4.2 mg/ml, thus achieving a tuning range of approximately 50 nm within the spectral window of the 0-0 and 0-1 vibronics of the fluorescence spectrum of Perylene Red (figure 6.2.4).

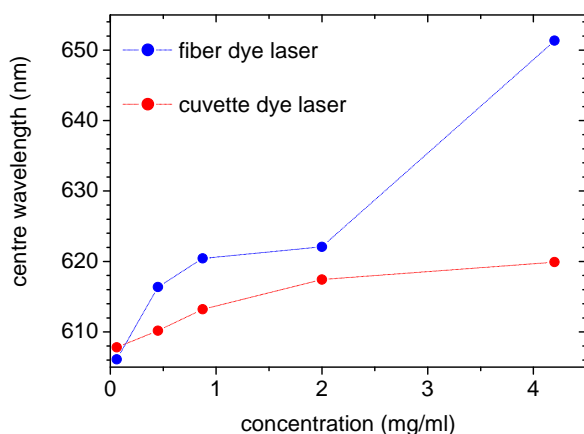


Figure 6.3.9: The tuning of the laser emission with the dye concentration for both a fibre fluidic laser (blue) and a dye laser based on a cuvette (red).

In addition, the tuning rate was also found to be higher than for a dye laser based on a Fabry-Perot resonator formed by the silica walls of a 10 mm long cuvette (6.3.9). The main difference between the two experiments is the excitation configuration, which for the fibre laser was longitudinal as described in section 6.2, while the cuvette based dye laser was transversely pumped with a stripe with dimensions $1 \times 0.3 \text{ mm}^2$. In both cases, the pump wavelength was 532 nm.

The origin of the tuning mechanism also lies within the re-absorption losses. Due to the finite overlap of the fluorescence with the absorption spectra, the chromophores can also act as absorbing species. Consequently, the increased chromophore density results in a higher attenuation of the optical field that propagates along the fluidic

waveguides, as expressed by the Beer-Lambert law (section 2.3.1). This effect was investigated by measuring the end-emitted fluorescence spectra of the Perylene Red solution in cuvette and at the aforementioned concentrations. The respective measurements are plotted in figure 6.3.10a. It can be observed that the short wavelength edge of the fluorescence red shifts with increasing concentration due to the higher absorption at these wavelengths. Such red-shift results in a convenient gain-tuning mechanism since the laser peak red-shifts accordingly for increasing chromophore densities and laser action will occur at the wavelength of the highest net-gain [13]. For the case of the transverse pumping of the dye laser in the cuvette, the tuning rate is not as significant because the gain medium is uniformly pumped along the cavity axis. It is also worth noting that the engineering of the re-absorption losses does not significantly affect the laser performance as indicated by the slope efficiency measurements for the same concentrations (figure 6.3.10b).

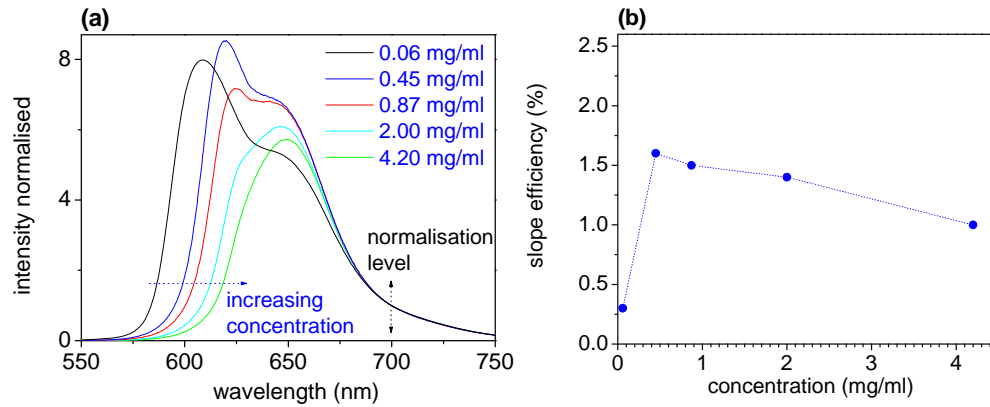


Figure 6.3.10: (a): For increasing chromophore densities, the blue-end of the fluorescence spectra red-shifts. (b): Under the same conditions, the laser efficiency does not vary significantly.

6.4 Wavelength selectivity

Above threshold, the photonic crystal fibre fluidic lasers exhibit a free spectral range that is approximately 300 times longer than expected for a Fabry-Perot resonator formed by the liquid waveguide and the solvent-air interfaces. The laser emission

appears to be strongly modulated by an envelope function, allowing the appearance of only certain longitudinal modes. This intracavity wavelength selectivity mechanism is unanticipated though conveniently provides a functional mode spacing that does not correspond to the fibre length. The study to identify the origin of this mechanism is the theme of this section.

In terms of material effects, longitudinal mode structure has been attributed to the diffusion of the excitation along the cavity axis. In this case, the standing wave creates a periodic axial variation in the gain and depending on the rapidity in which the excitation axially diffuses, other longitudinal modes may experience sufficient gain to exceed threshold [14]. In liquid state dye lasers however, the diffusion constant is relatively low in comparison to crystalline semiconductors and thus this effect is ineligible as the origin of the observed wavelength selectivity mechanism [15].

The presence of an additional resonance constraint that imposes this broader spectral selectivity is more likely. In order to identify its origin, several plausible scenarios were investigated. The first extensive study was on the transverse periodicity of the photonic crystal fibre. In this case, an antiresonant waveguiding mechanism (ARROW) could provide the frequency selection, but was proven not legible either; however it will be outlined for sake of completeness. The investigation of the length dependence on the mode spacing also excluded several resonant mechanisms previously considered responsible for similar observations, but also suggested an uncommon mechanism that has been suggested in the context of coupled resonators: a Vernier type resonant mechanism.

6.4.1 Antiresonant waveguiding

Antiresonant waveguiding was initially proposed in the 80's by researches at Bell Labs as a novel guiding mechanism, with applications such as higher order transverse mode discriminators in large modal area guides and integrated optical polarisers [16].

Antiresonant guiding originates from the resonant properties of the Fabry-Perot formed in the transverse dimension of a waveguide when the finite cladding layers are considered. At all wavelengths, there are modes whose wavevectors are below the cut-off condition and thus can escape through the cladding layers; these modes are referred to as leaky modes. However at specific wavelengths, the reflections from the core-cladding and cladding-coating interface of certain leaky modes interfere destructively and form a low transmission spectral window. Consequently, even below cut-off, it is possible to obtain bound modes localised both in the core and cladding layers under the antiresonant waveguiding condition (ARROW), which for a Fabry-Perot resonator can be described as $e^{2\beta_{Li}} = -1$ (see p. 31 for the definitions of the constants).

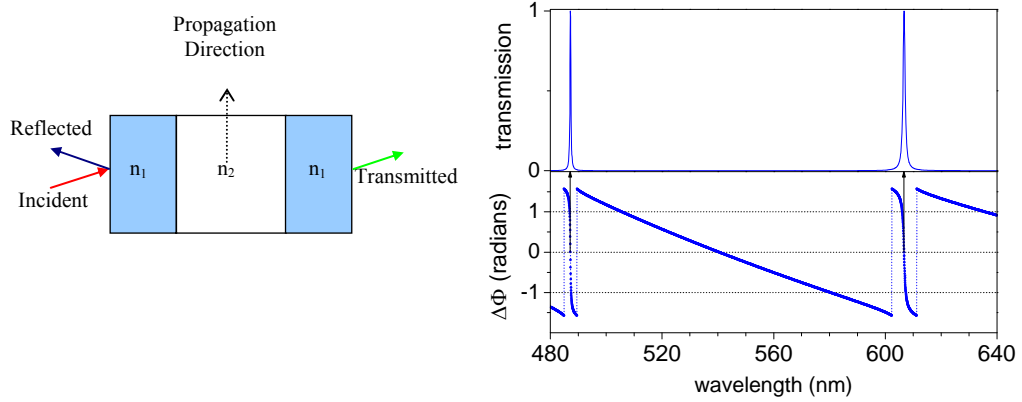


Figure 6.4.1: *Left:* A schematic of the waveguide with the direction of propagation depicted. *Right:* The transmission spectrum in the direction perpendicular to the propagation (*upper*) and the phase change in the same spectral range.

A typical example is shown in figure 6.4.1 for a waveguide formed by toluene (n_2) in silica (n_1) with dimensions of $3.68 \mu\text{m}$ and $4.32 \mu\text{m}$ respectively. The transmission at the cut-off wavevector at each wavelength was calculated with the transfer matrix method for a two dimensional planar case [17]. It can be observed that there are certain wavelength regions of high transmission, where the propagating optical mode leaks out the sides of the waveguide (figure 6.4.1). In addition, the phase change is zero at the peak of the transmission resonance. As one further decreases the value of the longitudinal wavevector below cut-off, the linewidth of these resonant windows increases, until they completely overlap. Such resonant mechanisms have been recently suggested as the origin of the filtering behaviour observed in photonic crystal

fibres, where the cores are infilled with high index inclusions, either liquid or solid [18-24]. In these studies, it has been observed that only at certain wavelengths the loss of a guided mode within the defect core is high. These wavelengths have been identified as the cut-off wavelengths of the guided modes within the high index inclusions.

The lasing experiments I performed were based on a similar photonic crystal fibre as in the aforementioned references and to this end I investigated whether the antiresonant mechanism would be feasible to form a feedback loop. In such case, the multiple liquid cores of the photonic crystal fibre are resonantly coupled forming thus the basis for stimulated emission. In addition, the condition of constructive interference is met due to the phase change being equal to zero at the resonant wavelengths (figure 6.4.1).

However, the antiresonant mechanism was excluded due to several evidences based on both experiments and calculations. The first one was based on the change of the refractive index of the liquid within the cores. This was changed by $\Delta n = 0.04$ by filling the cores with chlorobenzene instead of toluene. Under the ARROW scheme, the transfer matrix calculation indicated that a wavelength shift of 65 nm should occur (figure 6.4.2). However, only a red shift by 4 nm was experimentally observed.

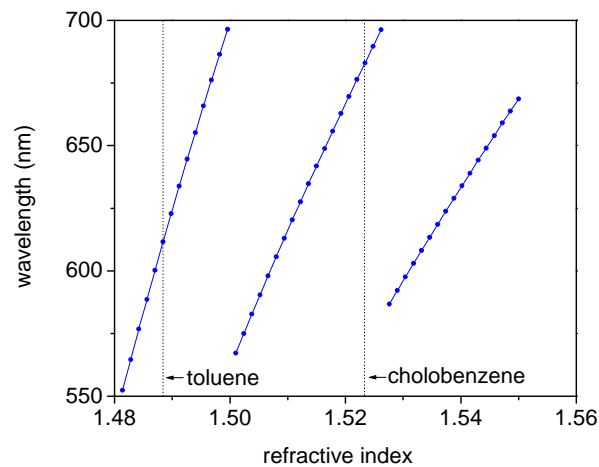


Figure 6.4.2: The dispersion relationship of the resonant wavelengths at the modal cut-off. The refractive indices of toluene and chlorobenzene are indicated with the black dotted lines.

In addition, similar lasing behaviour was observed when using a single core capillary tube. The single core capillary had a core and cladding diameter of 2 μm and 128 μm respectively and as with the photonic crystal it was examined under the SEM (figure 6.4.3(a)). The infilling process, the liquid gain medium and the excitation conditions were the same. Typical experimental spectra below and above threshold for a 25 mm long capillary are shown in figure 6.4.3(b). In terms of threshold and slope efficiency, the single core capillary fluidic lasers performed better than the photonic crystal fibre lasers. However, the free spectral range above threshold exhibits the same characteristics as with the multiple liquid core case, with the mode spacing being again approximately 300 times longer than expected. This evidence indicates that the ARROW mechanism is not eligible as a feedback mechanism, since the wavelength selectivity appears to be the same, irrespective of the number of the liquid cores present in the system.

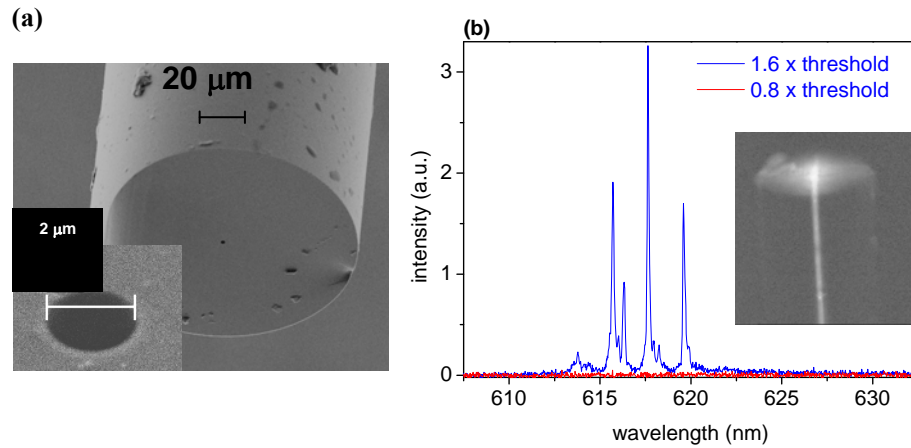


Figure 6.4.3: (a): SEM image of the capillary tube with the inset showing a higher magnification image designating the lateral dimensions of the core. (b): The spectra above and below threshold for the laser based on the capillary tube; the inset shows an epifluorescence image of the infilling process of the capillary tube.

6.4.2 Length dependence and the Vernier effect

In order to further investigate the wavelength selectivity mechanism in the photonic crystal fibre lasers, the dependence of the laser mode spacing was measured as a

function of the physical length of the liquid waveguide. The fluidic fibre lasers were cleaved at different lengths and their effective optical path lengths were determined by Fourier transforming the emission spectra above threshold, a technique that has been used in the context of the spectral analysis of polymer resonators and semiconductor waveguide lasers [25-27]. The Fourier transform of the laser emission spectrum results into a series of peaks situated at values equal to the integer multiples of the product of the laser mode's group index and the cavity length, which in essence is the resonator optical round-trip path. Typical measurements for three different lengths of the photonic crystal fibre are shown in figure 6.4.4, where the emission spectra above threshold are plotted in the left figure and the respective Fourier transform in the right one. The spectral resolution was 0.4 nm^{-1} , resulting thus in a length resolution of approximately 7 nm .

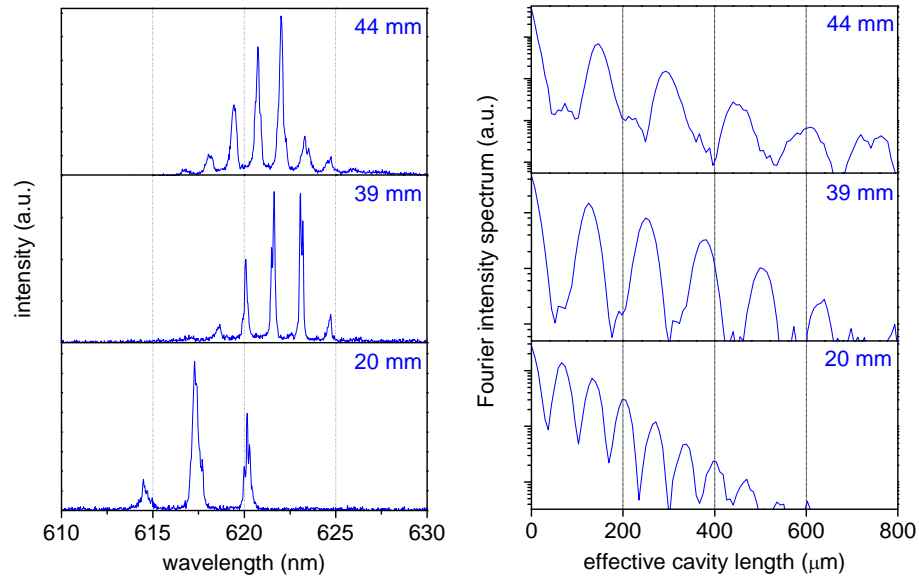


Figure 6.4.4: *Left:* The edge-emitted spectra for different fibre lengths, at an excitation energy of $1.7 \text{ } \mu\text{J}$ *Right:* The Fourier transform spectra for the same fibres.

From the emission spectra, it can be observed that the mode spacing changes inversely with the physical length of the fibre, resembling in this way the length dependence of the spectral behaviour of a Fabry-Perot resonator. In addition, the linewidth of each longitudinal mode decreases with the increasing length of the fibre, indicative of the increased photon lifetime within the longer resonator. The effective cavity length was

determined by fitting a series of Gaussian peaks in the Fourier spectra at each length. The round-trip optical lengths were found to vary with the physical length of the fibres. From the multiple fibre lengths that were examined, this type of variation was observed to be linear and is present in both the photonic crystal fibre and the capillary tube with the 2 μm core diameter and at approximately the same rate (figure 6.4.5).

The linear dependence of the laser mode spacing with the fibre length indicates the primarily longitudinal origin of the wavelength selection mechanism. Under this paradigm, random incoherent scattering from possible fluid non-uniformities and the roughness of the inner walls of the capillary tubes are not eligible as a feedback mechanism. In addition, a wide range of processes that have been reported to affect the mode spacing in waveguide lasers can be excluded as well. These include the resonant condition imposed by the lateral dimensions of the waveguide leading to spatial hole burning effects [28, 29], the purely transverse interference effects with substrate modes leading to a wavelength dependent depletion of the net-gain [30-33], the gain modulation with a spectral spacing equal to the homogenous broadening laser transition [34], the longitudinal resonances imposed by the periodic absorption saturation due to the standing wave formation in fibre lasers [35-37] and the transverse resonant mechanism due to the cylindrical morphology [38-42].

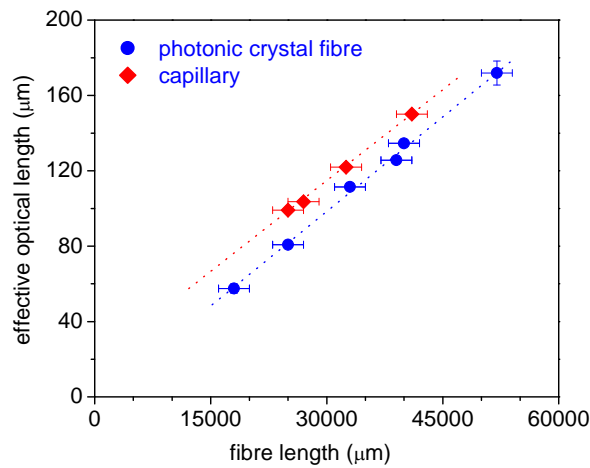


Figure 6.4.5: The linear dependence of the cavity mode spacing with the fibre length both for the photonic crystal fibre (●) and the capillary tube (◆).

On the contrary, such linearity that in essence amplifies the mode spacing has been observed in fiber lasers, laterally coupled and twin-guide semiconductor lasers and attributed to Vernier type resonant effect [43-48]. This mechanism - analogous to the length precision measurements - requires the presence of two (or more) cavities of different spectral range. In such ‘superstructure’, the combination of the comb characteristic transfer functions of each single resonator leads to a combined response of a longer modal spacing. For instance, if the ratio of the free spectral ranges of two cavities is equal to $(N+1)/N$ then the resultant effective FSR will be N times that of the one resonator [43]. The principle of operation is illustrated in figure 6.4.6 (a), where two oscillators with typical reflectivity spectra R_1 and R_2 are combined to obtain a broader reflectivity spectrum where the reflection peaks of the individual resonators coincide.

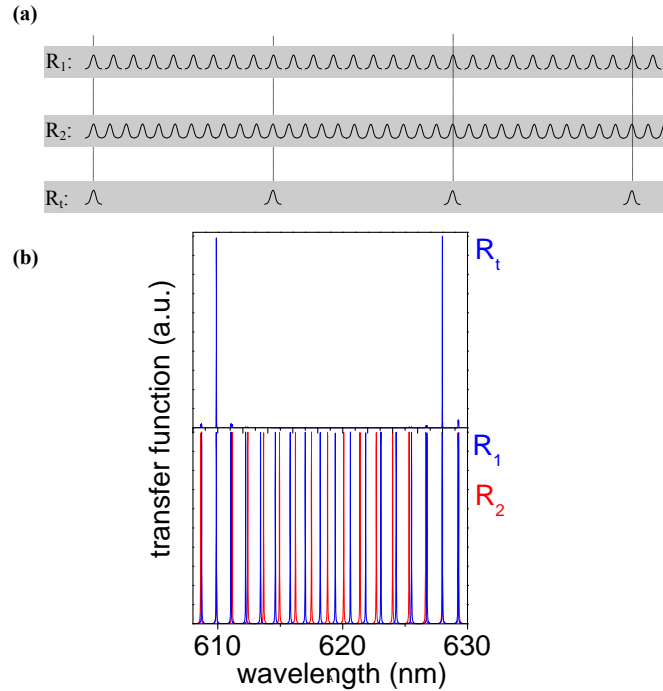


Figure 6.4.6: (a): A schematic illustration of the Vernier effect between two resonators R_1 and R_2 and the resulting transfer function R_t . (b): The Vernier effect for two Fabry-Perot resonators (R_1 and R_2) using the transfer matrix technique.

In figure 6.4.6 (b), the Vernier effect is demonstrated using the transfer matrix method where, two 0.1 mm long Fabry-Perot resonators in series, each supporting a single waveguide mode with indices of 1.482 (R_1) and 1.587 (R_2) are investigated. The

difference in the optical path length of the two resonators and the associated difference in the free spectral range, results in longer mode spacing (R_t), by approximately a factor of 15. However the situation in the photonic crystal fluidic fibre laser is expected to be different. There are no multiple cavities in series and the lateral spacing between the liquid cores is not short enough to allow any energy exchange during the propagation. On the contrary, the required multiple resonances for the Vernier effect are attributed to the different order transverse modes that are supported by the system.

There are two different types of transverse modes, the ones supported by the liquid cores (guided modes) and the ones that are supported by the composite system, including the air-silica interface (leaky modes) as discussed in section 6.4.1. In regards to the guided modes, they were investigated initially in the single capillary tube, as it supports only two transverse modes and consequently is a much simpler system. The group indices of the bound core modes were calculated as discussed in Chapter 5 and were found to be 1.498 ± 0.002 and 1.506 ± 0.001 , giving $\Delta n_g = 0.008 \pm 0.002$. Considering only the core modes, the Vernier effect would increase the mode spacing by a factor $n_g/\Delta n_g = 188 \pm 50$, but experimentally this value is measured at 309 ± 8 . This discrepancy would be accounted for if the effect of leaky modes is included, as recently proposed in a planar structure [49].

Leaky modes are defined as modes that do not exponentially decay outside the core, but are characterised by a propagating wave pattern in the cladding layers as well as in the core, with effective refractive indices lower than the refractive index of the silica cladding. There is experimental evidence that the leaky modes are associated with the wavelength selectivity mechanism that is observed. In this experiment, the coating of both the single capillary and the photonic crystal fibres was not removed, while the infilling process and the excitation geometry and wavelength were not altered. It was found that in the case of the photonic crystal fibre, the acrylate coating did not affect the mode spacing and was confirmed for several fibre lengths that are plotted in figure 6.4.7 (left) for the coated and the uncoated fibre lasers. In contrast, in the single core fluidic laser the polyimide coating was found to hinder the mode selectivity. This is

illustrated in figure 6.4.7 (right), for two fibres of similar lengths (~ 30 mm), one coated (upper) and the other stripped (lower). It can be observed that the coating perturbation inhibits the mode selectivity mechanism and has been confirmed for several lengths of the fibre (16 mm, 26 mm, 42 mm and 55 mm).

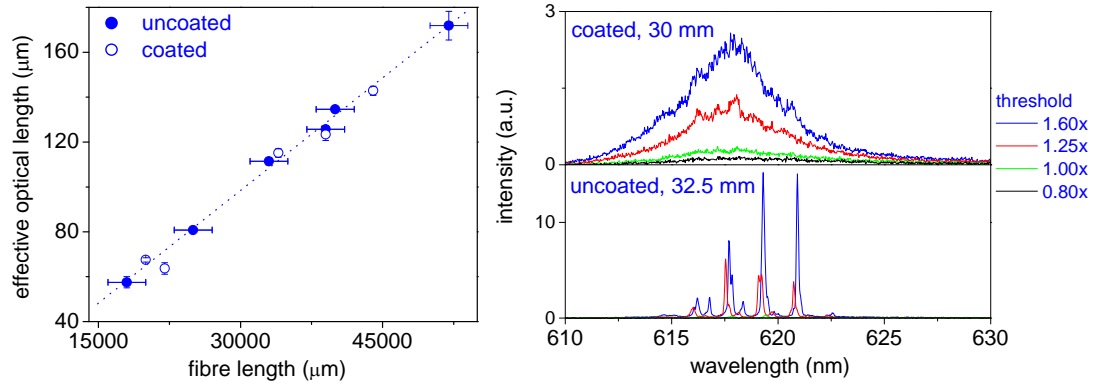


Figure 6.4.7: *Left:* The linear dependence of the cavity mode spacing with the actual fibre length for the photonic crystal fibre uncoated (●) and coated (○). *Right:* The spectral response above and below threshold for the capillary with the coating (upper) and without the coating (lower).

The assumption that the feedback mechanism is similar in the photonic crystal fibre and the single core capillary is based on the same amplification factor of the free spectral range observed in both cases (figure 6.4.5). Consequently, the different behaviour depending on the type of coating present in the two cases, suggests that the optical constants of the coating are significant. In the case of the photonic crystal fibre, the acrylate coating is transparent with a refractive index of 1.5, while in the case of the single capillary the polyamide coating has a much higher refractive index than silica (1.6) and is not transparent in the visible spectral range. Standard waveguide theory cannot be directly applied to solve the wave-equation in the multiple layer system and determine the propagation constants of the leaky modes. Such a task would require demanding computations based on the three-dimensional beam propagation method as suggested by the literature. For this reason, further investigations on the effect of the leaky modes on the free spectral range of the fibre lasers were not possible at the time of the thesis. However, the effect of the coating perturbation indicates that the resonant coupling of core and cladding modes is responsible for this wavelength selectivity mechanism.

6.5 Summary

A fluidic laser based on the photonic crystal fibre ESM-12-01 was the core theme of this chapter. The feasibility of multiple laterally integrated fluidic lasers was demonstrated, hence enhancing the functionality of photonic crystal fibres within the field of opto-fluidics. In addition, single core fibre fluidic lasers were demonstrated based on single core capillary tubes. Both types of laser were prepared based on capillary action, featuring thus a rapid and simple preparation technique, also promising for increased throughput. The disadvantage of this technique is the mismatch in the termination of the fluidic cores and the actual fibre facet and has been observed in similar experiments by other groups.

Laser emission is observed when the fluidic fibres are longitudinally pumped above threshold and manifests itself as an axially emitted beam with a spectrum of a series of narrow peaks. Longitudinal excitation was employed in order to provide adequate absorption length for the pump light, while keeping the chromophore density and thus the concentration quenching at low levels. The threshold and quantum efficiency were found to be dependent on the coupling efficiency of the pump light and the fibre length. In regards to the coupling efficiency, this was not trivial to investigate both experimentally and numerically. An indirect study took place instead, where it was found that the diameter of the core of the pump fibre is important and a value of 8 μm was found optimal. The operation characteristics of the fluidic lasers were found to degrade with the length of the fibre and this is attributed to the significant re-absorption losses of the laser field along the liquid waveguides.

The practicality of these optical sources is greatly enhanced by the possibility of tuning their emission by varying the chromophore density within the liquid core. Both in the single and multiple core lasers, the cavity mode spectrum was found to have a shorter free spectral range than expected for a Fabry-Perot cavity formed by the ends of the liquid waveguides. This advantageous spectral selectivity is attributed to a Vernier resonant mechanism between transverse electromagnetic modes of the fluidic laser.

The photonic crystal fibre features a hexagonal array of approximately 50 fluidic lasers demonstrating the prospect of lateral integration and can be used for the formation of an optical lattice with applications in optical tweezing. This type of laser is promising for opto-fluidic sensing and spectroscopy applications, and provides a convenient platform for rapid investigation of new types of liquids and organic dye molecules.

6.6 References

1. P.W. Atkins, 'Physical Chemistry', 3rd Edition, 154 (1986).
2. P. Steinvurzel, B.T. Kuhlmei, T.P. White, M.J. Steel, C. Martijn De Sterke, B. J. Eggleton, 'Long wavelength anti-resonant guidance in high index inclusion microstructured fibers', *Optics Express* **12**, 5424 (2004).
3. A. Samoca, 'Dispersion of refractive properties of solvents: Chloroform, toluene, benzene, and carbon disulfide in ultraviolet, visible, and near-infrared', *Journal of Applied Physics* **94**, 6167 (2003).
4. G. Quian, Y. Yang, Z. Wang, C. Yang, Z. Yang, M. Wang, 'Photostability of perylene orange, perylene red and pyrromethene 567 laser dyes in various precursors derived gel glasses', *Chemical Physics Letters* **368**, 555 (2003).
5. M. Canva, P. Georges, J.F. Perelgritz, A. Brum, F. Chaput, J.P. Boilot, 'Perylene- and pyrromethene-doped xerogel for a pulsed laser', *Applied Optics* **34**, 428 (1995).
6. M. Faloss, M. Canva, P. Georges, A. Brun, F. Chaput, J.P. Boilot, 'Toward millions of laser pulses with pyrromethene- and perylene-doped xerogels', *Applied Optics* **36**, 6760 (1997).
7. T. Kobayashi, W.J. Blau, 'Laser emission from conjugated polymer in fibre waveguide structure', *Electronic Letters* **38**, 67 (2002).
8. M. Saito, K. Kitagawa, 'Axial and radial fluorescence of dye-doped polymer fibre', *Journal of Lightwave technology* **19**, 982 (2001).
9. U. Gibson, U. Österberg, 'Comment on "Microstructured polymer fiber laser"', *Optics Letters* **30**, 1827 (2005).
10. A. Argyros, M.A.V. Eijkelenborg, S.D. Jackson, R.P. Mildren, 'Reply to comment on "Microstructured polymer fiber laser"', *Optics Letters* **30**, 1829 (2005).
11. A. Argyros, M.A.V. Eijkelenborg, S.D. Jackson, R.P. Mildren, 'Microstructured polymer fiber laser', *Optics Letters* **29**, 1882 (2004).

12. Beam Propagation Method, RSoft Design Group, Inc. BeamPROP 5.1.
13. S.K. B. Helbo, B.G. Kjeldsen, J.L. Reimers, A. Kristensen, 'Investigation of the dye concentration influence on the lasing wavelength and threshold for a micro-fluidic dye laser', *Sensors and Actuators A* **111**, 21–25 (2004).
14. W. Streifer, R.D. Burham, D.R. Scifres, 'Dependence of longitudinal mode structure on injected carrier diffusion in diode lasers', *IEEE Journal of Quantum Electronics* correspondence, 404 (1977).
15. H.G. Danielmeyer, 'Effects of drift and diffusion of excited states on spatial hole burning and laser oscillation', *Journal of Applied Physics* **42**, 3125 (1971).
16. M.A. Duguay, K. Kokuburn, T.L. Koch, L. Pfeiffer, 'Antiresonant reflecting optical waveguides in SiO₂-Si multilayer structures', *Applied Physics Letters* **49**, 13 (1986).
17. A. Yariv, P. Yeh, 'Optical waves in crystals', Wiley Classics Library (2003).
18. A.K. Abeeluck, N.M. Litchinitser, C. Headley, B.J. Eggleton, 'Analysis of spectral characteristics of photonic bandgap waveguides', *Optics Express* **10**, 1320 (2002).
19. F. Luan, A.K. George, T.D. Hedley, G.J. Pearce, D.M. Bird, J.C. Knight, P.S.J. Russell, 'All solid bandgap fiber', *Optics letters* **29**, 2369 (2004).
20. N.M. Litchinitser, A.K. Abeeluck, C. Headley, B.J. Eggleton, 'Antiresonant reflecting photonic crystal optical waveguides', *Optics letters* **27**, 1592 (2002).
21. G. Renversez, P. Boyer, A. Sagrini, 'Antiresonant reflecting optical waveguide microstructured fibres revisited: a new analysis based on leaky mode coupling', *Optics Express* **14**, 5682 (2006).
22. A. Argyros, T.A. Birks, S.G. Leon-Saval, C.M.B. Cordeiro, P.S.J. Russell, 'Guidance properties of low-contrast photonic bandgap fibres', *Optics Express* **13**, 2503 (2005).
23. N.M. Litchinitser, S.C. Dunn, P.E. Steinvurzel, B.J. Eggleton, T.P. White, R.C. Mcphedran, C.M.D. Sterke, 'Application of an ARROW model for designing tunable photonic devices', *Optics Express* **12**, 1540 (2004).
24. T.T. Larsen, A. Bjarklev, D.S. Hermann, J. Broeng, 'Optical devices based on liquid crystal photonic bandgap fibres', *Optics Express* **11**, 2589 (2003).
25. D. Hofstetter, R.L. Thorton, 'Loss measurements on semiconductor lasers by Fourier analysis of the emission spectra', *Applied Physics Letters* **72**, 404 (1997).
26. R.C. Polson, G. Levina, Z.V. Vardeny, 'Spectral analysis of polymer microring lasers', *Applied Physics Letters* **76**, 3858 (2000).
27. R.C. Polson, M.E. Raikh, Z.V. Vardeny, 'Universality in unintentional laser resonators in p-conjugated polymer films', *C.R. Physique* **3**, 509 (2002).
28. R.H. D. Ouyang, N.N. Ledenstov, S. Bogner, R.L. Sellin, Ch. Ribbat, D. Bimberg, 'Lateral-cavity spectral hole burning in quantum dot lasers', *Applied Physics Letters* **81**, 1546 (2002).
29. S. Yokoyama, T. Nakahama, S. Mashiko, 'Amplified spontaneous emission and laser emission from a high optical-gain medium of dye-doped dendrimer', *Journal of Luminescence* **111**, 285 (2005).

30. E.P. O'Reilly, A.I. Onischenko, E.A. Avrutin, D. Bhattacharyya, J.H. Marsh, 'Longitudinal mode grouping in InGaAs/GaAs/AlGaAs quantum dot lasers: origin and means of control', *Electronic Letters* **34**, 2035 (1998).
31. I.A. Avrutsky, R. Gordon, R. Clayton, J.M. Xu, 'Investigations of the spectral characteristics of 980-nm InGaAs-GaAs-AlGaAs lasers', *IEEE Journal of Quantum Electronics* **33**, 1801 (1997).
32. A. Patane, A. Polimeni, L. Eaves, M. Henini, P.C. Main, P.M. Snowton, E.J. Johnston, P.J. Hulyer, E. Herrmann, G.M. Lewis, G. Hills, 'Experimental studies of the multimode spectral emission in quantum dot lasers', *Journal of Applied Physics* **87**, 1943 (2000).
33. C. Ribbat, S. Bogner, R. Sellin, D. Bimberg, 'Spectral mode dynamics of short cavity quantum-dot lasers', *Applied Physics Letters* **81**, 147 (2002).
34. M. Sugawara, K. Mukai, Y. Nakata, H. Ishikawa, 'Effect of homogeneous broadening of optical gain on lasing spectra in self-assembled $\text{In}_x\text{Ga}_{1-x}\text{As}$ /GaAs quantum dot lasers', *Physical Review B* **61**, 7595 (2000).
35. M. Horowitz, R. Daisy, B. Fischer, J.L. Zyskind, 'Linewidth-narrowing mechanism in lasers by nonlinear wave mixing', *Optics Letters* **19**, 1406 (1994).
36. M. Horowitz, R. Daisy, B. Fischer, J.L. Zyskind, 'Narrow linewidth, singlemode erbium-doped fibre laser with intracavity wave mixing in saturable absorber', *Electronic Letters* **30**, 648 (1994).
37. B. Fischer, J.L. Zyskind, J.W. Sullof, D.J. Digiovanni, 'Nonlinear wave mixing and induced gratings in erbium-doped fiber amplifiers', *Optics Letters* **18**, 2108 (1993).
38. A.C. Lind, J.M. Greenberg, 'Electromagnetic scattering by obliquely oriented cylinders', *Journal of Applied Physics* **37**, 3195 (1966).
39. H.-M. Tzeng, K.F. Wall, M.B. Long, R.K. Chang, 'Laser emission from individual droplets at wavelengths corresponding to morphology-dependent resonances', *Optics Letters* **9**, 499 (1984).
40. H.-B. Lin, J.D. Eversole, A.J. Campillo, 'Spectral properties of lasing microdroplets', *Journal of the Optical Society of America B* **9**, 43 (1992).
41. H.C. Van de Hulst, 'Light scattering by small particles', Wiley, New York, 297 (1957).
42. J.C. Knight, H.S.T. Driver, R.J. Hutcheon, G.N. Robertson, 'Core-resonance capillary-fiber whispering-gallery-mode laser', *Optics Letters* **17**, 1280 (1992).
43. Y.H. Ja, 'Optical Vernier filter with fibre grating Fabry-Perot resonators', *Applied Optics* **34**, 6164 (1995).
44. R. Todt, T. Jacke, R. Laroy, G. Morthier, M.-C. Amann, 'Demonstration of Vernier effect tuning in tunable twin-guide laser diodes', *IEE Proceedings Optoelectronics* **152**, 66 (2005).
45. R.J. Lang, A. Yariv, J. Salzmans, 'Laterally coupled-cavity semiconductor lasers', *IEEE Journal of Quantum Electronics* **23**, 395 (1987).
46. S. Srivastava, R. Gopal, S. Sai, K. Srinivasan, 'Feedback Mach-Zehnder resonator with 'reflector': Analysis and applications in single frequency fiber lasers', *Applied Physics Letters* **89**, 141118 (2006).

47. A. Mihaescu, T.T. Tam, P. Besnard, G.M. Stephan, 'Effects of external cavities on laser spectra: application to a fibre laser', *Journal of Optics B: Quantum and Semiclassical Optics* **4**, 67 (2002).
48. A.J. Poustie, N. Finlayson, P. Harper, 'Multiwavelength fiber laser using spatial mode beating filter', *Optics Letters* **19**, 716 (1994).
49. L.M. Blinov, G. Cipparrone, P. Pagliusi, V.V. Lazarev, S.P. Palto, 'Mirrorless lasing from nematic liquid crystals in the plane waveguide geometry without refractive index or gain modulation', *Applied Physics Letters* **89**, 031114 (2006).

CHAPTER 7:

Conclusions

Microstructured dielectric environments can significantly modify the optical emission process in terms of number of photons emitted per unit area, time and wavelength. Organic semiconductors are ideal candidates for both exploring the photonic properties of resonant microstructures and employing the findings in order to develop laser sources. This type of structures is a promising candidate in the field of visible lasers and their prospects are significantly enhanced by the possibility of mass production using cost-effective fabrication techniques, such as soft lithography. Several different feedback mechanisms were explored in this thesis in order to control the stimulated emission from these chromophores. These mechanisms were investigated both in the context of solid-state polymer and fluidic dye lasers.

Periodically microstructured polymer lasers exhibit similar optical properties to photonic crystals but under the weak index modulation regime. The periodicity of the refractive index leads to strong effects in the weak regime, one of which is the formation of Bloch waves due to interference effects within the polymer film. This type of laser was examined in Chapter 4, using both experimental measurements and photonic crystal calculation methods, with the ultimate aim to improve their performance and reduce their oscillation thresholds. It was found that the coupling to free space radiation is a major source of loss in surface-emitting polymer lasers. By employing an alternative resonant symmetry and first order gratings ($a/\lambda = 0.5$), the coupling to free space was cancelled and the emission was re-directed to the edge of the film. This resulted in a threshold reduction by almost an order of magnitude. The

edge-emitted laser beam however suffered from significant divergence. The poor beam quality was addressed by integrating an output coupler in the vicinity of the resonator and hence a low threshold surface-emitting polymer laser was obtained.

The effect of the symmetry breakage of a periodic feedback lattice by the introduction of a structural defect was investigated in Chapter 5. These are the DBR resonators and were configured as compact, surface-emitting polymer lasers. In comparison to DFB lasers, the presence of the defect resulted in a higher net-gain and lower oscillation thresholds. The laser performance was studied below threshold, where the defect modes were identified. Above threshold a frequency selection mechanism was observed and attributed to the variation of scattering losses across the stop-band of the Bragg mirrors. In terms of applications, GaN diode pumped polymer lasers were demonstrated. This is a considerable advance denoting the transition from complex pump lasers to more compact and practical excitation sources. Also in Chapter 5, a novel DBR resonator design was examined and a polymer laser based on silicon was demonstrated. This demonstration offers a potential route to cost-effective optical interconnects since it combines CMOS fabrication technologies and solution processible light emitters. The hybrid structure was configured as surface emitting in the visible spectral range. The emission wavelength lies within the energy gap of Si and consequently it is compatible with the prospect of lateral integration with Si photodetectors.

In chapter 6, the properties photonic crystal fibres infilled with dye molecules in solution were analysed in the context of fluidic dye lasers. The photonic crystal fibre is an alternative type of a periodically microstructured silica matrix, where the periodicity is transverse to the propagation direction. Laser action was obtained from these microstructures, enhancing thus their functionality in the field of optofluidics. The emission spectrum of the laser consisted of a series of narrow linewidth peaks, with a free spectral range that did not correspond to the length of the fibres. The length dependence of the larger than expected free spectral range, indicated that a Vernier resonant mechanism between transverse electromagnetic modes of the fibre is

responsible for this effect. The effect of the cladding was also examined and the results suggested that the cladding modes are likely to be involved. A method to tune the laser emission wavelength was determined based on a gain tuning mechanism due to the variation of the chromophore density within the liquid cores. The photonic crystal fibre features a hexagonal array of approximately 50 fluidic lasers and can be used for the formation of an optical lattice with applications in optical tweezing. This type of laser is promising for opto-fluidic sensing and spectroscopy applications, and provides a convenient platform for rapid investigation of new types of liquids and organic dye molecules.

In regards to future work, preliminary results suggest that the surface-emitted quantum efficiency is significantly higher in DBR than DFB lasers (figure 7.1). Further experiments would support this argument and quantify this effect, while coupled-wave mode theory calculation would be the simplest method to confirm this observation.

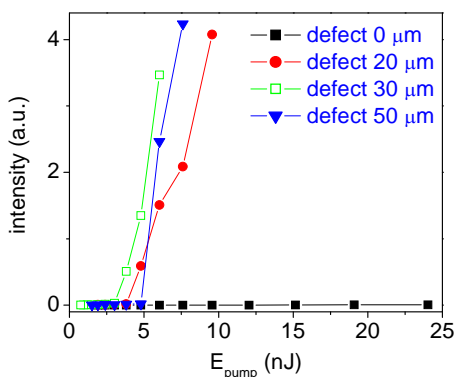


Figure 7.1: The input-output relationships for a DFB (black) and three DBR lasers (color). For this experiment, the microchip laser was employed and the collection set-up was the same for all lasers. Apart from the reduced oscillation threshold, DBR lasers exhibit enhanced quantum efficiency.

The outcomes of Chapters 4 and 5 could be combined to further improve the performance of solid-state polymer lasers. The structural defect can be placed in-between non-radiating Bragg reflectors, where the feedback is provided with a first order diffraction process and a separate grating in the vicinity of the mirrors can provide the advantageous surface emission. The combination of the low radiation and scattering losses can potentially further decrease the threshold of polymer lasers.

The Si based resonators offer a unique opportunity for electrical injection. P doped silicon can be employed as a hole injection layer [1] and could consequently act both as a contact and mirror with the prospect of realizing an electrically excited resonant cavity organic LEDs and ultimately electrical injection lasing.

In the context of the fluidic fibre lasers, the employment of advanced numerical methods would allow the determination of the propagation constants of the bound waveguide modes in the liquid-silica composite system. With these values, the identification of the modes that contribute to the Vernier effect would be possible, since the periodicity in the emission spectrum is related to the difference of the propagation constants between the core and cladding modes.

Alternative types of fibres could be explored, aiming to coherently couple the parallel cores, given that these are more closely spaced. To this end, the infilling and optical properties of the NL-1550-NEG-1 fibre (lattice constant: 1 μm , Crystal Fibre) have been explored, indicating that the same infilling process can be applied and stimulated emission is possible. Alternative types of liquids could be employed and ionic liquids are suitable candidates due to their electrical conductivity and low vapour pressure [2]. During this work, the ionic liquids based $[\text{N}_{2226}][\text{Tf}_2\text{N}]$ and $[\text{omp}][\text{Tf}_2\text{N}]$ were employed*. However, it was found that the infilling process via capillary action was not successful and surface treatment (silinization) is required.

Finally, the long interaction lengths in the fluidic photonic crystal fibre configuration can be employed for the enhancement of non-linear processes within the liquid cores and ultimately could be used to demonstrate an organic laser pumped by two-photon absorption [3, 4].

* The ionic liquids used were supplied by M.J. Muldoon and the assistance of P. André is gratefully acknowledged.

References

1. G.G. Qin, A.G. Xu, G.L. Ma, G.Z. Ran, Y.P. Qiao, B.R. Zhang, W.X. Chen, S.K. Wu, 'A top emission organic light emitting diode with a silicon anode and an Sm/Au cathode', *Applied Physics Letters* **85**, 5406 (2004).
2. P. Bonhote, A. Dias, N. Papageorgiou, K. Kalyanasundaram, M. Grätzel, 'Hydrophobic, Highly Conductive Ambient-Temperature Molten Salts', *Inorganic Chemistry* **35**, 1168 (1996).
3. G.S. He, R. Signorini, P.N. Prasad, 'Longitudinally two photon pumped leaky waveguide dye film laser', *IEEE Journal of Quantum Electronics* **34**, 7 (1998).
4. G.S. He, R. Hegleson, T.-C. Lin, Z. Qingdong, F. Wudl, P.N. Prasad, 'One- two- and three photon pumped lasing in a novel liquid dye salt system', *IEEE Journal of Quantum Electronics* **39**, 1003 (2003).

Appendix A:

Procedure for electron beam fabrication

Sample Preparation:

- The sample is thoroughly cleaned in Acetone and IPA ultrasonic bath. If there are visible 'comets' after the resist is spun, the cleaning procedure must be repeated.
- The resist solution PMMA: Anisole at a ratio of 1:1, which for a spin speed of 4000 rpm results in a film thickness of approximately 140 nm. The resist is subsequently baked at 178°C for four minutes, followed by the spin coating of a thin PEDOT layer at 5000 rpm. A thin layer of Au approximately 15 nm thick is finally sputtered.

Sample Development:

- The exposed sample is placed in a solution of IPA: H₂O at a ratio 24 ml: 10 ml for approximately one minute and then in IPA for 20''.
- If the Au film is not completely removed, the process is repeated for half the aforementioned durations.

Sample Etching:

The conditions for an etch rate of 20nm/min are:

- Ring position 31 cm.
- Set Point: 43 W.
- Strike/Etch Pressure: $2 \cdot 10^{-1}$ mbar/ $5.2 \cdot 10^{-2}$ mbar.
- CHF₃ gas flow set at 200.

Appendix B:

Publications arising from this work

Journals

- M. Alvaréz, A.E. Vasdekis, G.A. Turnbull, ‘Comparison of the operating characteristics of conjugated polymer and solid-state dye distributed feedback lasers,’ *in preparation* (2007).
- A.E. Vasdekis, S. Moore, A. Ruseckas, T.F. Krauss, G.A. Turnbull, I.D.W. Samuel, ‘Silicon based organic semiconductor laser,’ *Applied Physics Letters* **91**, 051124 (2007).
- D. Amarasinghe, A. Ruseckas, A.E. Vasdekis, M. Goossens, G.A. Turnbull, I.D.W. Samuel, 'Amplification of optical pulse sequences at a high repetition rate in a polymer waveguide,' *Applied Physics Letters* **91**, 011105 (2007).
- A.E. Vasdekis, G.E. Town, G.A. Turnbull, I.D.W. Samuel, ‘Fluidic fibre dye lasers,’ *Optics Express* **15**, 3962 (2007) / *also featured in Laser Focus World* **43** (7), 44 and the *Virtual Journal for Biomedical Optics*.
- A.E. Vasdekis, G. Tsiminis, J.-C. Ribierre, L.O. Faolain, T.F. Krauss, G.A. Turnbull, I.D.W. Samuel, 'Diode pumped distributed Bragg reflector lasers based on a dye-to-polymer energy transfer blend,' *Optics Express* **14**, 9211 (2006).
- D. Amarasinghe, A. Ruseckas, A.E. Vasdekis, M. Goossens, G.A. Turnbull, I.D.W. Samuel, 'Broadband solid state optical amplifier based on a semiconducting polymer,' *Applied Physics Letters* **89**, 201119 (2006).
- A.E. Vasdekis, G.A. Turnbull, I.D.W. Samuel, P. Andrew and W.L. Barnes ‘Low threshold edge emitting polymer distributed feedback laser based on a square lattice,’ *Applied Physics Letters* **86**, 161102 (2005).

- A.E. Vasdekis, G.A. Turnbull, I.D.W. Samuel, G.E. Town, 'Novel diffractive feedback structures for semiconducting polymer lasers,' Proc. SPIE Int. Soc. Opt. Eng., **5937**, 311-318 (2005).
- F.M. Bain, A.E. Vasdekis, G.A. Turnbull, 'Holographic recording of sub-micron period photonic crystals in the photoresist SU8,' Proc. SPIE Int. Soc. Opt. Eng., **5931**, 334 (2005).

Conferences

- A. E. Vasdekis, G. Tsiminis, D. Amarasinghe, A. Ruseckas, M. Goossens, L. O'Faolain, T. F. Krauss, G. A. Turnbull, I. D. W. Samuel (*INVITED*), CTuL3, *CLEO®/QELS, Baltimore, USA (2007)*.
- G. A. Turnbull, A. E. Vasdekis, G. Tsiminis, I. D. W. Samuel, 'Diode pumped polymer lasers' 6655-30, SPIE Symposium on Optics & Photonics, San Diego, USA (2007).
- G.A. Turnbull, A.E. Vasdekis, G.E. Town and I.D.W. Samuel, 'Microfluidic dye lasers based on microstructured optical fibres,' CJ-15-TUE, *CLEO®/Europe, Munich (2007)*.
- G. A. Turnbull, A.E. Vasdekis, S. Richardson, G. Tsiminis, L. O'Faolain, T.F. Krauss, G.A. Turnbull, I.D.W. Samuel, 'Microstructured polymer lasers: diode-pumped lasing and extending operation lifetimes,' CE2-2-TUE, *CLEO®/Europe, Munich (2007)*.
- A.E. Vasdekis, G. Tsiminis, S. Richardson, J.-C. Ribierre, G.A. Turnbull, I.D.W. Samuel, 'Microstructured Organic Semiconductor Lasers,' IEEE LEOS Scottish Chapter meeting on Photonic Crystals, St. Andrews, U.K. (2006).
- A.E. Vasdekis, G.E. Town, G.A. Turnbull and I.D.W. Samuel, 'Light Pipes in Contact Giving a Novel Organic Optical Source,' Quantum Electronics and Photonics 17, Manchester, U.K. (2006).
- A.E. Vasdekis, G.A. Turnbull, T.F. Krauss, I.D.W. Samuel, 'Optimising the Performance of Nanostructured Polymer Lasers,' ICSM, Dublin (2006).

- D. Amarasinghe, M. Goosens, A. Ruseckas, A.E. Vasdekis, I.D.W. Samuel, 'High Gain Optical Amplification in MEH-PPV Films,' ICSM, Dublin (2006).
- G.E. Town, A.E. Vasdekis, F. Bain, G.A. Turnbull, I.D.W. Samuel, 'Dual wavelength semiconducting polymer DFB laser,' paper CA8-5-TUE, CLEO[®]/Europe, Munich (2005).
- G.E. Town, A.E. Vasdekis, G.A. Turnbull, I.D.W. Samuel, 'Temperature tuning of a semiconducting polymer DFB laser,' IEEE/LEOS, Sydney (2005).
- A.E. Vasdekis, G.A. Turnbull, I.D.W. Samuel, P. Andrew and W.L. Barnes 'Blue and red polymer distributed feedback lasers using two different symmetries of a square lattice,' Photon '04, Glasgow (2004).